Master thesis - Electrical Engineering

Analysis and Design of Dual Band THz Imager Based on Incoherent Detectors

Shahab Oddin Dabironezare 4292480

Delft University of Technology

November 16, 2015

Master-track Telecommunications,
Faculty of Electrical Engineering,
Mathematics and Computer Science

Analysis and Design of Dual Band THz Imager Based on Incoherent Detectors (November 16, 2015)

TU Delft Delft University of Technology

TS THz Sensing Group

Preface

This work focuses on designing and evaluating the performance of a dual-band passive imager for security applications at sub-mm wave regime. The bolometer based kinetic inductive detectors are used as incoherent detectors on the focal plane array of this imaging system. In order to realize a dual-band system, two absorber sets are designed to operate at separate frequency bands and reject power at the other band. The frequency selectivity of the design is introduced by using the absorber based frequency selective surfaces as a layer on top of the bolometer based detectors. Using the provided spectral analysis tools, the total performance of the detector coupled optics is evaluated. This evaluation is performed in terms of the optical efficiency, the angular response of the imager to a point source, the angular resolution and the noise equivalent temperature difference of the imager. The mentioned parameters are obtained for a generic parabolic reflector based imager coupled to a detector located at the center of the FPA. Moreover, using GRASP computational software and the provided analysis method, the performance of the specific optics used in the CONSORTIS imaging system for the detector at the center of the FPA and also at the edge are approximated.

This thesis is submitted in partial fulfillment of the requirements for the degree of Master of Science in Electrical Engineering at Delft University of Technology.

Shahab Oddin Dabironezare
Delft, November 2015

Acknowledgments

I would like to thank Prof. Andrea Neto who provided me the opportunity to be in this field. I used the verb *be*, since I came to TU Delft 2.5 years ago to follow a very different study path. However, by attending Prof.Neto's first lecture in the Master kick-off event, I realized that I might have to reconsider my decisions, which eventually I did.

I would to thank dr. Nuria Llombart who has been the best supervisor one can hope for, both in the amount of time one can patiently spent on her students, and in the amount of knowledge one can possess in this field to guide students. I am looking forward to working with you in the coming years.

Moreover, I would like to thank dr. Erio Gandini who also supervised me throughout my work and explained various subjects to me. Who also spent patiently an immense amount of time to revise this thesis.

I would also like to thank all of the people in the Tera-Hertz Sensing Group. You all made this place a happier place to work in. From the casual talks and coffee breaks with Sven, Ozan, Waqas, Siyi and Wenda, to the discussions with Daniele, Giorgio, Maria, Bea and Alessandro who all have always been there if one needed help or guidance no matter how busy they were.

I would also like to thank my dear friends who constantly had my back and helped me through my days. Specially, Rossiza and Shailja who made my stay in the Netherlands a lot happier and memorable. This list is very long, so I would leave it at this, in order to not miss anybody out by mistake.

And finally, I would like to thank my parents and my little sister and dedicate this thesis to them who always supported me in every stages of my life, and always been a Skype call away, over these past years whenever I needed comfort or guidance. Sorry that I have been quite grumpy this past months.

This thesis work is performed in the context of the Seventh Framework Program (FP7) project Concealed Object Stand-Off Real-Time Imaging for Security (CONSORTIS), grant agreement no: 312745.

Analysis and Design of Dual Band THz Imager Based on Incoherent Detectors

This thesis is submitted in partial fulfillment of the requirements for the degree of

MASTER OF SCIENCE

in

ELECTRICAL ENGINEERING

by

Shahab Oddin Dabironezare

The work presented in this thesis was performed at:

Tera-Hertz Sensing Group
Department of Microelectronics
Faculty of Electrical Engineering, Mathematics and Computer Science
Delft University of Technology

DELFT UNIVERSITY OF TECHNOLOGY
DEPARTMENT OF ELECTRICAL ENGINEERING

The undersigned hereby certify that they have read and recommend to the Faculty of Electrical Engineering, Mathematics and Computer Science for acceptance a thesis entitled **" Analysis and Design of Dual Band THz Imager Based on Incoherent Detectors "** by **Shahab Oddin Dabironezare** in partial fulfillment of the requirements for the degree of **Master of Science**.

Dated: Nov 23, 2015

Chairman: ______________________________

prof. dr. Andrea Neto

Supervisor: ______________________________

dr. Nuria Llombart Juan

Committee Member: ______________________________

dr. Rob Remis

Contents

Preface i

Acknowledgments vii

List of Figures ix

1 Introduction **1**
1.1 Sub-millimeter Radiometric Imaging for Security . . . 1
1.2 Sub-millimeter Detectors . . . 2
1.2.1 Kinetic Inductance Detectors . . . 3
1.3 Optical Imaging System . . . 4
1.3.1 Introduction to Focusing Systems . . . 4
1.3.2 Parameters of the Imaging system . . . 6
1.4 Thesis Goal . . . 12
1.5 Thesis Outline . . . 14

2 A Review on Related Background **17**
2.1 Solving Electromagnetic Problems Using Spectral Green's Function Representation . . . 17
2.2 Analysis Techniques for Focusing System . . . 24
2.2.1 Calculating Focal Field at Sub-mm Wave Frequencies Using Fourier Optics . . . 25
2.3 Conclusion . . . 28

3 Design of Absorbing Frequency Selective Surface **29**
3.1 Introduction to Frequency Selective Surfaces . . . 29
3.2 Choice of the receiver architecture . . . 31
3.3 Jerusalem Cross Frequency Selective Surface: Design Steps . . . 33
3.3.1 Design steps for the FSS operating at f_1 Frequency Band . . . 35
3.3.2 Designing steps for the FSS operating at f_2 Frequency Band . . . 37
3.3.3 Oblique Incidence Performance . . . 40
3.3.4 Low Coupling between TE/TM Modes . . . 41
3.4 Study for Finiteness Effect . . . 43
3.5 Evaluating the Performance of the Design Including the KID Resonators . . . 47
3.6 Conclusion . . . 51

4 Analysis and Performance Evaluation of the Absorber Coupled Optics **53**
4.1 Circuit Model for the Absorber Based FSS Array . . . 53
4.2 Analysis of the Focusing System . . . 60
4.2.1 Approximated Analysis Method . . . 65

4.2.2 Angular Response of Absorber Based Imaging System 68
4.3 Evaluation of System Performance 70
4.3.1 System Performance: Parabolic Reflector 70
4.3.2 System Performance: CONSORTIS Optics 73
4.4 Conclusion 77

5 Conclusion **79**
5.1 Future Research 81

Bibliography **83**

A List of abbreviations **87**

List of Figures

1.1 Two common type of KIDs: (a) Many inductive based KIDs are connected to one readout line [1]. (b) Optical micrograph of a bolometer based KID [2] . . . 4
1.2 A schematic illustration of a focusing system 4
1.3 Generic schematic for different types of reflectors. 5
1.4 Detailed geometry of a parabolic reflector. 5
1.5 Focused fields on the focal plane, incoming from different angles in the FoV. w is the length of the square shape detectors, and d_s is the distance between two detector in the array. 7
1.6 Normalized Airy pattern for $y_f = 0$ cut, as a function of x_f. 7
1.7 Shifted Airy patterns on the focal plane array. 8
1.8 Ratio of the filling factor over spill over efficiency, F_m/η_{so}, as the function of the filling factor. 11
1.9 Simplified model of the CONSORTIS optics including its focal plane. 12
1.10 Simplified schematic of the imaging scenario. 13
1.11 Structure of the FPA of the imager. The arrow indicates the axis of the mechanical scanning 14

2.1 An example of the stratified structure and its equivalent transmission line. . . . 19
2.2 An equivalent transmission line with an electrical elementary source at $z = z'$. . 20
2.3 A 2D periodic array and replacing it with an array of equivalent currents. 21
2.4 Example of an equivalent transmission line with electrical elementary source at $z = z'$ 24
2.5 The focusing system and its equivalent replacement. 25
2.6 Detailed geometry of a parabolic reflector 27

3.1 Incident field on a scattering object and the scattered field cause by that excitation. 30
3.2 Incident and scattered fields at resonance frequency for an infinite dipole array. 30
3.3 Typical FSS geometries. 31
3.4 Initial proposed structure for the kinetic inductance bolometer based FSS. (a) Side view, (b) top view, (c) unit cell. 32
3.5 Real and imaginary parts of the sheet resistance of the superconductive resonator lines. 33
3.6 Jerusalem cross FSS unit cell and its geometrical parameters. 33
3.7 Geometry of a Jerusalem cross FSS. The parts indicated by the red color resonate, when the structure is excited by a horizontally polarized wave. 34
3.8 Equivalent transmission line model of an infinite periodic array. 35
3.9 Transmission line model for TE and TM fields, with the back short. 36
3.10 Absorption efficiency of the infinite array of f_1 absorbers with indicated operation and rejection bands. 37
3.11 Real and imaginary parts of the impedances in the infinite array of f_1 absorbers. 37

3.12 Power absorption efficiency of infinite array of f_2 FSS structure. 38
3.13 Real and imaginary impedance parts of infinite array of f_2 FSS structure. 39
3.14 Continues strip line absorber and its geometrical parameters. 39
3.15 Comparison between the absorption efficiency of a broadband absorber and a JC FSS based absorber with the same period and sheet resistance. 40
3.16 Absorption efficiency of f_1 and f_2 absorbers in scanning for TE and TM modes separately. 41
3.17 Coupling between TE and TM modes for different scanning angles for both the absorber based FSS and the PEC based. 42
3.18 A plane wave impinges on a surface with a certain direction of propagation. . . 43
3.19 1D array which is finite in x, and it is infinite in y. 44
3.20 Comparison between the absorbed power by the infinite array and a 1D array, finite in x and excited by a vertically polarized plane wave coming from the broadside, for continuous dual polarized strip line array. 45
3.21 Comparison between the absorbed power by the infinite array and a 1D array, with $n = 4$ and excited by a horizontally polarized plane wave for continuous dual polarized strip line array. 45
3.22 Effective length as a function of the physical length at different frequencies. . . 46
3.23 1D array of Jerusalem cross which is finite in x, and it is infinite in y. 46
3.24 Power absorbed over a 1D finite array of JC FSS v.s. the power absorbed over the same physical area in an infinite array of JC FSS. 47
3.25 Absorption efficiency of the free standing FSS design v.s. the same design including the dielectric layer and the resonator lines. 48
3.26 Input impedance of the FSS design (Z_{FSS}) for free standing v.s. with layer and resonator lines. 48
3.27 An example of comparison between the absorption efficiency of a bent and not bent JC. 49
3.28 Bent JC for the f_1 design. 49
3.29 Design parameters of the absorbers with resonator lines. 50
3.30 Absorption efficiency for both the horizontal and vertical excitations. 50

4.1 The direct field impinging on the FSS array. 54
4.2 Equivalent circuit model of the absorber based FSS. 55
4.3 Transmission line representation of the absorber based FSS. 55
4.4 Thevenin equivalent circuit from AA' terminal in the transmission line model. . 57
4.5 Comparing absorption efficiency of MATLAB code and CST simulation for both f_1 and f_2 absorbers with scanning angle of $\theta = 30^o$ and $\phi = 25^o$ 58
4.6 Geometry of an absorber with focus on the absorbing part (orange color). . . . 59
4.7 Comparing total absorbed power of the structure, considering coupling (blue) or not (red) 60
4.8 Geometry of a parabolic reflector and its focal plane. 61
4.9 Finite array of designed FSS as the detectors in the FPA, (a) f_1 type, (b) f_2 type. 61
4.10 Incident plane wave coming from broadside and direct field represented as a PWS. 62
4.11 FSS response as a function of k_x when $k_y = 0$ for both TE and TM modes for f_1 absorber at the center of its operation frequency band. The marked region is the limitation on the spectral domain. 63
4.12 Normalized amplitude of the total electrical field in x direction compared to the direct field and the Airy pattern, at the focal plane of the imager, at f_1 frequency for the f_1 detector 64
4.13 Finite array of FSS unit cells as a detector on the FPA 64

4.14 Z_{tot} as a function of x_f when $y_f = 0$ compared to the $Z_{FSS}(0,0)$ for f_1 absorber at f_1 frequency. 66
4.15 Representation of the fields focused by the quasi-optical system on the FSS array: (a) $\theta_{FoV} = 0$, (b) $\theta_{FoV} \neq 0$. 68
4.16 Angular response of the imager in comparison to the response of a uniformly illuminated reflector, for f_1 detector with different sizes at f_1 frequency. 69
4.17 Normalized value of the resolution for different detector sizes, at f_1 frequency. 70
4.18 Discussed efficiencies for the detectors using the free standing FSS design. The green and red areas correspond to the operational and rejection bands, respectively. 71
4.19 Angular response of the imager calculated as a function of positions in the FoV, compared to the one of a uniformly illuminated reflector. 72
4.20 Discussed efficiencies for the design introduced in section 3.5. The green and red areas correspond to the operational and rejection bands, respectively. 73
4.21 Comparison between the possible incidence angles of plane waves coming to the edge and central detector at the FPA of CONSORTIS optics. 74
4.22 Angular response of CONSORTIS imager for the detector, compared to the magnified version of the direct field 75

Chapter 1

Introduction

1.1 Sub-millimeter Radiometric Imaging for Security

Imaging systems for security applications are widely used to detect hazardous objects and materials such as: weapons, explosives, illegal drugs and chemical and biological agents [1,3,4]. Over a long time, the security systems at airports have being using x-ray metal detectors [5]. However in the recent years, there is an increasing interest in exploiting mm-waves and sub mm-waves for detection of objects under clothing. By using these wavelengths, it is possible to obtain images at a relatively good spatial resolution while allowing penetration through material. Moreover, due to the non-ionizing characteristic of the millimeter and sub-millimeter waves, the health risks are reduced in comparison to x-ray radiation.

The current state of the art of mm-wave security systems are portal based systems, which use active imagers working around $30GHz$ frequency band. These images are acquired digitally with post processing algorithms [6,7]. Such systems can obtain an image with the sufficient resolution when they are operating at a very short distance from their target. In some cases, it is desired that the security system is placed at a larger distance from the target for a more operational flexibility. Therefore, the security system should be able to maintain its spatial resolution from farther distances. This requirement is possible by operating at higher frequencies which enables the usage of larger antennas in terms of the wavelength. Moreover, the penetration length of the sub-mm waves is still sufficient to detect objects concealed behind cloths, and also objects inside typical packages [8]. The above points show the importance and possibilities in using sub-mm based security systems, it also explains the significant interest of researchers toward developing such systems in the recent years.

One of the main parameters in an imaging system is the image acquisition speed. In security applications, in order to capture the moving targets and cover a large field of view (FoV), the system should be able to have a high image acquisition speed. In millimeter wave systems, this requirement is achieved using phased arrays and digital beam forming for stationary targets [9]. However, in the sub-mm regime, acquiring the image digitally, using phased arrays, requires a very large number of transceivers with a very accurate phase control over the whole array. At the moment, the technology required for such systems is not available. Therefore, in the sub-mm regime, the solution of acquiring the image using a quasi-optical system is widely used. Such imagers behave as cameras, which use focusing systems such as lenses or reflectors to generate the image. Therefore, in this approach the quality of the image is determined by the optics. This solution removes the need for phased arrays in the system.

Sub-mm imaging systems can be divided in two categories: *Active* and *Passive* systems. In active imagers, transmitter and receivers are placed at the focal plane of the focusing system. The system transmits signals to the target and receives the signal that comes back, similar to radar systems. By using a frequency modulated continuous wave (FMCW) radar scheme, it is possible to generate 3D images, an example of such system is presented in [10]. On the other hand, passive imagers or radiometers, measure the emission from the black-body source [3, 4, 11, 12]. The black-body radiation of an object is related to the temperature of the object. Due to the passive operation of these systems (i.e. no active illumination is used), they are considered to be less intrusive in comparison to their active counterparts. However, in a passive imager there is not much control over the radiation intensity of the source. Therefore, in order to distinguish the actual radiations of the target from the environment noise, detectors with high sensitivity and wide band coupling mechanisms are required. Multi-band passive imagers provide the possibility of detecting objects at multiple frequency bands. The thermal effects show different responses at different frequencies. Therefore, a multi-band imager can obtain more information from the object in comparison to a single-band imager. The extra information can be used to increase the probability of detection, and improve the material differentiation for the security imaging.

1.2 Sub-millimeter Detectors

Typically, two types of detectors are available: *coherent* and *incoherent* detectors [13]. Coherent detectors measure both the amplitude and phase information of the incoming signals. Since at THz frequencies low noise amplifiers are not available, coherent detectors use heterodyne scheme with low noise mixers. Heterodyne receivers mix the incoming signals with the signal from the local oscillator in order to down convert the signal to lower frequencies. The down conversion operation continues until the frequency is suitable to perform demodulation. Some of the coherent detector examples at THz frequencies are: the superconductor-insulator-superconductor (SIS) tunnel junction mixers [14, 15], hot-electron bolometer (HEB) mixers [16], and the Schottky diode mixers [17, 18]. However, at THz frequencies, the system suffers from low power sources and higher costs in comparison to millimeter wave systems. Therefore, a good image quality is more difficult to achieve.

Another solution is the incoherent or direct detection. In the direct detection, electromagnetic (EM) waves are absorbed by a material, causing variations in its physical properties. One can measure these variations to obtain the information on the incoming EM waves. In the direct detection, only the amplitude information of the signal can be obtained. Direct detectors are categorized based on the physical properties they exploit: semiconductor detectors measure the behavior of excited electrons, which are pushed out of their valance band by THz radiations [19]; superconducting bolometers such as transition edge sensors (TES) [20, 21] measure changes in the material properties when the metal shifts between the normal and superconducting states; and superconducting detectors that measure changes in the properties of a superconductor material which requires to keep the operational temperature of the system below the critical temperature of the superconductor. The kinetic inductance detector (KID) [22] and the superconducting tunnel junction (STJ) [23] are two examples of superconducting direct detectors.

Superconducting detectors are the most sensitive type among the mentioned ones. In the past, individual superconductive bolometers were widely used [24, 25]. However, in order to increase the image acquisition speed, the number of detectors required in these systems should increase significantly. Therefore, typical detector geometries in the past based on TES or bolometers are difficult to extend to arrays with a large number of elements. On the other hand, The simple readout mechanism of the KID allows the possibility of having a larger number of detectors in the imager, [26].

1.2.1 Kinetic Inductance Detectors

The inductance based KID is a specific type of kinetic inductance detector which is used in space observation applications [22, 27]. In inductance based KIDs, THz radiations change the density of the Cooper pairs inside a volume of the superconducting material. This change in the number of quasi-particles in the superconducting material increases the kinetic inductance (L_k) of the material. Therefore, the complex impedance of the material changes. In order to sense the small changes in L_k, the superconductor material should resonate at a certain frequency with a very large quality factor (Q factor). To achieve this goal, the superconductor is designed as a meandering coplanar wave guide (CPW) which resonates at a low GHz frequency. To achieve the resonance, the length of the line should be half or a quarter of the wavelength. Due to small losses in a superconducting material, the quality factor of the mentioned structure is very large. Resonator is then coupled to a CPW read-out line. Therefore, at the corresponding GHz frequency, a sharp deep is visible in the read-out. When THz radiations are absorbed on the superconductor, the Q factor of the resonator decreases, which leads to wider deeps in the readout line. In addition, the resonance frequency shifts toward lower frequencies. Therefore, by linking the amount of power absorbed on the lines with the mentioned variations in the resonance properties, one can have a direct detector. The advantage of using a CPW read out line is that one can connected many KIDs with slightly different resonator lengths to one readout line. Each detector in an imager can be assigned to a KID resonator with a specific resonating frequency. At the readout, the response of all the detectors are gathered in term of deeps in the frequency domain. In conclusion, a KID can obtain the response of several detectors with just one read out line, Fig. 1.1a.

The coupling of the incoming radiation into the KIDs is commonly possible by two different approaches. In antenna based KIDs, the incoming plane waves are guided into the superconducting lines using antennas. The advantage of this approach is the possibility of designing the antenna and the KIDs separately. On the other hand, the absorber based KID (Lumped element kinetic inductance detector (LEKD)) uses specific materials that absorb radiations at THz frequencies and behave as a superconductor at GHz frequencies. Typically, these absorbers are broad band and absorb radiations in a large THz frequency band.

The inductance based KID requires an operation temperature in the order of a few hundred milli-Kelvin. Another possible KID based detector is a hybrid between bolometers and KIDs, which is refereed to as the bolometer based KID [2] . This structure exploits the relation between the kinetic inductance and the temperature of the superconductor. Using the same mentioned method, the bolometer based KID, uses deeps in the Q factor, to measure how much THz radiation is absorbed on the structure in terms of heat. In other words, bolometer based KID behaves similar to a thermometer. The main advantage of the bolometer based KIDs to the inductive based is the possibility of operating at higher temperatures in the order of a few kelvin (i.e. 5-10 kelvin) [2]. This temperature can be achieved by commercial coolers. However, the Q factor in the bolometer based KID is lower than the Q factor of the inductive based KID. Therefore, a lower number of detectors can be connected into one readout line. Moreover, a bolometer based KID requires a membrane to absorb the THz radiations in terms of heat. The membrane should be thermally isolated from the substrate, which introduces complexity in the fabrication of the detector. Fig. 1.1b illustrates a membrane which is supported by several legs to realize the thermal isolation . Another limitation introduced by a bolometer based KID is the thermal time constant of the membrane. Thermal time constant indicates how fast a membrane can absorb the heat on its surface. Larger membranes have a longer time constant. Therefore, the response speed of these detectors is inversely proportional to their physical size.

In this thesis work, bolometer based KIDs are used as the incoherent detector of the imaging system. In order to couple the incoming fields into the superconducting lines, a frequency

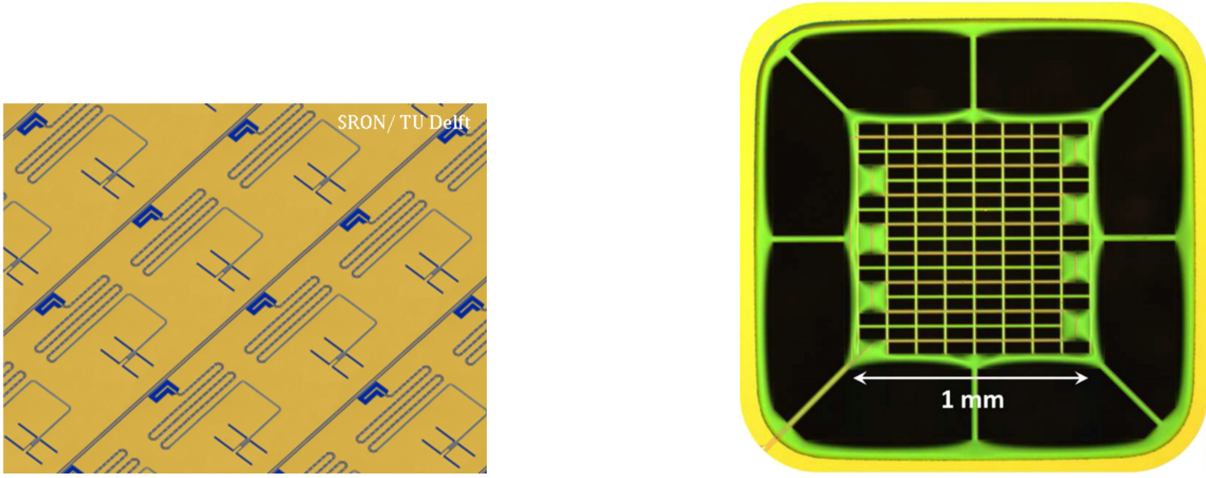

(a) (b)

Figure 1.1: Two common type of KIDs: (a) Many inductive based KIDs are connected to one readout line [1]. (b) Optical micrograph of a bolometer based KID [2]

selective surface (FSS) is used on top of the bolometer based KID. Therefore, two separate layers are located in the detector architecture.

1.3 Optical Imaging System

1.3.1 Introduction to Focusing Systems

A focusing system consists of a reflector or lens, which focuses the incoming waves on the focal plane. In Fig. 1.2, this principle is shown for a case in which the field coming to the reflector is represented as a plane wave coming from broadside direction. Since typically, a lens based focusing system behaves similar to a reflector based system, in this section only the reflector based focusing systems are discussed.

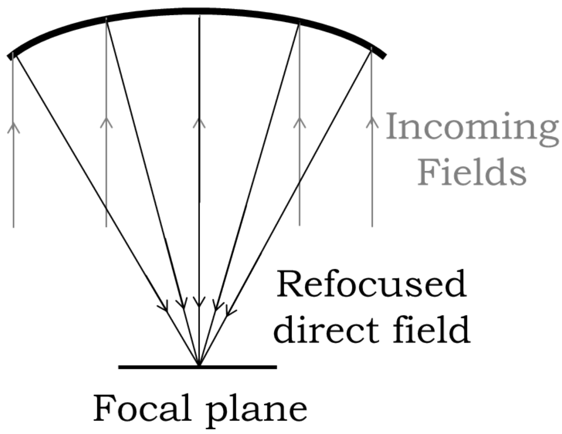

Figure 1.2: A schematic illustration of a focusing system

In general, two types of reflector shapes are common, the elliptical reflectors Fig. 1.3a, and the parabolic reflectors, Fig. 1.3b. In the figures, D is the diameter of the reflector, R is the distance from the first focus to the apex of the reflector, and in the case of the elliptical reflector, R_f is the distance of the second focus point from the apex. The relation between the two focus distances in a elliptical reflector is called the magnification factor, and can be expressed as

$$M = \frac{R_f}{R} \tag{1.1}$$

In the optical based imagers, the detectors are placed at the first focal plane, closer to the reflector. The signal received by each of the detectors is associated to a pixel in the image. This array of detectors is referred to as the focal plane array (FPA). The target plane is at the second focus point, or at infinity for the parabolic reflector case. The area at the target plane which illuminates the FPA is called the field of view (FoV).

For space observation applications, the target plane is at infinity. Therefore, the parabolic reflectors are used. On the other hand, since the target is at a finite distance from the system for security imaging applications, the elliptical reflectors are typically used. The relation between

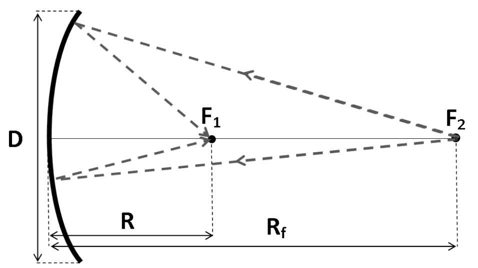

(a) Elliptical reflector.

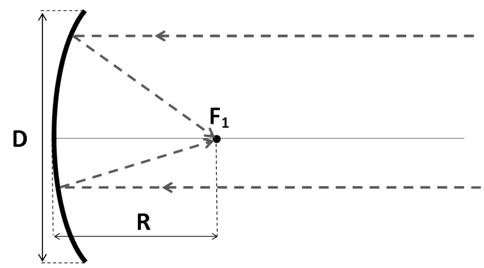

(b) Parabolic reflector.

Figure 1.3: Generic schematic for different types of reflectors.

the diameter of a reflector and the focal distance is a common parameter in the optical systems, which is referred to as the f-number, $f_{\#}$. The f-number is expressed as

$$f_{\#} = \frac{R}{D} \tag{1.2}$$

In Fig. 1.4, θ_0 is the subtended rim angle of the focusing system. θ_0 could be calculated geometrically as [28]:

$$\theta_0 = 2acot(4f_{\#}) \tag{1.3}$$

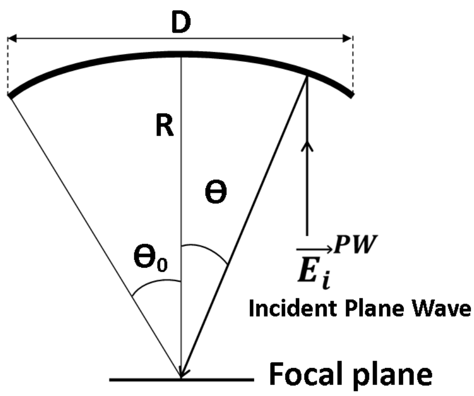

Figure 1.4: Detailed geometry of a parabolic reflector.

For electrically large reflectors, the far field generated a parabolic reflector can be approximated by the Fourier transform of its aperture field. This approximation can be expressed as [29]

$$\vec{E}_{far}(\theta_t, \phi_t) = FT\{\vec{e}_{ap}(x_{ap}, y_{ap})\} = \vec{E}_{ap}(k_x, k_y) \tag{1.4}$$

Where $\vec{E}_{far}(\theta_t, \phi_t)$ is the far field generated by the parabolic reflector as a function of elevation, θ_t, and azimuth angle, ϕ_t, in the spherical coordinates. The field at the aperture of the reflector is $\vec{e}_{ap}$, and $\vec{E}_{ap}$ represents its spectral form. The spectral components of the wave vector, $\vec{k}_t = k\hat{t}$, are $k_x = k\sin(\theta_t)\cos(\phi_t)$ and $k_y = k\sin(\theta_t)\sin(\phi_t)$. The near field generated by an elliptical reflector, $\vec{E}_{near}$, with a large R_f/D, also has a similar relation with the field on its aperture. However, such near field is compressed in the spectral domain by the term R_f. This can be demonstrated using a Fourier optics approximation [29]. The near field can be expressed as

$$\vec{E}_{near}(\theta_t, \phi_t) = \vec{E}_{ap}(\frac{k_x}{R_f}, \frac{k_y}{R_f}) \tag{1.5}$$

Since this relation is valid for both magnetic and electrical near fields at the target plane, the near field of such elliptical reflector has similar properties to a far field. In other words, the magnetic and electrical fields are orthogonal to each other, and they are related to each other by the free space impedance. In conclusion, from a certain boundary condition related to R_f/D [29], the focusing properties of an elliptical reflector can be approximated by the properties of a parabolic reflector. In this thesis, the above condition is assumed to be valid. Therefore, in order to evaluate the properties of the absorber based KIDs under an optical system, the elliptical reflector is approximated by a parabolic reflector.

1.3.2 Parameters of the Imaging system

Sampling of the FPA

The field at the focal plane of a parabolic reflector consists of radiation contributions from each angle in the FoV. In order to distinguish the contribution of each angle in the target plane, the field at the focal plane should be properly sampled. The sampling is possible by putting several detectors in the focal plane. Each detector, due to its position and size, absorbs only a part of the focal field, and therefore it can be related to a pixel in the image. In this section, in order to define the sampling, the Airy pattern approximation for the spatial distribution of the fields at the focal plane is used.

For a focusing systems with a large $f_\#$, when the reflector is illuminated from broadside, $\theta_{FoV} = 0$ (see Fig. 1.5a), the field at the focal plane can be approximated as the Airy pattern [29]. This is discussed in details at Section 2.2.1. An Airy pattern can be expressed as

$$AP(\rho_f) = \frac{J_1(k\rho_f/2f_\#)}{k\rho_f/2f_\#} \tag{1.6}$$

Where $AP(\rho_f)$ is a function of the cylindrical positions at the focal plane, ρ_f, and k is the propagation constant: $k = 2\pi f/c$, and c is the speed of light in the medium. J_1 is the Bessel function of the first kind of the order one. The amplitude of the focal field is proportional to $|AP(\rho_f)|$. The normalized Airy pattern for any frequency and $f_\#$ is illustrated in Fig. 1.6. The half power beam width (HPBW) (i.e. the $-3dB$ threshold) of the Airy pattern can be expressed as

$$HPBW = 2x_f|_{-3dB} = \lambda f_\# \tag{1.7}$$

As it was mentioned in Section 1.3.1, the field at the focal plane of the focusing system can be related to the Fourier transform of the spectrum of its aperture field. For small angles of incidence, θ_{FoV}, the aperture field can be approximated by the aperture field generated by broadside illumination with an extra linear phase term. A linear phase term in the spectral domain is equivalent to a translation in the spatial domain. Therefore, it is possible to approximate the

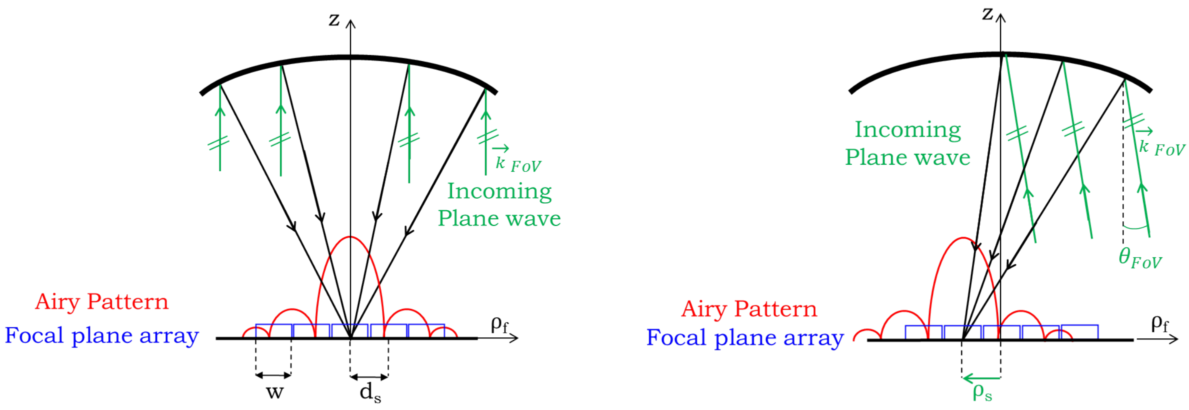

(a) Plane waves incoming from broadside to the detector at the central of the array.

(b) Plane waves incoming from an oblique direction, θ_{FoV}, to a position in the FPA.

Figure 1.5: Focused fields on the focal plane, incoming from different angles in the FoV. w is the length of the square shape detectors, and d_s is the distance between two detector in the array.

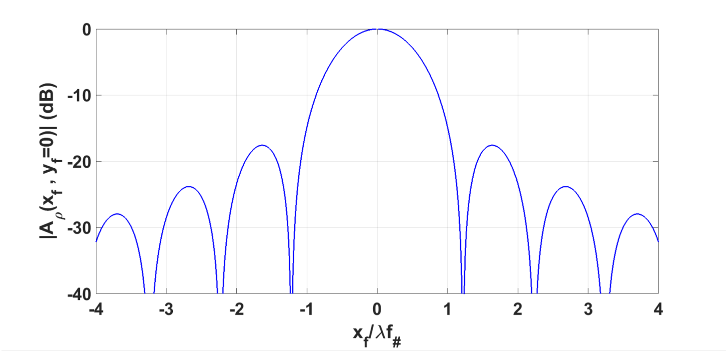

Figure 1.6: Normalized Airy pattern for $y_f = 0$ cut, as a function of x_f.

field focused at the focal plane from different angles of incidence in the FoV as shifted version of the Airy pattern, $AP(\vec{\rho}_f - \vec{\rho}_s)$, Fig. 1.5. The translation value can be expressed as

$$\vec{\rho}_s = \frac{R}{k_0}\vec{k}_{\rho FoV} \tag{1.8}$$

Where $k_{\rho FoV} = k_0 \sin(\theta_{FoV})$, and R is the distance of the parabolic reflector apex from its focus.

Using the above approximation, it can be assumed that when the detectors are placed in the FPA, they receive a certain portion of the field generated by each direction in the FoV, θ_{FoV}. The sampling rate, d_s, is defined as the distance between two neighboring detectors on the FPA. If the sampling rate is chosen based on the HPBW threshold in the Airy pattern, this sampling rate is referred to as the full or coherent sampling rate. This sampling rate is expressed as [29]

$$d_s^{coh} = \lambda f_\# \tag{1.9}$$

The fields at the focal plane associated to the consecutive samples will then crossed at -3dB as shown in Fig. 1.7. Incoherent detectors reconstruct the image using the absorbed power and not the field itself. The absorbed power is proportional to the amplitude of the focal field to the power of two. Therefore, the HPBW of the function $|AP(\rho_f)|^2$ should be considered. The latter is half of the HPBW of $|AP(\rho_f)|$. As a result, it is common to use the half sampling rate for incoherent detectors, as [29]

$$d_s^{incoh} = 0.5\lambda f_\# \tag{1.10}$$

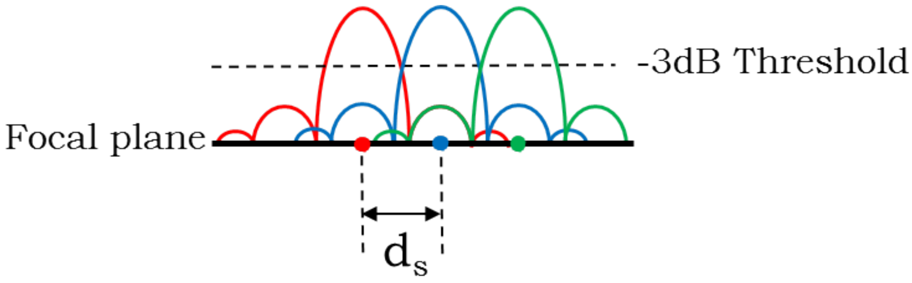

Figure 1.7: Shifted Airy patterns on the focal plane array.

In general form, the sampling rate can be formulated as:

$$d_s = s\lambda f_{\#} \tag{1.11}$$

Where s indicates the relation between the full sampling rate and the implemented one.

If a squared shaped detector is used, its area is: $A_{det} = w^2$. The relation between the detector length, w, and the full sampling rate can be expressed as

$$F_m = \frac{w}{d_s^{coh}} = \frac{w}{\lambda f_{\#}} \tag{1.12}$$

Where F_m is introduced as the filling factor. If there is not a sufficient number of detectors to fully sample the FPA, a mechanical scanner in the optics is introduced to generate the full image. The missing pixels are obtained by mechanically steering the beams of the optical system [29]. The mechanical scanning is achieved by rotating a small mirror in the optics or by rotating the focusing system itself. Moreover, this allows the detectors to be designed with larger dimensions than the limit introduced by the implemented sampling rate. Larger detectors can absorb a bigger portion of the field on the FPA, which can improve the sensitivity of the detectors.

Image Acquisition Speed

The mechanical scanning can be implemented using different schemes. The speed of a mechanical scanning scheme is limited by the rotation speed of its motors. Therefore, the cost of the mechanical scanning is associated to the acquisition speed of the image. As an example, one dimensional (1D) mechanical scanning is faster than a two dimensional (2D) one when both schemes use comparable rotation motors. If the imaging speed is kept constant, then the imager must observe a certain point in the FoV for a shorter time than a system with no mechanical scanning. This time is referred to as the integration time, τ_i, of the imager. Larger integration time decrease the image acquisition speed of the system, but increase the sensitivity of the detectors. However, as it was mentioned before, the bolometer based KIDs use a membrane to absorb radiations in terms of heat, and such membrane has a minimum time response. This time response is referred to as the thermal time constant of the membrane, τ_t. Therefore, the integration time of the imager can not be lower than τ_t. In the extreme case, τ_i is chosen equal to τ_t. In addition, τ_t becomes larger as the detector area increases, i.e. the system becomes slower.

For a system with a certain FPA size equal to $L_x \times L_y$, the number of needed detectors for the sampling rate, d_s, is

$$N_p = \frac{L_x}{d_s} \cdot \frac{L_y}{d_s} \tag{1.13}$$

When a mechanical scanning scheme is used, the number of actual present detectors is lower, and referred to as N_d. N_d and N_p are related by the fact that some samples are missing in FPA, and they are compensated by using the mechanical scanning. This is expressed by the scanning factor, F_s, as

$$F_s = \frac{N_d}{N_p} \tag{1.14}$$

If a certain imaging speed is chosen, f_{image}, the integration time for the fully sampled array is $\tau_i = 1/f_{image}$. Using the above discussions, the integration time for the sparse array is

$$\tau_i' = F_s \tau_i \tag{1.15}$$

Therefore, if one wants to keep the imaging speed constant, the integration time will be reduced by a factor of F_s.

Sensitivity of the System

The quality of an image is directly related to the contrast between the received signal power and the noise power in the system. The noise equivalent temperature difference (NETD) gives an estimation of the imaging system performance. It is defined as minimum detectable temperature of the system given a certain integration time or imaging speed. The NETD is related to the system noise via the NEP and the received power P_r as:

$$NETD = \frac{NEP}{dP_r/dT\sqrt{\tau_i}} \tag{1.16}$$

Where NEP is the noise equivalent power, P_r the power received , T is the operating temperature and τ_i the integration time of the imager. A larger integration time means that the system receives radiation from an angle in the FoV for a longer period of time. However, as it was mentioned before, the integration time is related inversely to the image acquisition speed. Therefore, to achieve a high imaging speed, the integration time is limited to a certain value. In a passive imager, the source power is fixed by the expression for the intensity of the black body radiation, and the optical system efficiency. Moreover, to improve the NETD of the imager for real time applications, low noise detectors, i.e sensitive detectors are required. It is common to assess the quality of a detector with the term sensitivity. The sensitivity determines the ability of the detector in resolving between the noise and the actual radiated power from the target. Therefore the sensitivity has an inverse relation with the noise power generated in the detector.

The power received from an incoherent source can be expressed as

$$P_r = \int \int_{\Omega_s} B(f,\theta,\phi) A_{eff}(f,\theta,\phi) d\Omega df \tag{1.17}$$

where $B(f,\theta,\phi)$ is the angular Brightness distribution of the source and Ω_s its solid angle; and $A_{eff}(f,\theta,\phi)$ is the effective area of the imaging system (i.e. optics plus detectors) as function of the angular direction. This effective area can be expressed as

$$A_{eff}(f,\theta,\phi) = A_r \eta_o F_a(\theta,\phi) \tag{1.18}$$

with A_r being the reflector aperture area, η_o the optical efficiency (including possible losses) and $F_a(\theta,\phi)$ the normalized pattern of the imager (which corresponds to the response of the imager to a point source).

When estimating the sensitivity of the imager, it is convenient to assume an incoherent source distributed over the whole hemisphere with a constant angular distribution. Moreover, since $\frac{hc}{\lambda} \ll k_B T$, the Brightness frequency dependence can be simplified in the Rayleigh-Jeans limit. In such cases, the Brightness simply is

$$B(f) = \frac{2f^2 k_B T}{c^2} \tag{1.19}$$

Where k_B is the Boltzman constant. Therefore, using the above equation, Eq. (1.17) becomes

$$P \approx \int \frac{2k_B T}{\lambda^2} \int_\Omega A_{eff}(f,\theta,\phi) d\Omega df \tag{1.20}$$

Resorting to standard antenna concepts, one can express $\int_\Omega A_{eff}(f,\theta,\phi)d\Omega = \eta_o \lambda^2$. As a result, it can be observe that the power received basically depends only on the frequency integral of the optical efficiency:

$$P \approx 2k_B T BW \eta_o^{avg} \tag{1.21}$$

where we have explicitly shown the dependency on the bandwidth by introducing an optical efficiency average over that same bandwidth:

$$\eta_o^{avg} = \frac{1}{BW} \int_{f_0-BW/2}^{f_0+BW/2} \eta_o(f) df \tag{1.22}$$

Therefore, we can estimate the NETD as

$$NETD = \frac{NEP}{2\eta_o^{avg} k_B BW \sqrt{\tau_i}} \tag{1.23}$$

The parameter which is usually employed to quantify the noise of the system is the noise equivalent power (NEP). In bolometer based KIDs, there are different noise source. In particular the KIDs developed for CONSORTIS [30] are limited by the phonon noise which has a NEP of

$$NEP = \sqrt{4k_B T^2 G} \tag{1.24}$$

Where G is the thermal conductivity. By following the steps given in [31], on can express the NEP as

$$NEP = 2w\sqrt{k_B T^2 C_0/\tau_t} \tag{1.25}$$

Where w is the length of the squared shaped detector, and C_0 is the heat capacity constant of the membrane. Using the relation between the full sampling rate, d_s^{coh}, and the filling factor, F_m, (see Eq. (1.12)) the NEP is expanded to

$$NEP = 2F_m f_\# \lambda \sqrt{k_B T^2 C_0/\tau_t} \tag{1.26}$$

Therefore, for the CONSORTIS detector, we can express the NETD as by substituting Eq. (1.26) in Eq. (1.23), as

$$NETD = \lambda f_\# \frac{F_m}{\eta_o^{avg}} \frac{1}{BW} f_{image} T \sqrt{\frac{2\pi C_0}{k_B}} \tag{1.27}$$

In sparse arrays, mechanical scanning is used. Therefore NETD can be expressed as

$$NETD = \lambda f_\# \frac{F_m}{\eta_o^{avg}} \frac{1}{BW} \frac{f_{image}}{F_s} T \sqrt{\frac{2\pi C_0}{k_B}} \tag{1.28}$$

A sensitive thermometer has a low NETD value. In this work, to improve the sensitivity, the focus is on having a high optical efficiency over a large BW.

Optimization of the FPA Structure

Using Eq. (1.28), one should design the geometrical parameters of the FPA structure in a certain way to minimize the NETD. For sampling rates lower than $2\lambda f_{\#}$, the optical efficiency can be directly approximated by the spill over efficiency. The spill over efficiency indicates how much power is intercepted by the detectorThe latter can be calculated as the ratio between the amount of power focused on a detector to the total power focused over the focal plane.

$$\eta_{SO} = \frac{\iint_{A_{det}} |E|^2 ds}{\iint_{-\infty}^{\infty} |E|^2 ds} \tag{1.29}$$

Where A_{det} is the area of the detector, and $|E|$ is the amplitude of the field at the focal plane. The filling factor is equal to $\frac{w}{\lambda f_{\#}}$. Therefore, the spill over efficiency is directly a function of the filling factor. This relation indicates that the term F_m/η_o in Eq. (1.28) should have an minimum value when it is plotted as a function of the detector size for a specific $f_{\#}$. In Fig. 1.8, the term F_m/η_o is computed for different filling factor values, when the optical efficiency is approximated by the spill over efficiency. The figure indicates that F_m/η_o has a minimum at $F_m = 1$. The position of this minimum is independent of the selected $f_{\#}$. However, the NETD dose depend on $f_{\#}$. This is associated to the fact that the thermal constant of the detectors is proportional to its physical dimension. Since the NETD is proportional to $\frac{f_{\#}}{BW}$, in order to have the same NETD for different f-numbers, the operation bandwidth of the imager has to change accordingly. Indeed the larger is the $f_{\#}$, a larger BW is needed to obtain the same sensitivity. By having a larger number of detectors in the FPA, a smaller portion of the pixels in the image will be obtained by the mechanical scanning. Therefore, the integration time improves, which leads to a lower NETD. This relation is shown by the scanning factor term, F_s, in Eq. (1.28).

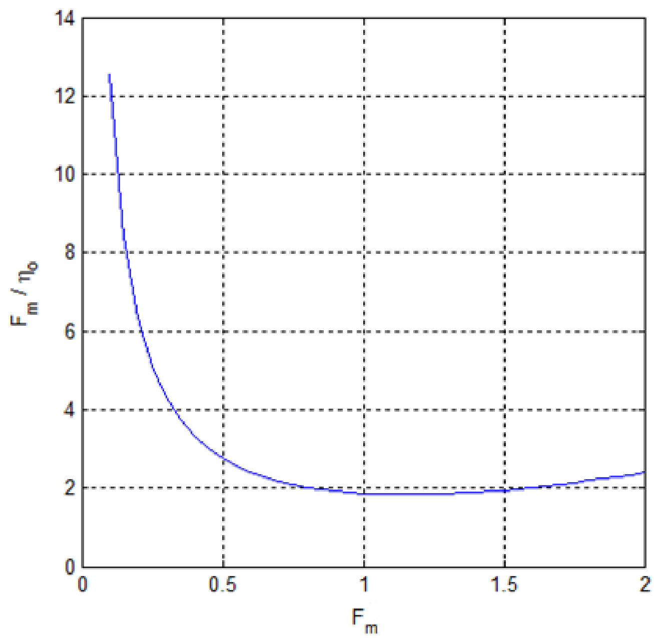

Figure 1.8: Ratio of the filling factor over spill over efficiency, F_m/η_{so}, as the function of the filling factor.

1.4 Thesis Goal

In the project CONSORTIS (Project code: FP7-security) [32], an imager for security applications is desired which should combine a passive and an active system to increase the probability of detection. This thesis focuses on the passive system. The passive system is an incoherent dual band THz imager. To construct the passive image, a dual band system is introduced which should receive radiations at two different frequency bands. Through out this thesis, the central frequency of these two bands are refereed to as f_1 and f_2, when $f_2 = 2f_1$. The radiation at the two bands must be received separately. Afterward, the image is constructed using the thermal information acquired from both bands. The system should be able to image a human size target at a certain distance from the imager, with certain required resolution.

Since the large focal plane in a lens doses not block the target plane and using reflectors with the same properties need a more complicated optical system, in the CONSORTIS the optical system is a lens. The simplified model of the CONSORTIS optics and the related optical parameters of the system are indicated in Fig. 1.9. The magnification factor of this optical system is $M = 8.33$ and f-number equal to 2. However, in most of this thesis, the focusing system is simplified as a parabolic reflector with the same $f_{\#}$. Therefore, the FoV is assumed to be located at the far field region, Fig. 1.4.

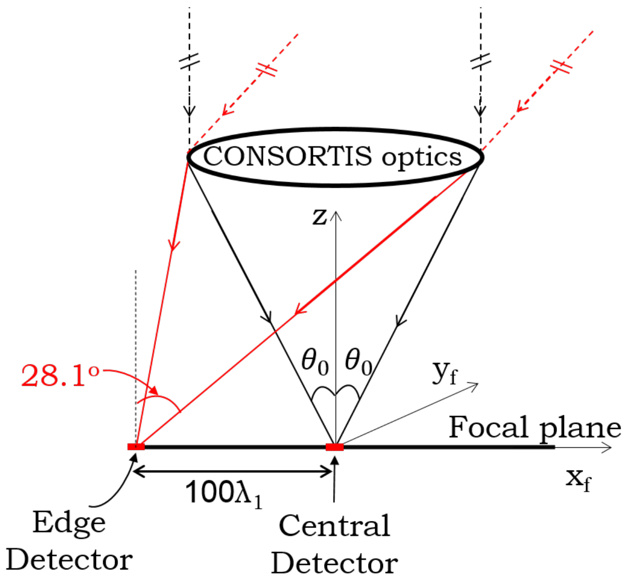

Figure 1.9: Simplified model of the CONSORTIS optics including its focal plane.

As it was mentioned earlier, the KID structure is suitable for developing a large number of detectors in the focal plane. The imaging system in this project uses the bolometer based KIDs, introduced in [2]. The superconducting resonator lines in the KID should be coupled to both f_1 and f_2 frequency bands. This is achieved by using a frequency selective surface (FSS) layer on top of the lines. The FSS absorbers only the corresponding band in terms of heat, and couples the generated heat into the superconductor lines using thermal coupling [2]. Moreover, the FSS reflects the unwanted band of THz radiations. Due to fabrication limits, only one layer of FSS can be fabricated on a membrane based technology. Since it is necessary to receive radiations from each band separately, two different FSS based KIDs are needed. Therefore, two types of detectors are in the FPA. Each type of such detectors consist of a finite array of the designed FSS unit cells. The Jerusalem cross element is chosen as the unit cell of the FSS absorber. This imaging scenario is illustrated in Fig. 1.10.

Using the discussion on NETD, the structure of the dual band FPA was optimized in [33]

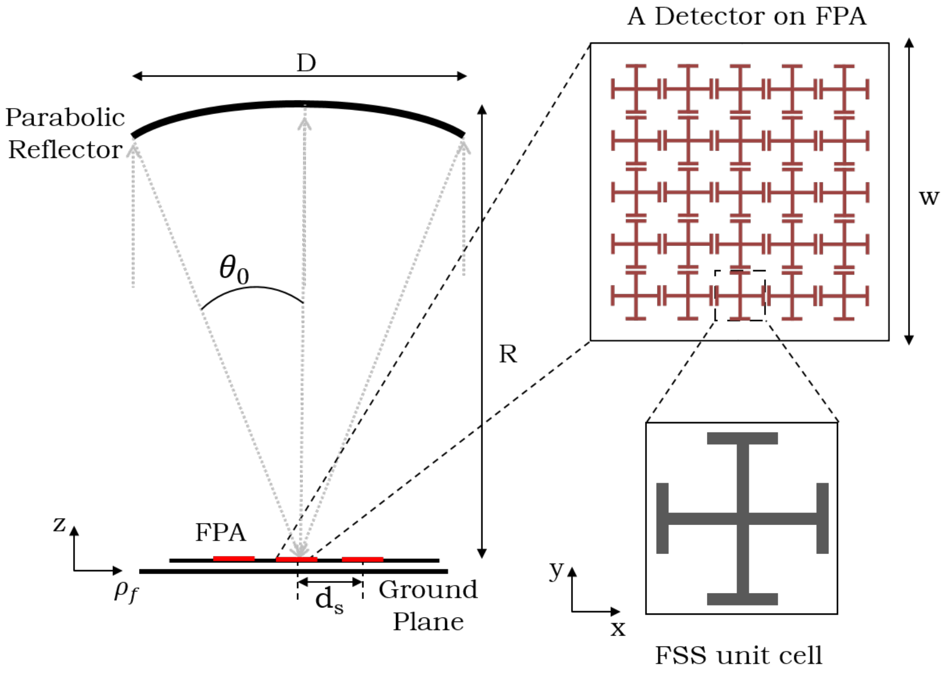

Figure 1.10: Simplified schematic of the imaging scenario.

as shown in Fig. 1.11. Since the number of realizable detectors on the FPA is lower than the amount needed, a sparse array of detectors with diagonal 1D mechanical scanning is used. The number of the required samples in the FPA is computed using Eq. (1.13). In order to keep the complexity low, the mechanical scanning is introduced as a diagonal scan. The axis of such scanner is also indicated in Fig. 1.11. As it is visible in the figure, this decision leads to a less complex mechanical scheme, since the mirror on the optical system only needs to rotate in one direction. As it can be seen in the figure, f_2 detectors are placed on the FPA in such a way that mechanical scanning in one axis covers the missing pixels for the both detector types. By choosing the scanning factor, F_s, the total number of the actual detectors present in the FPA can be calculated (see Eq. (1.14)). In Table 1.1, the defined system parameters of the imager are reported. These parameters are chosen based on the requirements of the project and the provided discussions [33].

The goal of this thesis is to design the required dual band FSS based absorbers and evaluate its performance and impact on the optical performance of the imager. To achieve this goal, firstly, a FSS based KID is designed. Secondly, a spectral analysis tool to characterize the detector and the focusing system is provided. Finally, the total system performance of the imager including both the detector and the focusing system is investigated, using the provided analysis tool.

Table 1.1: The provided parameters of the imaging system.

	Detectors operating at f_1 band	Detectors operating at f_2 band
Bandwidth of operation	0.9 octave	0.9 octave
Bandwidth of rejection	0.9 octave	0.9 octave
Detector size (w)	$1.25\lambda_1$	$1.5\lambda_2$
Sampling rate (d_s)	$1.22\lambda_1$	$1.22\lambda_2$
f-number ($f_\#$)	2	2
Maximum angle of incidence	$\simeq 28.1^o$	$\simeq 28.1^o$
Maximum rim angle (θ_0)	$\simeq 15^o$	$\simeq 15^o$
Maximum tolerable NETD	1 K	1 K

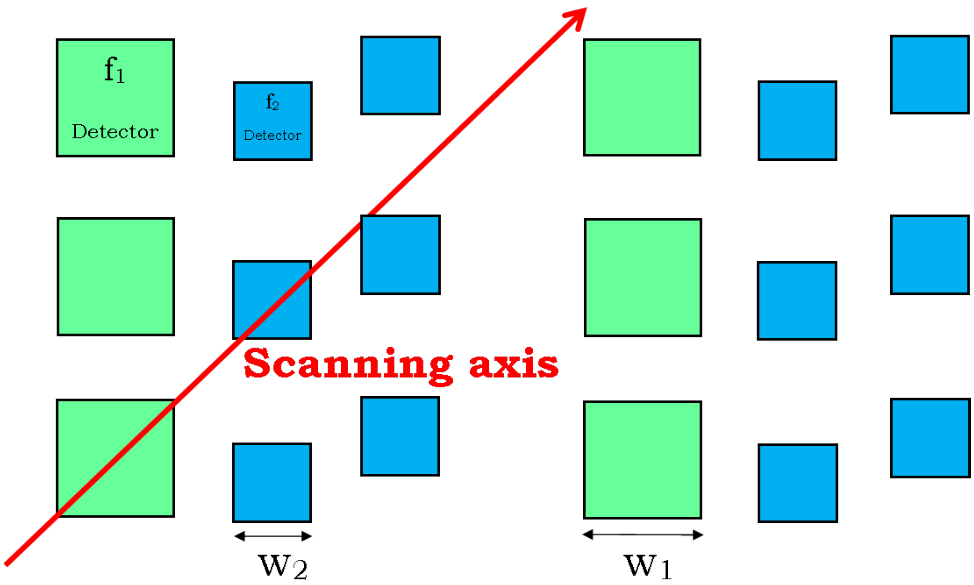

Figure 1.11: Structure of the FPA of the imager. The arrow indicates the axis of the mechanical scanning

1.5 Thesis Outline

This thesis consists of five chapters including the introduction and the conclusion chapters. The second chapter focuses on the background needed to analysis a periodic structure under a focusing system. In this chapter, the spectral analysis for a generic periodic structure is provided. Moreover, the Fourier optic analyze tool is discussed and used to calculate an expression for the focal field generated by a focusing system.

In the third chapter, FSS structures are introduced, and the FSS based absorber required for this particular application is designed. In addition, by removing the assumption of the infinite structure and including the KID lines behind the FSS layer, the performance of the proposed design in two more realistic situations is investigated.

In chapter 4, a circuit model for the absorber based FSS is introduced. This circuit model is used to evaluate the absorbed power on the FSS structure for a generic plane wave incident on the structure. The field at the focal plane of the focusing system is represented as a summation of the incoming plane waves from different angles. Therefore, the introduced circuit model can be used, for each incoming plane wave to evaluate the optical efficiency of the imager. Finally, the chapter focuses on evaluating the total system performance while both detectors and the focusing system are included. The pattern in reception of the imager, and the resolution are determined using this evaluation.

As a conclusion, chapter 5 summaries the main points of the thesis, and provides the possible future research topics to improve the work done in this thesis.

Chapter 2

A Review on Related Background

An imaging system consists of two main parts: the focusing system and the focal plane array. The focusing system and the FPA can be analyzed together if the fields in both parts are represented in the spectral domain. This chapter describes the most well-known spectral analysis methods for each parts. Chapter 4 will then combine both procedures to provide an overall evaluation on the performance of the system.

In Section 2.1, a discussion is included on analyzing the response of a passive periodic structure to an incoming plane wave, in the spectral domain. Moreover, Section 2.2 focuses on obtaining a spectral plane wave representation of the fields at the focal plane of a focusing system.

2.1 Solving Electromagnetic Problems Using Spectral Green's Function Representation

A typical electromagnetic (E.M) problem consists of a set of known sources in a certain location in space, and the electric and magnetic fields generated by these sources. The relation between the sources and the fields can be shown by the Maxwell's equations. These equations are expressed in phasor domain as

$$\vec{\nabla} \times \vec{H} = j\omega\varepsilon\vec{E} + \vec{J} \tag{2.1}$$

$$\vec{\nabla} \times \vec{E} = -j\omega\mu\vec{H} - \vec{M} \tag{2.2}$$

$$\vec{\nabla} . \vec{E} = \frac{\rho}{\varepsilon} \tag{2.3}$$

$$\vec{\nabla} . \vec{H} = -\frac{\rho_m}{\mu} \tag{2.4}$$

Where $\vec{E}$ and $\vec{H}$ are the electric and magnetic fields generated by electrical and magnetic current sources, $\vec{J}$ and $\vec{M}$. The electric and magnetic charge densities are ρ and ρ_m, respectively. ε and μ, are the electromagnetic permittivity and permeability of the medium, respectively. The magnetic current and charge density are artificial components. They are added to Maxwell's equations for symmetry, and their usefulness in solving some E.M problems using equivalent sources. The Maxwell's equations (2.1) to (2.4) are valid for every point in space.

For complex geometries, such as stratified mediums, solving the Maxwell's equations directly is not straightforward. Therefore, the Green's functions (GF) are used to rewrite the same equations and solve such E.M problems. A Green's function is a dyad, $\tilde{g}(\vec{r}, \vec{r}')$, which represents an electrical or magnetic field, at a certain point in the space, $\vec{r}$. The field is generated by an elementary electrical or magnetic source, $\delta(\vec{r} - \vec{r}').\hat{p}$, located at $\vec{r}'$, orientated in the $\hat{p}$ direction.

In other words, the Green's function allows a direct relation between the known source and the unknown field in an specific geometry in space. An arbitrary current distribution can be represented by many elementary current sources in different positions in space, $\vec{r}'$, with different amplitudes. Therefore, using the superposition theorem, a field generated by an arbitrary current source in an specific structure, can be calculated using an integral convolution over all the space domain between the Green's function of that structure and the current source as [34]

$$\vec{f}(\vec{r}) = \tilde{g}(\vec{r}) * \vec{C}(\vec{r}) = \iiint_V \tilde{g}(\vec{r}-\vec{r}')\vec{C}(\vec{r}')d\vec{r}' \tag{2.5}$$

Where $\vec{C}(\vec{r})$ is an arbitrary current source, and $\vec{f}(\vec{r})$ is the corresponding generated field.

By knowing the Green's function for a specific structure, for any current source distribution, one can calculate the electric and magnetic fields. However, other than free space, calculating the Green's function for different geometries in the spatial domain is not possible analytically. Therefore, Green's functions are typically introduced in the spectral domain for specific configurations.

Spectral Green's Function

The spectral Fourier transform is similar to the frequency Fourier transform. The latter is a relation between time and frequency, and the former is a relation between positions in space and the plane wave vector. The 1D spectral Fourier transform is defined as

$$f(x) = \frac{1}{2\pi}\int_{-\infty}^{\infty} F(k_x)e^{-jk_x x}dx \tag{2.6}$$

Where $f(x)$ is in the space domain, and $F(k_x)$ is its spectral Fourier transform (FT). The same formula can be used to calculate the 2D Green's function.

$$\tilde{g}(\vec{r}) = \frac{1}{4\pi^2}\iint \tilde{G}(k_x,k_y,z,z')e^{-jk_x x}e^{-jk_y y}dk_x dk_y \tag{2.7}$$

Where $\tilde{G}(k_x,k_y,z,z')$ is the 2D Green's function in the spectral domain, k_x and k_y are the spectral domain representation of the spatial values, x and y. The condition for going from a 3D spectral domain FT to a 2D one is by defining k_z as [34]

$$k_z = \sqrt{k^2 - k_x^2 - k_y^2} \geq 0 \tag{2.8}$$

Where k is the propagation constant of the medium: $k = 2\pi/\lambda$, and λ is the wavelength in the medium.

In the spectral domain, the convolution integral in Eq. (2.5) can be expressed as a multiplication. Therefore, the electrical field can be expressed as

$$\vec{E}(\vec{r}) = \frac{1}{4\pi^2}\int_{-\infty}^{\infty}\int_{-\infty}^{\infty} \tilde{G}^{ej}(k_x,k_y,z,z')\vec{J}(k_x,k_y)e^{-jk_x x}e^{-jk_y y}dk_x dk_y \tag{2.9}$$

Where $\vec{J}(k_x,k_y)$ and $\tilde{G}^{ej}(k_x,k_y,z,z')$, are the spectral Fourier transforms of the current and the Green's function, respectively.

Spectral Green's Function for Stratified Media

Since stratified structures are very common in the integrated technology, the tools to analyze such structures using Green's functions are well developed [35]. These tools use an equivalent transmission line representation to calculate the Green's functions analytically in the spectral domain for the stratified media.

It is common in the electromagnetic theory to separate a plane wave into transverse electrical and magnetic fields. In a plane wave, both the electric and magnetic fields are orthogonal to the direction of propagation. The propagation vector, $\hat{k}$, and the surface normal vector, $\hat{n}$, form a plane in the space. The part of the electric field that is normal to this plane is referred as the transverse electrical, TE, field (E_{TE}) and the part of the magnetic field that is normal to the plane is referred to as transverse magnetic, TM, field (H_{TM}). The magnetic TE field, H_{TE}, and electrical TM field, E_{TM}, are defined in such a way to include the remaining part of the E.M fields. Therefore

$$\vec{E} = \vec{E}_{TE} + \vec{E}_{TM} \tag{2.10}$$

$$\vec{H} = \vec{H}_{TE} + \vec{H}_{TM} \tag{2.11}$$

The problem is separated in TE and TM fields, and the layered structure is modeled as a series of transmission lines. The structure should be homogeneous in the transverse plane. As an example, a stratification is shown in Fig. 2.1. A material with dielectric constant ε_{r2} is placed in between two layers of a dielectric with ε_{r1}. The upper layer is infinite in $+z$ direction. Whereas, the bottom layer is grounded by a ground plane. The characteristic impedance of the equivalent transmission lines can be expressed as [36]

$$Z_{TM} = \eta \frac{k}{k_z} \tag{2.12}$$

$$Z_{TE} = \eta \frac{k_z}{k} \tag{2.13}$$

Where η is the wave impedance in the material, and $kz = \sqrt{k^2 - k_x^2 + k_y^2}$.

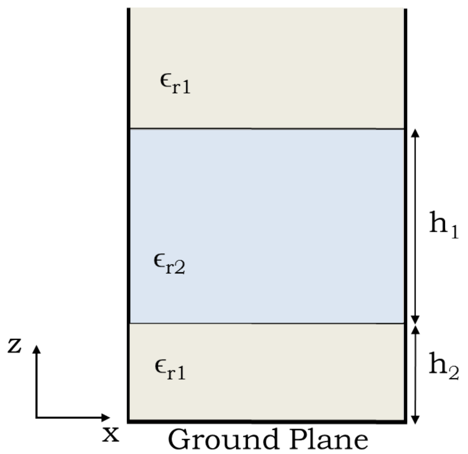

(a) The stratified structure.

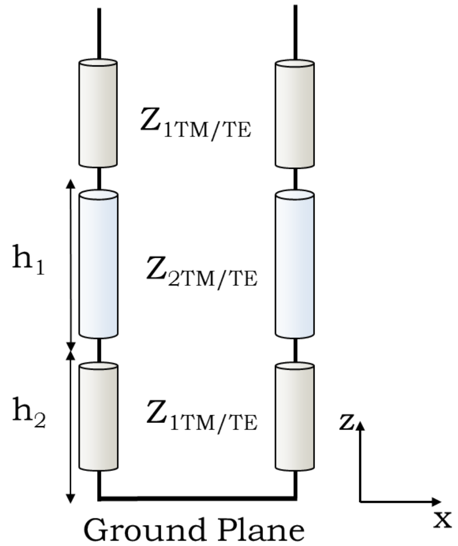

(b) The equivalent transmission line.

Figure 2.1: An example of the stratified structure and its equivalent transmission line.

By introducing the normalized current or voltage transverse sources to the equivalent transmission line, one can calculate the spectral Green's function. The spectral GF is a function of the source location, positioned at $z = z'$, and it is used to calculate the fields at a certain position, z_0: $\tilde{G}^{ej}(k_x, k_y, z_0, z')$. The positions z' and z_0 are shown in Fig. 2.2. As an example, for an elementary electrical source in x direction, the electrical field in x can be calculated using the spectral Green's function:

$$E_x = \frac{1}{4\pi^2}\int_{-\infty}^{\infty}\int_{-\infty}^{\infty} G_{xx}^{ej}(k_x,k_y,z_0,z')e^{-jk_x x}e^{-jk_y y}dk_x dk_y \tag{2.14}$$

Where $G_{xx}^{ej}(k_x,k_y,z_0,z')$ is [36]

$$G_{xx}^{ej}(k_x,k_y,z_0,z') = -\frac{\upsilon_{TM}k_x^2 + \upsilon_{TE}k_y^2}{k_\rho^2} \tag{2.15}$$

Where υ_{TM} and υ_{TE} are voltage solutions of TM and TE transmission line at z_0 position, and $k_\rho = \sqrt{k_x^2 + k_y^2}$.

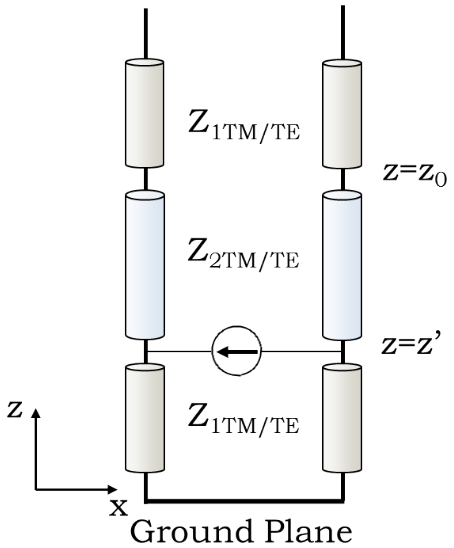

Figure 2.2: An equivalent transmission line with an electrical elementary source at $z = z'$.

Periodic Green's Function

A periodic 2D structure consists of an array of identical elements at a certain distance from each other, which is called the period distance, d_x and d_y, Fig. 2.3a. Analyzing such structures with method of moment in the spectral domain requires a massive number of unknowns, which is time and resource consuming. Therefore, another approach is necessary. The tools for analyzing such periodic structures are well developed and discussed in [36–38]. As a first approximation the array is assumed to be infinitely large. In this section, for an array of elements in transmission, periodic Green's function is introduced. Secondly, the discussion is used to analyze an array in reception.

If each element of the array is excited by a current source, these sources can be replaced by equivalent currents. The elementary equivalent current for a 2D array in x-y plane at $z = 0$, is defined as [36]

$$\vec{J}_\infty(x,y,z) = \sum_{n_x=-\infty}^{\infty}\sum_{n_y=-\infty}^{\infty} \delta(x-n_x d_x)\delta(y-n_y d_y)\delta(z)e^{j\beta_x}e^{j\beta_y}\hat{p} \tag{2.16}$$

Where n_x and n_y are the element indices in x and y, d_x and d_y are the periods of the array in x and y, and $\hat{p} = p_x\hat{x} + p_y\hat{y}$ is the orientation of the current, Fig. 2.3b. The terms $e^{j\beta_x}$ and $e^{j\beta_y}$

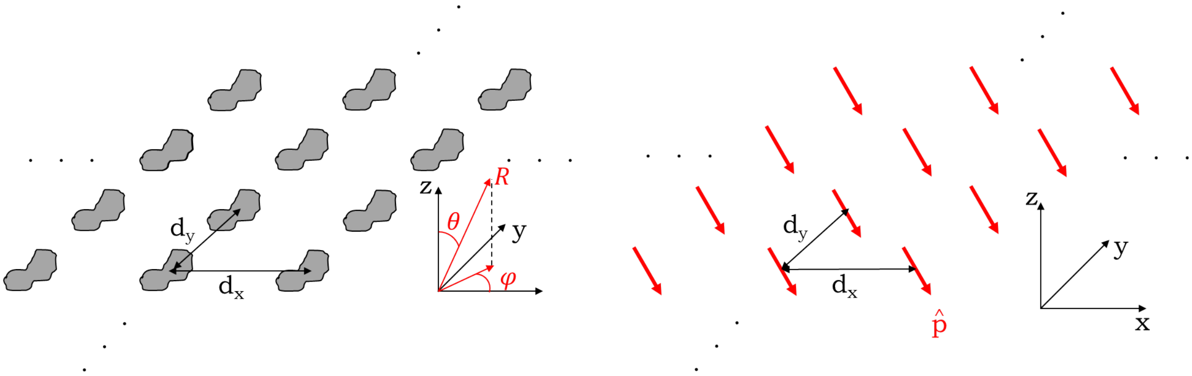

(a) A planar periodic structure in $x-y$. **(b)** Array is replaced by elementary currents.

Figure 2.3: A 2D periodic array and replacing it with an array of equivalent currents.

are the progressive phase shifts of the current sources. When scanning in elevation angle θ, and azimuth angle ϕ, is desired. This phase shifts are defined as:

$$\beta_x = -k_{x0} n_x d_x \tag{2.17}$$

$$\beta_y = -k_{y0} n_y d_y \tag{2.18}$$

Where k_{x0} and k_{y0} are:

$$k_{x0} = k \sin(\theta)\, \cos(\phi) \tag{2.19}$$

$$k_{y0} = k \sin(\theta)\, \sin(\phi) \tag{2.20}$$

Where k is the propagation constant.

One can define the periodic Green's function as the electrical field generated by a periodic set of elementary sources. The periodic Green's function for the defined elementary source, J_∞, is [36]

$$\vec{g_\infty}^{ej}(x,y,z) = \iiint_V \tilde{g}^{ej}(x-x', y-y', z-z') \vec{J}_\infty(x', y', z') dx' dy' dz' \tag{2.21}$$

Where $\tilde{g}^{ej}(x,y,z)$ is the non-periodic Green's function of the geometry, V is the total volume of the EM problem, and x', y', z' are the position of the sources in the Cartesian coordinate. Using Eq. (2.16), one can rewrite the above equation as:

$$\vec{g_\infty}^{ej}(x,y,z) = \\ \sum_{n_x=-\infty}^{\infty} \sum_{n_y=-\infty}^{\infty} \iiint_V \tilde{g}^{ej}(x-x', y-y', z-z') \delta(x'-n_x d_x) \delta(y'-n_y d_y) \delta(z') e^{-jk_{x0} n_x d_x} e^{-jk_{y0} n_y d_y} \hat{p} dx' dy' dz' \tag{2.22}$$

Following a few mathematical steps, using the δ functions properties, Eq. (2.22) can be simplified as:

$$\vec{g_\infty}^{ej}(x,y,z) = \sum_{n_x=-\infty}^{\infty} \sum_{n_y=-\infty}^{\infty} \tilde{g}^{ej}(x-n_x d_x, y-n_y d_y, z) e^{-jk_{x0} n_x d_x} e^{-jk_{y0} n_y d_y} . \hat{p} \tag{2.23}$$

Periodic Spectral Green's Function

Using Eq. (2.7), one can calculate the 2D spectral FT for periodic Green's function:

$$\vec{g_\infty}^{ej}(x,y,z) = \sum_{n_x=-\infty}^{\infty}\sum_{n_y=-\infty}^{\infty}\Big(\frac{1}{4\pi^2}\int_{-\infty}^{\infty}\int_{-\infty}^{\infty}\tilde{G}^{ej}(k_x,k_y,z)e^{-jk_x(x-n_xd_x)}e^{-jk_y(y-n_yd_y)}\Big)e^{-jk_{x0}n_xd_x}e^{-jk_{y0}n_yd_y}.\hat{p}dkxdky \tag{2.24}$$

Where $\tilde{G}^{ej}(k_x,k_y,z)$ is the non-periodic spectral Green's function of the structure. Following a few mathematical steps including Poisson's summation formula [39], Eq. (2.24) can be simplified as a double summation over specific points of the spectral Green's function, these spectral modes are referred as Floquet modes. The simplified expression is

$$\vec{g_\infty}^{ej}(x,y,z) = \frac{1}{d_xd_y}\sum_{m_x=-\infty}^{\infty}\sum_{m_y=-\infty}^{\infty}\tilde{G}^{ej}(k_{xm},k_{ym},z)e^{-jk_{xm}x}e^{-jk_{ym}y}.\hat{p} \tag{2.25}$$

Where m_x and m_y are indices for Floquet modes of the structure, k_{xm} and k_{ym} are Floquet modes propagation constants in x and y. The latter are introduced as:

$$k_{xm} = k_{x0} - \frac{2\pi m_x}{d_x} \tag{2.26}$$

$$k_{ym} = k_{y0} - \frac{2\pi m_y}{d_y} \tag{2.27}$$

By comparing Eq. (2.7) with Eq. (2.24), one can realize that in periodic structures double integral over all k_x and k_y spectral domain is reduced to a summation at certain points. These points are introduced as Floquet modes.

To calculate the field radiated by an array of periodic elements, the current on such structure can be introduced in a similar form as Eq. (2.16)

$$\vec{J_\infty}(x,y,z) = \sum_{n_x=-\infty}^{\infty}\sum_{n_y=-\infty}^{\infty} j_0(x-n_xd_x, y-n_yd_y)\delta(z)e^{j\beta_x}e^{j\beta_y}\hat{p} \tag{2.28}$$

Where $j_0(x,y)$ is the current on the central element. By using Eq. (2.25), the electrical field radiated by a periodic structure can be computed as

$$\vec{E}(x,y,z) = \frac{1}{d_xd_y}\sum_{m_x=-\infty}^{\infty}\sum_{m_y=-\infty}^{\infty}\tilde{G}(k_{xm},k_{ym},z)J_0(k_{xm},k_{ym})e^{-jk_{xm}x}e^{-jk_{ym}y}.\hat{p} \tag{2.29}$$

Where $J_0(k_x,k_y)$ is the spectral Fourier transform of the current at the central element, $j_0(x,y)$. The formulation of the current, allows a designer to focus only on a single element (unit cell) of a periodic array to analyze the structure.

In the spectral Green's function discussion, k_z was defined. For the periodic structures, it is defined the same way, as: $k_{zm} = \sqrt{k^2 - k_{xm}^2 - k_{ym}^2}$. A Floquet mode propagates, if the following condition is satisfied [36]

$$k_{xm}^2 + k_{ym}^2 \leq k_0^2 \tag{2.30}$$

Otherwise, it exponentially decays in z direction. The latter is called an evanescent mode. For a periodic structure that desires to transmit fields in the direction of θ_t and ϕ_t. Only the mode with the propagation constant of $k_{x0} = k\sin(\theta_t)\cos(\phi_t)$ and $k_{y0} = k\sin(\theta_t)\sin(\phi_t)$ must propagate.

If more modes are excited, a grating lobe could appear in the radiation pattern. Therefore, only the main Floquet mode, $m_x = m_y = 0$, must be excited.

Using the above discussions, one can calculated the maximum possible scanning angle, which ensures that only the main Floquet mode propagates, at a certain frequency and for a certain period , d_x. If $\phi = 0^o$, the maximum elevation angle for scanning can be expressed as

$$\theta_{max} = \sin^{-1}(\frac{\lambda}{d_x} - 1) \tag{2.31}$$

In addition, for a certain scanning angle and period, one can calculated the maximum frequency in which only the main Floquet mode propagates. This frequency can be expressed as

$$f_{max} = \frac{c}{d_x}(\frac{1}{\sin(\theta)+1}) \tag{2.32}$$

Where c is the speed of light.

Analsis of Periodic Structures in Reception

The analysis of periodic structures in transmission, using Green's functions was discussed in the previous sections. The same analysis can be applied in reception. In reception, the plane wave incoming toward the array, $\vec{E}_i$, induces a periodic current on the structure, Fig. 2.4. The induced current over the periodic array can be modeled similar to Eq. (2.28). Where $j_0(x,y)$ is the shape of the current on the central element. Moreover, the phase difference between the currents induced on each element is determined by the direction of the incoming plane waves, $k_{x0} = k\sin(\pi - \theta_i)\cos(\phi_i)$ and $k_{y0} = k\sin(\pi - \theta_i)\sin(\phi_i)$. Where $\vec{k_i} = k.\hat{k_i}$ is the incident propagation vector, and k is the wave number.

Using Eq. (2.33), the field scattered by the structure, Fig. 2.4, can be computed as

$$\vec{E}_s(x,y,z) = \frac{1}{d_x d_y} \sum_{m_x=-\infty}^{\infty} \sum_{m_y=-\infty}^{\infty} \tilde{G}(k_{xm}, k_{ym}, z) J_0(k_{xm}, k_{ym}) e^{-jk_{xm}x} e^{-jk_{ym}y}.\hat{p} \tag{2.33}$$

Having a combination of propagating Floquet modes means that a complex mixture of incident plane waves impinged on the structure. Therefore, for simplicity we assume that only the main Floquet mode can be received, which indicates that the period size is small (see Eq. (2.31) and Eq. (2.32)). Since, only the main Floquet mode is present, the scattered field from the structure also propagates as a plane wave in the far field region, in θ_i and ϕ_i direction.

The total field is defined as the summation of the incident and scattered fields, as

$$\vec{E}_t = \vec{E}_i + \vec{E}_s \tag{2.34}$$

The relation between the amplitude of the incident and scattered field at a certain point in space is referred to as the S-parameter of the structure. If the incoming and scattering fields are separated into TE and TM fields based on the $\hat{z} - \hat{k}$ surface (see Fig. 2.4), one can define a S-parameter matrix which relates the scattering characteristics of the array, as below

$$S = \begin{bmatrix} S_{TM-TM} & S_{TM-TE} \\ S_{TE-TM} & S_{TE-TE} \end{bmatrix} \tag{2.35}$$

Where as an example, S_{TM-TE} relates the incident TE field to the scattered TM field as

$$S_{TM-TE} = \frac{|E_s^{TM}|}{|E_i^{TE}|} \tag{2.36}$$

The S-parameter matrix is commonly used to characterize the behavior of a periodic structure. The above discussion is valid for every incoming plane waves with a certain direction of incidence, $\vec{k_i}$.

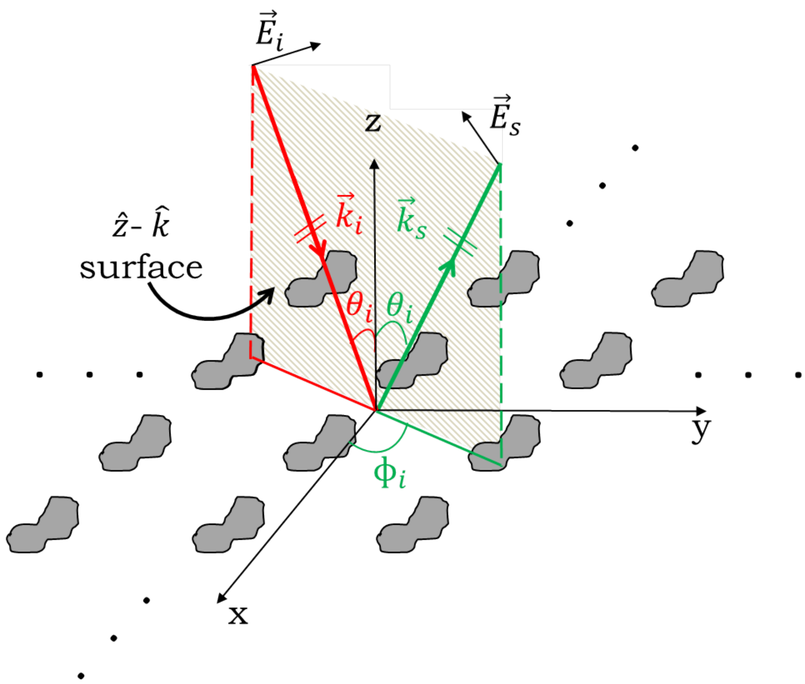

Figure 2.4: Example of an equivalent transmission line with electrical elementary source at $z = z'$

2.2 Analysis Techniques for Focusing System

There are different approaches and tools for analyzing a radiation coupling structure (antenna or absorber) under a focusing system depending on the frequency of the operation. If the size of the employed reflector or lens is in the order of the wavelength, then low frequency methods are typically used. In low frequency, the numerical methods which simulate the whole structure are not very time consuming. Therefore, tools such as finite-difference time-domain (FDTD) [40, 41], finite-elements method (FEM) [42–44], or method of moments (MoM) and integral equation (IE) [45], are common. On the other hand, for very high frequencies, i.e optical regime, scalar geometric optics (GO) is common [46].When dealing with diffraction in the system is important, more advanced models are used [47].

As for THz domain, the frequency is not high enough to go to the pure GO methods, and it is not as low as needed for numerical methods to work without being very time consuming. In this region, a method called physical optics (PO) can be used [46], which needs numerical computations on the focusing object's surface. In PO, an integration of the sources over the surface of the focusing object is used to calculate the fields scattered by the focusing system. In this approximation sources that are created by the incoming fields, are introduced the same way as if the objects surface was an infinite plane locally tangent to the object surface. Calculating the scattered fields, when the surface currents are defined, can be done with precision, using radiation integrals. Therefore, the accuracy of a PO method is directly limited by the accuracy of the introduced currents on the focusing system's surface.

Another method commonly used in optical regions is Fourier optics (FO). FO was firstly developed by E.Wolf in [48]. The main advantage of FO over PO is the ability of FO in calculating the plane wave spectrum of the field in the focal plane analytically using Fourier transforms. FO uses the approximation that the focal plane is far away from the focusing object in terms of wavelength. It has been recently proposed to evaluate absorbers under focusing systems at sub-mm wave frequencies using FO [49].

2.2.1 Calculating Focal Field at Sub-mm Wave Frequencies Using Fourier Optics

The FO approximation is valid in the optical region. On the other hand, the validity region of the FO was unclear for the THz domain. In [49], the validity region of FO for THz frequencies is discussed in detail, and the method is used to calculated the focal fields generated by focusing systems at THz frequencies. In FO, an equivalent sphere is introduced closed to the focusing system (see Fig. 2.5a). The field at the surface of the equivalent sphere propagating toward the focal plane is referred to as the aperture field, $\vec{e}_{ap}$. This field can be calculated analytically using the GO approximation for simple optical systems, or it can be obtained using computational softwares for more complicated cases. By applying the equivalence theorem, the focusing system is substituted by magnetic and electric equivalent current sources over the equivalent sphere (see Fig. 2.5b).The normal vector of the equivalent surface can be expressed as $\hat{n} = -\hat{r}'$, where $\vec{r}' = R\hat{r}'$ is the vector that indicates the position on the sphere surface. This vector can be expressed as

$$\hat{r}' = \sin(\theta')\cos(\phi')\,\hat{x} + \sin(\theta')\sin(\phi')\,\hat{y} + \cos(\theta')\,\hat{z} \tag{2.37}$$

Where $\hat{x}$, $\hat{y}$, and $\hat{z}$ are the unit vectors of the Cartesian coordinates, and θ' and ϕ' are the angles in the spherical coordinates that indicate a position on the equivalent surface. The equivalent magnetic, $\vec{m}$, and electric sources, $\vec{j}$, are expressed as

$$\vec{m} = \vec{e}_{ap} \times \hat{n} \tag{2.38}$$

$$\vec{j} = \hat{n} \times \vec{h}_{ap} \tag{2.39}$$

Where $\vec{e}_{ap}$ and $\vec{h}_{ap}$ are the electrical and magnetic aperture fields respectively.

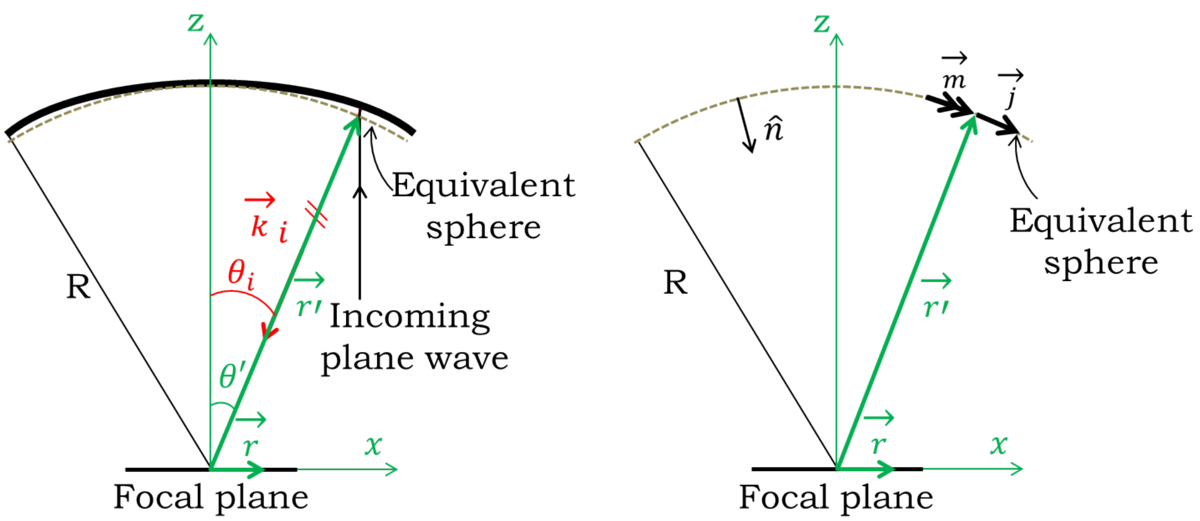

(a) 2D representation of the focusing system geometry. **(b)** Equivalent sphere and surface currents.

Figure 2.5: The focusing system and its equivalent replacement.

$\vec{e}_{ap}$ and $\vec{h}_{ap}$ are related to each other by the wave impedance, η, and they are orthogonal to each other. This relation can be expressed as

$$\vec{h}_{ap} = -\frac{1}{\eta}\vec{e}_{ap} \times \hat{k}_i \tag{2.40}$$

Where $\vec{k}_i = k\hat{k}_i$ is the wave vector of the plane wave coming toward the focal plane. When the reflector is illuminated from broadside: $\hat{k}_i = -\hat{r}'$. Therefore, the magnetic aperture field is expressed as

$$\vec{h}_{ap} = \frac{1}{\eta}\vec{e}_{ap} \times \hat{r}' \tag{2.41}$$

Using the above expressions, the equivalent magnetic and electrical surface currents for broad side illumination are calculated as

$$\vec{m} = -\vec{e}_{ap} \times \hat{r}' \tag{2.42}$$

$$\vec{j} = (\frac{1}{\eta}\vec{e}_{ap} \times \hat{r}') \times \hat{r}' = -\frac{1}{\eta}\vec{e}_{ap} \tag{2.43}$$

In the free space, using the free space Green's function, the field at observation point $\vec{r}$ generated by the electric and magnetic sources can be expressed by a radiation integral as [28]

$$\begin{aligned}\vec{e}_f(\vec{r}) = &-jk\int_s \hat{k} \times \vec{m}(\vec{r}')\frac{e^{-jk|\vec{r}-\vec{r}'|}}{4\pi|\vec{r}-\vec{r}'|}ds' \\ &- j\omega\mu\int_s \left(\vec{j}(\vec{r}') - (\hat{k}\cdot\vec{j}(\vec{r}'))\hat{k}\right)\frac{e^{-jk|\vec{r}-\vec{r}'|}}{4\pi|\vec{r}-\vec{r}'|}ds'\end{aligned} \tag{2.44}$$

Where $\hat{k} = \frac{\vec{r}-\vec{r}'}{|\vec{r}-\vec{r}'|}$, k is the wave number and $\vec{r} = x\hat{x}+y\hat{y}$ is the observation vector (see Fig. 2.5a). For observation points close to the center of the focal plane, the approximation: $\hat{k} \simeq -\hat{r}'$ is applicable. By substituting the obtained expressions of the electric and magnetic sources in Eq. (2.44), the field at the focal plane can be calculated as

$$\begin{aligned}\vec{e}_f(\vec{r}) = &-jk\int_s \hat{r}' \times (\vec{e}_{ap} \times \hat{r}')\frac{e^{-jk|\vec{r}-\vec{r}'|}}{4\pi|\vec{r}-\vec{r}'|}ds' \\ &+ jk\eta\int_s \left(\frac{1}{\eta}\vec{e}_{ap}(\vec{r}') + \left(\hat{r}'\cdot(\frac{1}{\eta}\vec{e}_{ap})\right)\hat{k}\right)\frac{e^{-jk|\vec{r}-\vec{r}'|}}{4\pi|\vec{r}-\vec{r}'|}ds'\end{aligned} \tag{2.45}$$

By simplifying the above equation, the radiation integral is expressed as

$$\vec{e}_f(\vec{r}) = jk\int_s 2\vec{e}_{ap}(\vec{r}')\frac{e^{-jk|\vec{r}-\vec{r}'|}}{4\pi|\vec{r}-\vec{r}'|}R^2\,d\Omega' \tag{2.46}$$

Where $d\Omega' = \sin(\theta')\,d\theta'\,d\phi'$. As it was mentioned, this expression is only valid for the broad-side illumination of the focusing system. By following a few mathematical steps, and performing approximations on both amplitude and phase, one can obtain the field at the focal as [49]

$$\vec{e}_f(x_f,y_f) = \frac{1}{4\pi^2}\int_{-\infty}^{\infty}\int_{-\infty}^{\infty}\vec{E}_f(k_x,k_y)e^{jk_xx_f}e^{jk_yy_f}dk_xdk_y \tag{2.47}$$

Where x_f and y_f are the spatial positions in the focal plane, $k_x = k\sin(\theta')\cos(\phi')$ and $k_y = k\sin(\theta')\sin(\phi')$. $\vec{E}_f(k_x,k_y)$ is expressed as

$$\vec{E}_f(k_x,k_y) = \frac{j2\pi Re^{-jkR}}{\sqrt{k^2-k_\rho^2}}\vec{e}_{ap}(\sin^{-1}(\frac{k_\rho}{k}),\tan^{-1}(\frac{k_y}{k_x}))circ(k_\rho,k_{\rho 0}) \tag{2.48}$$

Where the function $circ(a,b)$ equals 1 when $|a| \leq b$, and 0 otherwise, and $k_\rho = \sqrt{k_x^2+k_y^2}$. $\vec{e}_{ap}$ is the discussed aperture field. The *circ* function is introduced to implement the limitation on the radiation integral caused by the equivalent surface. This surface is limited by the maximum rim angle, θ_0, Fig. 2.6. Therefore, the spectral domain is limited by $k_{\rho 0} = k\sin(\theta_0)$. Eq. (2.47)

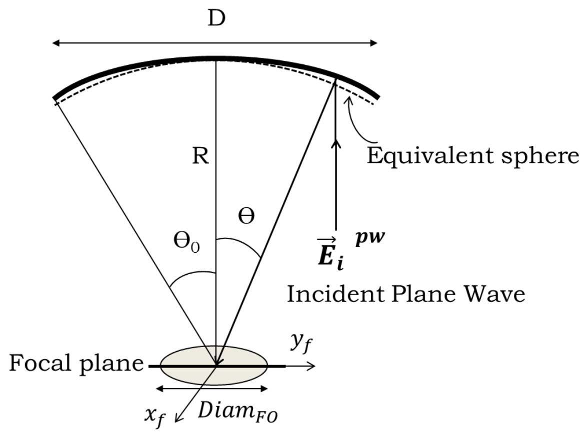

Figure 2.6: Detailed geometry of a parabolic reflector

and Eq. (2.48) indicate that the field at the focal plane of a focusing system can be calculated using the spectral Fourier transform of the aperture field.

The validity region of this method is related to the asymptotic evaluation of the discussed radiation integral. The region is determined by an area around the focus center of the reflector. This region indicates positions at the focal plane that the amplitude error is less than 10%, and phase error is less than $\pi/8$. The validity region is expressed as [49]

$$Diam_{FO} = min(Diam_{FO}^{A}, Diam_{FO}^{B}) \tag{2.49}$$

Where $Diam_{FO}$ is the diameter of a circle around the focal center where the FO is valid, Fig. 2.6, and $Diam_{FO}^{A}$ and $Diam_{FO}^{B}$ are

$$Diam_{FO}^{A} = 0.4 f_{\#} D \tag{2.50}$$

$$Diam_{FO}^{B} = f_{\#}\sqrt{2 f_{\#} D \lambda} \tag{2.51}$$

Parabolic Reflector

If a plane wave polarized along x, impinges on a parabolic reflector from broadside, the incident field can be expressed as

$$\vec{E}_i = E_0^{PW} e^{-jkz}\hat{x} \tag{2.52}$$

Where E_0^{PW} is the amplitude of the field.

Using the GO, the expression of the aperture field is driven from the incident field, using the geometrical characteristics of the parabolic reflector. Therefore, $\vec{E}_f(k_x,k_y)$ is calculated as [49]

$$\vec{E}_f(k_x,k_y) = -\frac{4\pi k R E_0^{PW} e^{-jkR}}{k_z}\frac{1}{k+k_z}\left(\frac{k_x}{k_\rho}\hat{\theta} - \frac{k_y}{k_\rho}\hat{\phi}\right)circ(k_\rho, k_{\rho 0}) \tag{2.53}$$

Where $k_z = \sqrt{k^2 - k_\rho^2}$. Eq. (2.53) is the spectral representation of the electrical field at the focal plane.

For focusing systems with a large f-number, the approximation: $k_z \simeq k$ is valid. By applying this approximation in Eq. (2.53), and solving Eq. (2.48) analytically, the field at the focal plane can be approximated as

$$\vec{e}_f(\rho_f) \simeq -\frac{jE_0^{PW} k e^{-jkR}}{2\pi R}\frac{\pi D^2}{4}\frac{J_1(k\rho_f/2f_{\#})}{k\rho_f/2f_{\#}} \tag{2.54}$$

Where the expression: $\dfrac{J_1(k\rho_f/2f_\#)}{k\rho_f/2f_\#}$, was introduced in chapter 1, as the Airy pattern.

For small angles of incidence on the reflector, the aperture field can be approximated by the broadside aperture field with an extra linear phase term. Since, the spectral Fourier transform of the aperture field is the field at the focal plane, this linear phase term is equivalent to a translation in the spatial domain. The relation between the oblique angle of incidence on the reflector and the spatial translation was already discussed in Section 1.3.2.

2.3 Conclusion

In Section 2.1, the method for analyzing a periodic structure using the Floquet mode theorem was discussed. The periodic structure in reception is also analyzed using the mentioned method. In order to characterize the relation between the incident field on the structure and the scattered field generated by the structure, the S-parameter matrix was defined. The S-parameter matrix determines the scattering characteristic of a periodic structure, when both incident and scattered fields are separated into TE and TM components of the field.

In Section 2.2, methods for analyzing a focusing system was discussed. Using the FO method within its region of applicability for THz frequency bands, the spectral distribution of the field on the focal plane of a focusing system was obtained. The validity region for this method was also discussed.

The combination of these analysis tools will lead to the possibility of evaluating the performance of the entire imaging system, including the focusing system and the detectors on the FPA. This analysis is discussed in detail at chapter 4.

Chapter 3

Design of Absorbing Frequency Selective Surface

In the European project CONSORTIS, bolometer based KIDs are used to realize a large FPA for the passive imager. As it was mentioned in Section 1.2.1, the bolometer based KIDs should be coupled to the incident field generated by the optical system. In this work, this coupling is made possible by adding a layer of absorber based frequency selective surface (FSS) on top of the superconducting resonators. The use of the absorber based FSS enables the introduction of a frequency selectivity in the response of the passive imager. In this chapter after a brief introduction on the FSS concept, two sets of FSS arrays are designed based on the CONSORTIS project requirements on the dual band imaging system. Each set is then coupled to its corresponding bolometer based KID, in order to absorb power over a certain frequency band and reject power at another band. The design steps for both FSS arrays are discussed in detail in Section 3.3. Furthermore, the performance of the designed structure is evaluated for oblique incidences. In the last sections of the chapter, in order to compare the theoretical performance with the actual system, two more realistic scenarios are investigated. Firstly, the performance of the designed array is investigated when the infinite array approximation is removed. By studying the finiteness effect on the absorber based FSS, it is shown that, when the array size is large, the effect of having a finite array is not significant due to the high losses of the absorber material and it can be neglected. The limit of this approximation is discussed. Secondly, in order to investigate the effect of having the KID resonator lines underneath the absorber based FSS, the behavior of the complete detector structure is studied. Furthermore, the effects caused by the resonator lines are compensated by modifying the FSS geometry.

3.1 Introduction to Frequency Selective Surfaces

A frequency selective surface (FSS) structure is an array of identical periodic elements. These elements could be patches or slots [50]. When an incident plane wave impinges on an array of elements, part of the field is reflected, $\vec{E}_r$, and a part is transmitted, $\vec{E}_t$. At the resonance, these structures can show a perfect transmission or reflection behavior for slot or patch based FSS, respectively. Therefore, the FSS can be used as a frequency filter for the incoming electromagnetic waves. If an object is illuminated by an incoming plane wave, it radiates a field which is called the scattered field $\vec{E}_{scat}$, Fig. 3.1. Using this terminology, the incident field (or direct field) is the field that is present in the space without including the effect of the object. The total field is the combination of the scattered and the incident field: $\vec{E}_{total} = \vec{E}_{inc} + \vec{E}_{scat}$. For example, an array of dipoles with the length of $\lambda_0/2$, where λ_0 is the wavelength at a certain frequency, f_0, resonates at f_0 in such a way that the field scattered in the transmission direction cancels out the incident field. Therefore, the field is totally reflected at f_0. In Fig. 3.2, the fields for the dipole case are shown. Such dipole arrays act as frequency filters, reflecting all the fields at the f_0 frequency with a certain bandwidth, and for the other frequencies a part of the field is transmitted and another part is reflected. In literature, it is common to show the performance of a FSS array with reflection or transmission coefficients as a function of frequency [50].

Two examples of application of such structures are: decreasing the Electromagnetic Interference (EMI) between antennas working at overlapping bands, and reducing the Radar Cross Section (RCS) of antennas, in order to reduce their visibility to Radars [51].

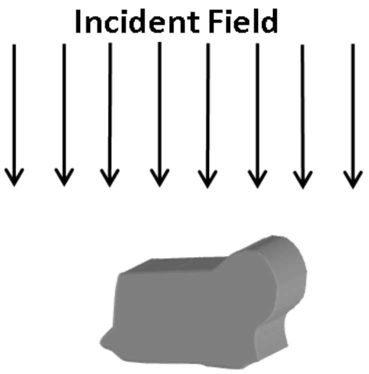

(a) Incident field incoming towards the scatterer object

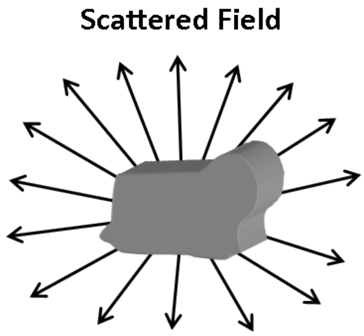

(b) Scattered field radiates from the object

Figure 3.1: Incident field on a scattering object and the scattered field cause by that excitation.

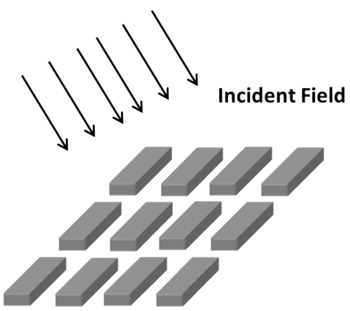

(a) Incident field

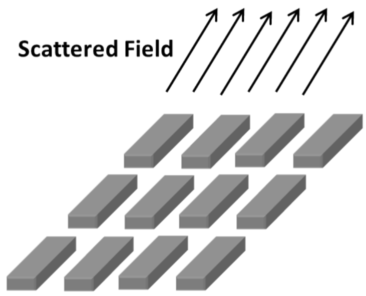

(b) Scattered field

Figure 3.2: Incident and scattered fields at resonance frequency for an infinite dipole array.

Introduction to Different FSS Geometries

In this project, the FSS will be used as a receiver in the focal plane over a radiometer. Therefore, the field coming to the imager from the field of view is unpolarized. For this reason, a dual polarized geometry is required to maximize the absorbed power. There are many possible geometries for the unit cell element of a FSS array. In Fig. 3.3, several example of dual polarized FSS unit cells are illustrated [50]. Each of these geometries show a different reflection or transmission response. As it was mentioned in Section 1.3, in this work the imager requires a dual band focal plane. Therefore, an important factor in choosing a certain unit cell shape is a fast sharp roll off in the response. Outside the desired band, the response must drop sharply in order to minimize the interference between the bands. In addition, the imager requires a wide band system. As it was mentioned in Section 2.1, in order to allow only the main Floquet mode to propagate, the array must be tightly spaced. This condition becomes more demanding as a larger maximum scanning angle is desired in the system. Therefore, the period size should be as small as possible, limiting the possible size of the unit cell.

(a) Center connected FSS elements

(b) Loop type elements

(c) Plate Type elements

Figure 3.3: Typical FSS geometries.

3.2 Choice of the receiver architecture

As it was already mentioned in Section 1.4, in order to detect objects using thermal emission, two separate frequency bands in the THz domain are used. Each of these frequency bands have a set of detectors in the focal plane. The information obtained from each frequency band is then separately processed and used to detect the target. These detectors consist of an arrays of FSS based absorbers. Therefore, two sets of absorber unit cells are needed. Each set should absorb power in a frequency band which is referred to as the operation band, and reject power at a band named the rejection band. The FSS set which operates at the band centered at f_1 frequency is referred to as the f_1 absorber, and, using the same notation, the other set of FSS based absorbers which operate at a band centered at f_2 frequency are referred to as the f_2 absorber. Moreover, every frequency data in this thesis is normalized to f_1, and all the geometric parameters in the FSS design are normalized to the corresponding wavelength, i.e. λ_1 or λ_2. Since both sets of absorbers should work without interfering with each other, the absorbers have two bandwidths: an absorption bandwidth (i.e. operation bandwidth) and a rejection bandwidth. As an example, for f_1 absorber, the rejection band is centered around f_2. The performance of these absorbers are not only evaluated by how much power they absorb in their operation band, but also in their ability to reject power in their rejection band.

The resonance behavior is directly related to the length in which an induced current can propagate on the structure. When the mentioned length is $\lambda_0/2$, the resonance occurs at that specific frequency. The Jerusalem cross (JC) element, Fig. 3.4c, has a bent design which allows a similar effective length with a smaller period in comparison to a cross dipole element (first configuration of Fig. 3.3a). Moreover, the JC has a zero in its reflection coefficient response immediately after its resonance frequency point [50], which realizes the fast roll off requirement. Therefore, the JC is chosen as the shape of the FSS unit cell for this project.

Bolometer based FSS

In this thesis work, the FSS array is used as a bolometer incoherent detector. In other words, the FSS structure uses a lossy material with low conductivity instead of using materials with a very high conductivity which can be approximated as a perfect electric conductor (PEC). Therefore, in the bolometer based FSS, the amplitude of the induced current decays as it propagates in the structure. This decay of current allows the field to be absorbed in the material in terms of heat. The result is a bolometer detector with a certain frequency response. These detectors are designed in such a way that they absorb the electromagnetic waves in a certain bandwidth and reflect or transmit at other frequencies. In the dual band scheme, the detector should absorb a large portion of the incident power in its operation band, and rejects a large portion of the incoming power at its rejection band.

Without a backing reflector, only half of the incident power can be absorbed by a bolometer based FSS, and the rest will be transmitted. Having a backing reflector insures that this transmitted power is also captured by the FSS. Therefore, typically in the THz detector applications, a backing reflector is used at a certain distance behind the FPA. The backing reflector also alters the frequency response of the array.

The bolometer based KIDs were introduced in Section 1.2.1. In Fig. 3.4, the superconductive resonator lines of such KID are shown as blue lines behind the FSS array. A thin layer of dielectric is used between the FSS and the resonator lines for support [2]. The FSS array, the resonator lines and the thin dielectric layer in between are referred to as the free standing membrane. This membrane and its effects on the speed of the imager is already discussed in chapter 1. As it is already mentioned, an important feature of a KID is its ability in using a small number of read out lines for a large number of detectors. This feature leads to a less complex FPA architecture.

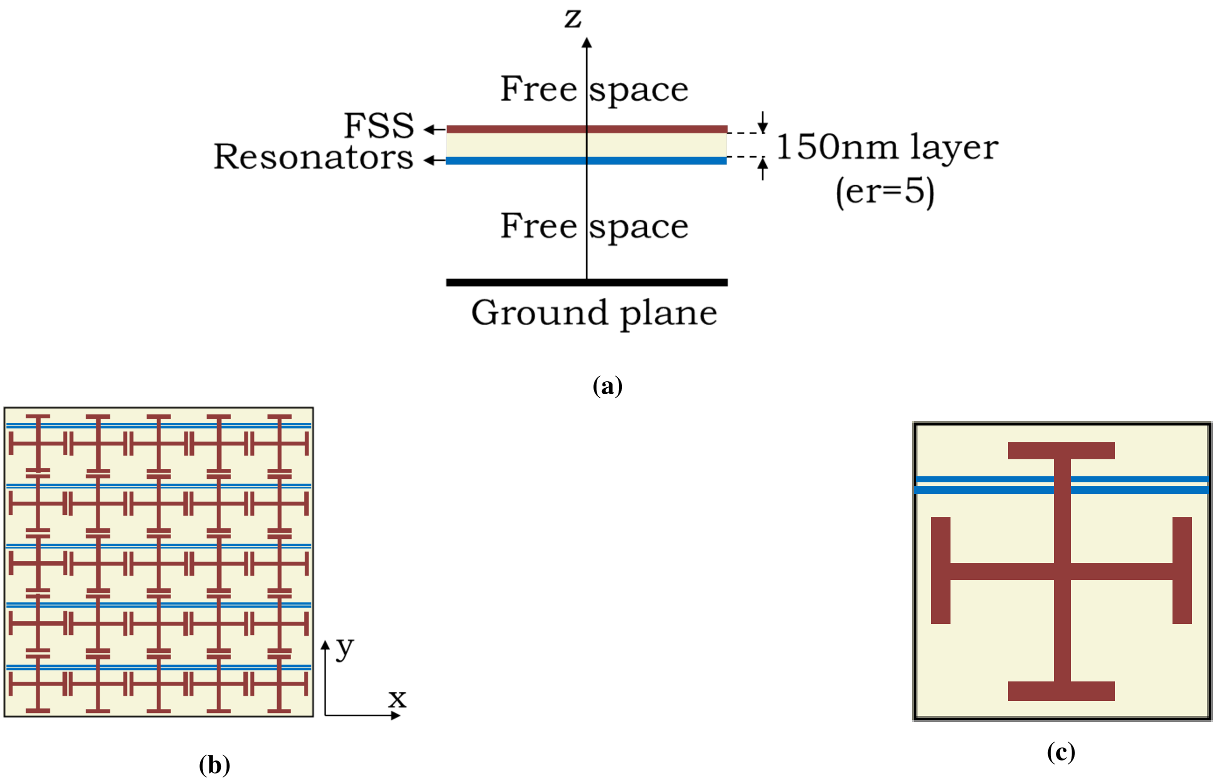

Figure 3.4: Initial proposed structure for the kinetic inductance bolometer based FSS. (a) Side view, (b) top view, (c) unit cell.

The FSS structure uses a lossy material with the sheet resistance equal to $5\Omega/square$. The sheet resistance of an absorbing material is defined as a relation between its conductivity, σ, and the thickness of the material, τ, as [52]

$$R_s \simeq \frac{1}{\sigma\tau} \tag{3.1}$$

This resistance is in general real for the material used in the FSS design. The superconducting resonator lines of KIDs also have an equivalent sheet resistance, Z_{res}, which is complex. The real and imaginary part of this impedance as a function of frequency is illustrated in Fig. 3.5. The imaginary part of Z_{res} varies considerably over the considered frequency band. This has an effect on the performance of the final design. Such effect and the procedure to compensate it are discussed in Section 3.5.

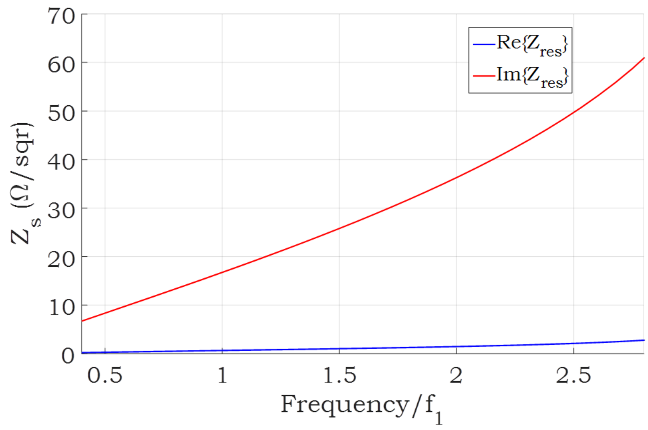

Figure 3.5: Real and imaginary parts of the sheet resistance of the superconductive resonator lines.

3.3 Jerusalem Cross Frequency Selective Surface: Design Steps

In this section, the free standing FSS unit cell is considered. The effect of having the dielectric layer and the resonator lines behind the FSS are discussed in Section 3.5. The geometrical parameters of a Jerusalem cross structure are: the length of the main arm, l, the length of the short arms, h, the width of the strips, w, the period, $d = d_x = d_y$, and the distance of the FSS from the backing reflector, h_b, Fig. 3.6.

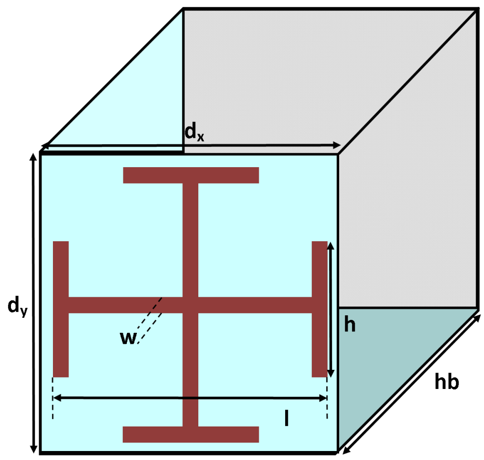

Figure 3.6: Jerusalem cross FSS unit cell and its geometrical parameters.

In the previous section, a brief introduction on the frequency selective surfaces (FSS) have been mentioned. In this section, the steps for designing the required FSS based absorber is discussed. The geometric parameters of the JC are optimized to absorb all the incident power in the operation band and have rejection of the incident power in the rejection band. In the following design steps, the approximation of the infinite array of elements is used. This approximation is introduced here, by simulating the structure with the unit cell boundary condition in the CST simulation software. The effects of having a finite array are explained in Section 3.4.

As it was mentioned in Section 3.1, the first parameter which limits the design is the period of the FSS unit cell, d_x and d_y (see Fig. 3.6). By allowing only the main Floquet mode to propagate in the structure, the performance of the array improves in terms of rejection at frequencies higher than the centeral frequency of the operation band. Based on the Floquet mode theory, in order to insure that only the main Floquet mode propagates, the following condition is required in the structure:

$$d \leq \lambda(\frac{1}{sin\theta + 1}) \tag{3.2}$$

Where θ is the elevation angle of the plane wave coming toward the array. As it was mentioned in Section 1.4, for this imager the maximum incidence angle is 30 degrees. This value is related to the maximum rim angle of the focusing system and it is the maximum incidence angle of plane waves incoming toward the detectors at the edge of the FPA. Moreover, since for the absorber working at f_1 a good rejection is required around f_2, the maximum frequency without multiple modes propagating has been chosen as a frequency higher f_2. Therefore, using Eq. (3.2), the period of the structure is chosen as $d_{f1} = \lambda_1/4$ for the $f1$ absorbers. As for the f_2 absorber a simple scaling of the geometry is sufficient: $d_{f2} = \lambda_2/4$. Since the structure is dual polarized and symmetric, from now on the periodicities in x and y are considered as equal: d=d_x=d_y.

For each polarization, the resonance of a FSS array depends on the length of its unit cell element, for the Jerusalem cross this length is $l + 2h$ (see Fig. 3.6). Since having resonance at a certain frequency with a small period size leads to a small value for l value ($l \leq d$), to compensate a large value for h should be used. However, increasing the short arm of the FSS creates another problematic effect. As an example in Fig. 3.7, focusing on one polarization (here the horizontal polarization), the part of JC FSS which contributes to the resonance is determined by the highlighted parts of the cross. The short arms have smaller lengths in comparison to the total length of the horizontal arm. Therefore, when a horizontally polarized plane wave arrives to the structure, the short arms in the vertical polarization resonate at higher frequencies than the main resonance. This additional resonance at the higher band can cause problems for the f_1 absorber, since it needs a good rejection at the f_2 band. The mentioned effect limits the maximum tolerable short arm length. In other words, one must make sure that the resonance due to the short arms stays at frequencies higher than the f_2 band. In conclusion, the reduction of the period size is limited by how much absorption at the higher band is tolerable. Furthermore, one should choose the main arm size almost equal to the period ($l \simeq d$). This allows to reduce the length of the short arms, since the resonance of the structure is given by $l + 2h$.

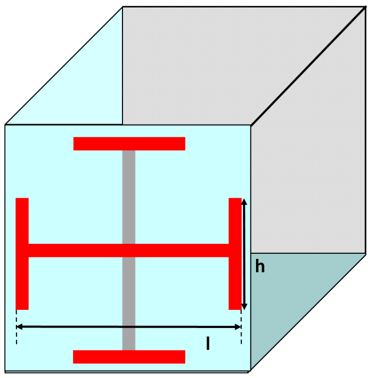

Figure 3.7: Geometry of a Jerusalem cross FSS. The parts indicated by the red color resonate, when the structure is excited by a horizontally polarized wave.

When a generic plane wave is coming toward an infinite periodic structure, it is useful to separate the field into TE and TM with respect to the normal vector of the structure (here the normal vector is chosen as z direction, see Fig. 3.4a). By separating the plane wave into the two modes, one can use an equivalent transmission line model to represent the structure, Fig. 3.8a. In this model, the voltages and currents represent the transverse value of the main Floquet mode of the electrical and magnetic fields, respectively. The FSS array can be represented by an impedance matrix which indicates the FSS effect on the TE and TM voltages and currents.

This matrix can be obtained by using a periodic based numerical method, in this project the CST simulation software is used. For the absorber based Jerusalem cross FSS, the coupling between the two modes is very low. This statement is discussed and validated in Section 3.3.4. Using this approximation, one can separate the transmission line model into TE and TM transmission line models, Fig. 3.8b, and analyze them separately.

(a) Transmission line circuit model in the general form.

(b) Transmision line model when there is no coupling between the modes.

Figure 3.8: Equivalent transmission line model of an infinite periodic array.

3.3.1 Design steps for the FSS operating at f_1 Frequency Band

In order to maximize the absorbed power, a ground plane at a certain distance, h_b, is necessary. Otherwise, at least half of the incident power would be transmitted toward the back of the structure. This can be shown using an equivalent transmission line representation for the structure. Fig. 3.9 indicates the mentioned transmission line model including a back short at the distance h_b, where Z_{FSS} represents Z_{TE-TE} or Z_{TM-TM} in Fig. 3.8b. In the figure, Z_{in} is the input impedance seen by the incoming plane wave. This impedance can be expressed as

$$Z_{in} = Z_{FSS} || Z_{gp} \tag{3.3}$$

Where Z_{gp} is the impedance of the ground plane seen from the AA' terminal [53]

$$Z_{gp}^{TM/TE} = jZ_0^{TM/TE} \tan(k_{zi} h_b) \tag{3.4}$$

Where $Z_0^{TM/TE}$ is the characteristic impedance of the TE/TM transmission line. These impedances were discussed at Section 2.1 (see Eq. (2.12) and (2.13)). In order to maximize the absorption, Z_{in} should be matched to the free space impedance.

In Fig. 3.9, the reflection coefficient looking toward the absorber is:

$$\Gamma^{TE/TM} = \frac{Z_{in}^{TE/TM} - Z_0^{TE/TM}}{Z_{in}^{TE/TM} + Z_0^{TE/TM}} \tag{3.5}$$

For the f_1 absorber the ground plane distance has been chosen in such a way that it creates a perfect mismatch at the second frequency, f_2, $\Gamma|_{f_2} = -1$. Therefore, the perfect mismatch can

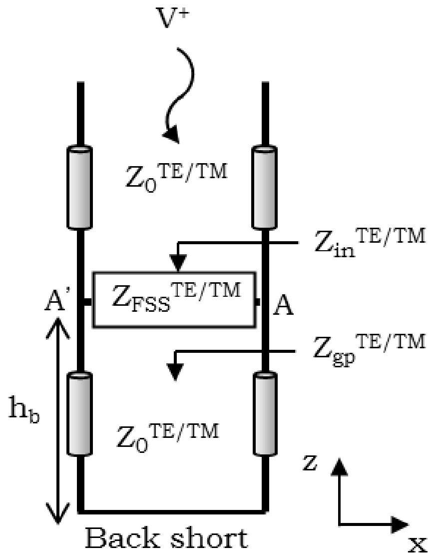

Figure 3.9: Transmission line model for TE and TM fields, with the back short.

be achieved when $Z_{in}|_{f_2}$ = 0. This corresponds to a ground plane distance h_b = $\lambda_2/2$ = $\lambda_1/4$. In addition, h_b = $\lambda_1/4$ leads to $Z_{in}|_{f_1}$ = Z_{FSS} [53]. Therefore, for this choice of h_b, the FSS impedance alone has to be matched to the free space impedance.

In order to match the real part of Z_{FSS} to the free space impedance and achieve the maximum absorption, the following relation has to be satisfied [52]:

$$\frac{w}{d}\eta_0 = R_s \tag{3.6}$$

Where w is the width of the strips (Fig. 3.6), $\eta_0 = 377\Omega$ is the free space impedance and R_s is the sheet resistance of the absorber material. For a certain R_s, w can be chosen in such a way that Z_{FSS} matches the free space impedance. In this project, it was possible to use materials with $3 \leq R_s \leq 10$. If an absorber material with R_s= $5\Omega/square$ is considered, by using Eq. (3.6), the width can be calculated as $w = 0.003\lambda_1$. This value ensures the match between the real part of the FSS impedance and the free space impedance at broadside for both TE and TM modes.

The next step will be tuning the resonance of the structure to have: $Im\{Z_{in}\}|_{f_1} = 0$. As it was mentioned at the beginning of Section 3.3, the resonance of the structure is related to the total length of the cross, $l+2h$. Since l is chosen to be close to the period, the main parameter for tuning the resonance is the length of the short arms, h.

Using CST simulation software, the impedance of the structure, Z_{in}, has been obtained, and the steps above have been followed. In Table 3.1, the optimized geometrical parameters of the structure (see Fig. 3.6) are indicated. The absorption efficiency of such design can be seen in Fig. 3.10. To demonstrated the frequency selectivity in the Jerusalem cross, the performance of the same design without the backing reflector is also illustrated in the figure. As it was mentioned before, the efficiency of an absorber structure without the backing reflector is 50% at best. Moreover, as it was already mentioned in Section 3.1 and [50], the figure indicates that the JC has a resonant nature. The operation bandwidth is defined as the frequency band in which the absorption efficiency is larger than 80%. The rejection bandwidth is defined as the band in which the absorption efficiency is lower than 30%. The relative bandwidth can be expressed in Octave as

$$BW_{relative} = log_2(\frac{f_h}{f_L}) \tag{3.7}$$

Table 3.1: Geometrical and material parameters of the unit cell of a f_1 FSS absorber.

R_s	w	l	h	hb	d
5Ω/sqr	$0.003\lambda_1$	$0.241\lambda_1$	$0.108\lambda_1$	$\lambda_1/4$	$\lambda_1/4$

Where f_H is the high frequency limit of the band, and f_L is the low frequency limit. The relative operation and rejection bandwidth of the f_1 absorber are 1.35 and 0.6 *Octave*, respectively.

The real and imaginary parts of Z_{in} and Z_{FSS} are shown in Fig. 3.11. The figure indicates the effect of the backing reflector on the resonance characteristic of the structure. Z_{FSS} and Z_{in} are equal at f_1 as expected. Therefore, it was possible to match Z_{in} using Eq. (3.6) to the free space impedance. It can be seen that the match of the real part of Z_{in} at f_1 to the free space impedance is approximately achieved: $Re\{Z_{in}\}|_{f_1} = 418\Omega$. The real part of Z_{in} at f_2 is equal to zero as desired. Moreover, the imaginary part of Z_{in} is close to zero at f_1, $Im\{Z_{in}\}|_{f_1} = -11\Omega$, giving the required resonance.

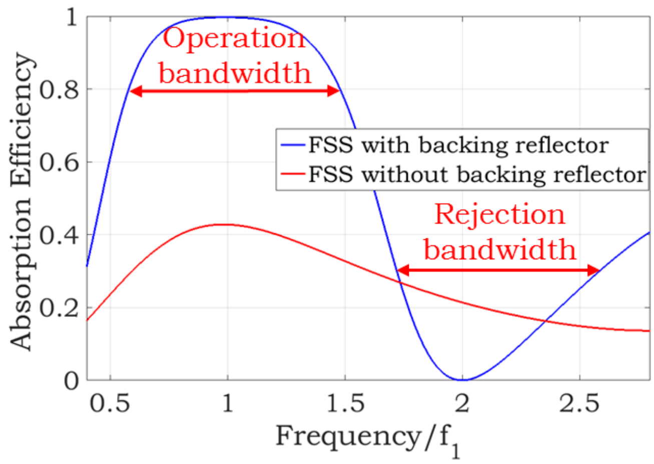

Figure 3.10: Absorption efficiency of the infinite array of f_1 absorbers with indicated operation and rejection bands.

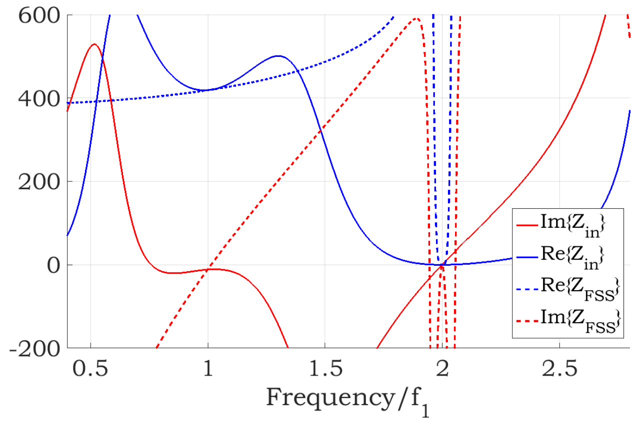

Figure 3.11: Real and imaginary parts of the impedances in the infinite array of f_1 absorbers.

3.3.2 Designing steps for the FSS operating at f_2 Frequency Band

Table 3.2: Geometrical and material parameters of f_2 FSS absorber unit cells

R_s	w	l	h	hb	d
5Ω/sqr	$0.005\lambda_2$	$0.242\lambda_2$	$0.047\lambda_2$	$\lambda_2/6$	$\lambda_2/4$

If the ground plane distance of the second absorber is chosen by scaling the design of the f_1 absorber, the usage of the back short null provides little advantage for the performance of the whole system. In other words, there is no advantage in rejecting the power at frequencies higher than f_2, since the desired rejection band is around f_1 frequency, which is lower than f_2. A solution for achieving a good rejection with the help of the ground plane is to locate it very close to the FSS plane. At low frequencies, this distance is electrically small, which leads to an almost short circuit behavior: $Z_{in}|_{f_1} \simeq 0$. Therefore, from Eq. (3.5) , $\Gamma|_{f_1} \simeq -1$, and most of the field at f_1 band will be reflected. Using this concept, the ground plane distance for the f_2 unit cells have been chosen as: $h_b = \lambda_2/6 = \lambda_1/12$.

The optimization of the remaining parameters follows the same procedure discussed in the previous section. The width of the lines is fixed using Eq. (3.6) for $R_s = 5$. By using the length of the FSS (l and h), the resonance of the structure is adjusted. The optimized geometric parameters of the f_2 FSS are reported in Table 3.2.

In Fig. 3.12, the absorption efficiency of the f_2 absorber is shown for a plane wave incoming from broadside. It is visible that, the structure can have a very large relative operation bandwidth which starts at $1.5f_1$ frequency. Moreover, the f_2 absorber has a rejection bandwidth which finishes at $1.1f_1$ frequency. This bandwidth achieves the required rejection at f_1. The absorption efficiency of the f_2 FSS without the ground plane is also shown in the figure. The back short helps to achieve both the resonance and the matching at f_2 frequency.

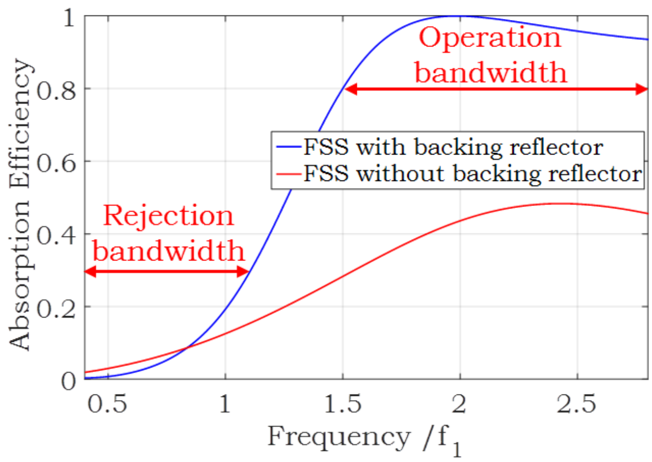

Figure 3.12: Power absorption efficiency of infinite array of f_2 FSS structure.

In Fig. 3.13, the real and imaginary parts of Z_{in} and Z_{FSS} are reported. As it can be seen, the real part of Z_{FSS} is approximately constant. Therefore, the ground plane was used to change the real part of Z_{in} to match it to the free space impedance at f_2 and cause mismatch at f_1. This goal is approximately achieved at the operation frequency: $Re\{Z_{in}\}|_{f_2} = 359\Omega$ and at the rejection frequency: $Re\{Z_{in}\}|_{f_1} = 135\Omega$. $Re\{Z_{in}\}|_{f_1}$ is different from the free space impedance, causing the required mismatch. The imaginary part of the impedance is close to zero at f_2: $Im\{Z_{in}\}|_{f_2} = 13\Omega$, as desired.

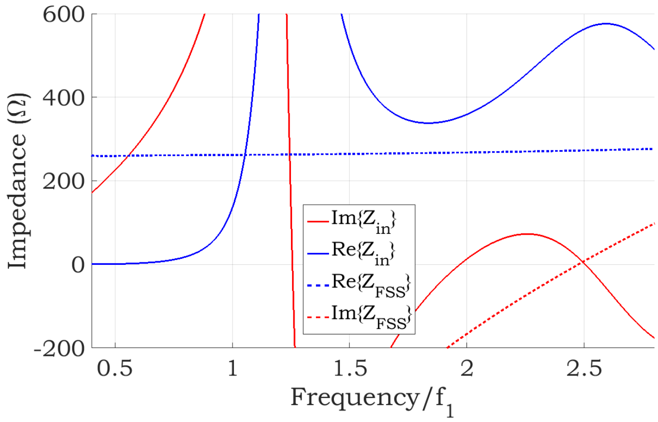

Figure 3.13: Real and imaginary impedance parts of infinite array of f_2 FSS structure.

Broadband Absorbers v.s. Jerusalem Cross based absorbers

Since the rejection band of the discussed design was achieved mainly by using a ground plane, one might wonder if using a Jerusalem cross element is necessary or a simple geometry can provide the same performance. To show the need of the designed structure, the JC is compared in this section to the continuous strip line absorber, Fig. 3.14, discussed in [52]. The continuous straight line absorbers are commonly used as the bolometer based detectors for sub-mm wave imagers [52]. These absorbers have a broadband frequency response. In Fig. 3.15, the absorption efficiency for the designed Jerusalem cross operating at f_1 and f_2 frequencies are compared to the corresponding optimized broadband strip lines with the same period size and R_s. As it can be seen, in the broadband absorber operating at f_1, the absorption efficiency is 80%, lower than the one shown by the JC FSS absorber. This is due to the fact that in this absorber there is no possibility to adjust the imaginary part of Z_{FSS}, unlike the JC FSS, where the length of the short arms can be used to introduce capacitive effects between elements. In f_2 absorbers, since the broadband absorber is not resonant, the ground plane resonance is not enough to create a sharp roll off toward the lower frequency band, and the f_2 JC FSS shows better rejection due to its frequency selectivity. In conclusion, the Jerusalem cross is needed to improve the absorption efficiency in the operational band of f_1 absorbers and also to improve the roll off for the rejection band of the f_2 absorbers. Moreover, a JC structure provides a higher degree of freedom for the design, by having a larger number of geometrical parameters, Fig. 3.6, in comparison to the strip line geometry. The only designable parameters in a continuous strip line are the width of the lines and the period size of the unit cell, Fig. 3.14.

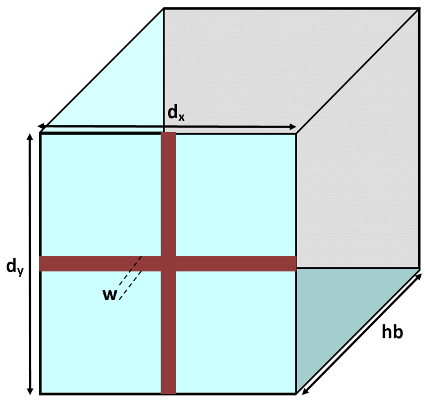

Figure 3.14: Continues strip line absorber and its geometrical parameters.

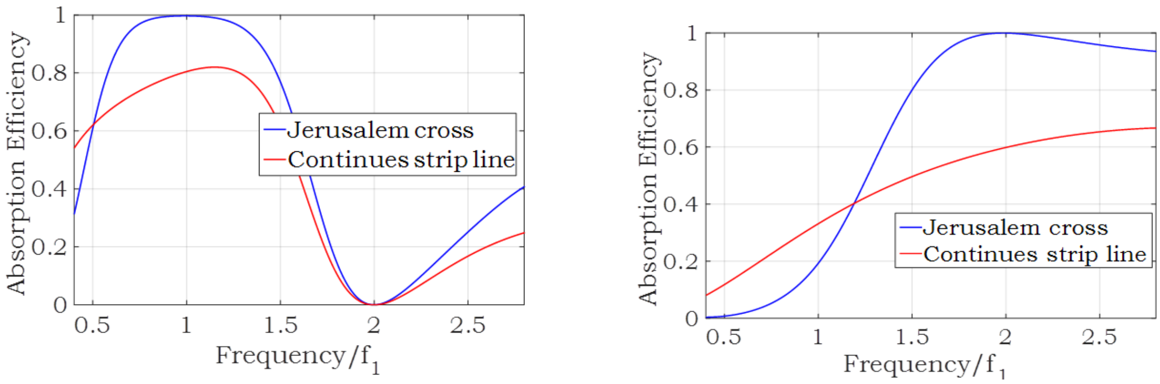

(a) Absorbers operating at f_1 frequency band **(b)** Absorbers operating at f_2 frequency band

Figure 3.15: Comparison between the absorption efficiency of a broadband absorber and a JC FSS based absorber with the same period and sheet resistance.

3.3.3 Oblique Incidence Performance

In this section, the performance of the designed FSS is validated for different scanning angles. It is expected that the matching of the real part of the input impedance degrades while scanning, and the resonance point is shifts in frequency. These effects are due to the fact that both Z_{FSS} and Z_{gp} are functions of the incidence angle. Using Eq. (3.4), the relation between the incidence angle and Z_{gp} can be derived. For the designed f_1 absorber, while scanning in θ, k_{zi} decreases, and $Z_{gp} = \infty$ occurs at a higher frequency. Therefore, the null of the absorption efficiency which occurred at f_2 for broadside incidence, now occurs at $f > f_2$. This effect, decreases the rejection performance of the f_1 absorber. For the f_2 absorber, because of the non-resonance choice of h_b (see the previous section), scanning has little effect on the rejection.

Because of the complex geometry of JC FSS, it is difficult to calculate an analytical expression for Z_{FSS}. Therefore, the effect of scanning on the absorption efficiency has been investigated using CST simulations. In Fig. 3.16, the discussed effects of scanning are shown. The required maximum angle of incidence of the project is 30^o at the edge of the FPA. Up to this limit, the variation of the absorption and rejection bands are minor for both frequencies and for both TE and TM modes. Therefore, it is expected that the FSS based absorbers will behave approximately in the same way regardless of their position in the FPA.

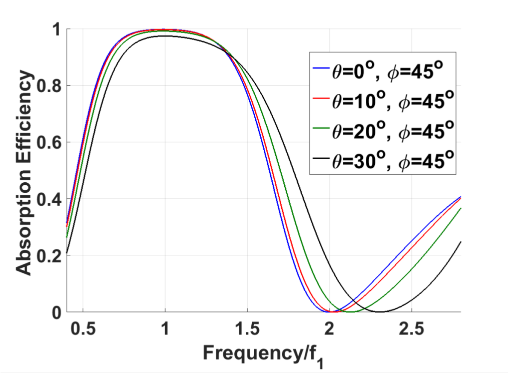

(a) f_1 absorber for TM mode.

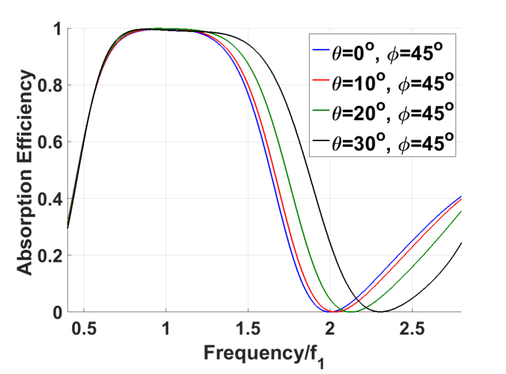

(b) f_1 absorber for TE mode.

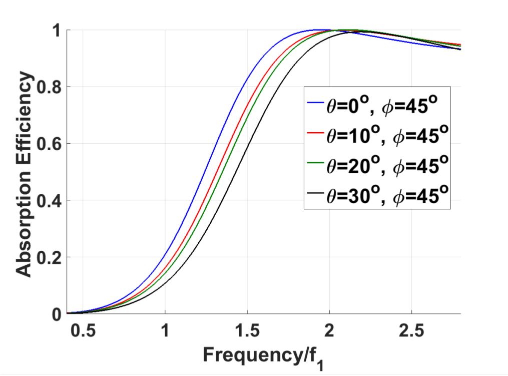

(c) f_2 absorber for TM mode.

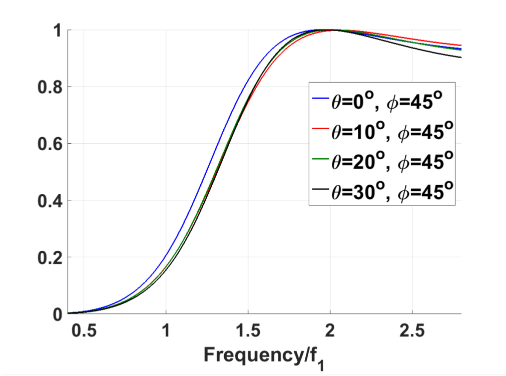

(d) f_2 absorber for TE mode.

Figure 3.16: Absorption efficiency of f_1 and f_2 absorbers in scanning for TE and TM modes separately.

3.3.4 Low Coupling between TE/TM Modes

At the beginning of Section 3.3, the coupled TE and TM transmission line was simplified by two independent TE/TM transmission lines. The following discussion demonstrates the validity of this approximation. To do so, the coupling between the TE and TM modes for the designed absorber based JC FSS is compared to a similar JC FSS made of PEC in Fig. 3.17. In the comparison, the coupling between the modes is shown in terms of S-parameters, S_{TE-TM}. Significant coupling can be observed between the TE and TM modes for certain angles of incidence (Fig. 3.17g and Fig. 3.17h) for the structure made of PEC. On the other hand, when an absorbing material is used, this coupling is low. As it can be observed in Fig. 3.17a to Fig. 3.17d, less than $-20dB$ coupling was achieved. Therefore, the mentioned approximation is valid.

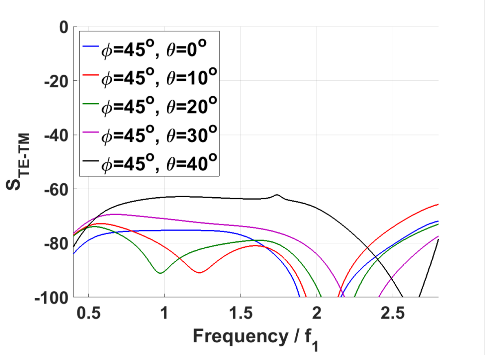

(a) Coupling of modes in f_1 absorber based FSS ($\phi_i = 45^o$).

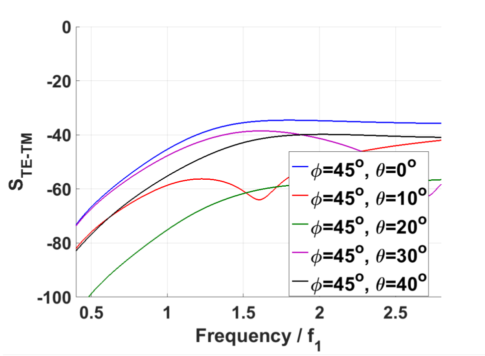

(b) Coupling of modes in f_2 absorber based FSS ($\phi_i = 45^o$).

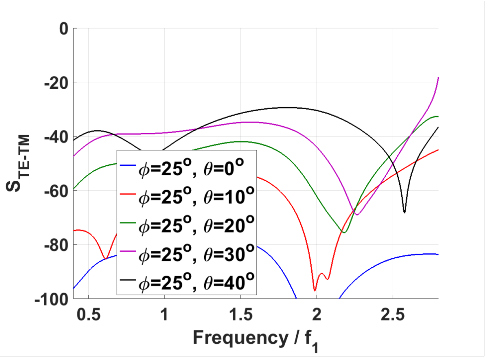

(c) Coupling of modes in f_1 absorber based FSS ($\phi_i = 25^o$).

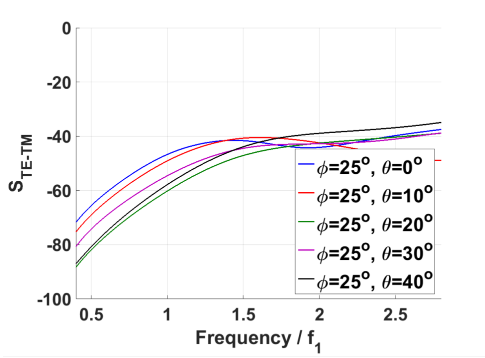

(d) Coupling of modes in f_2 absorber based FSS ($\phi_i = 25^o$).

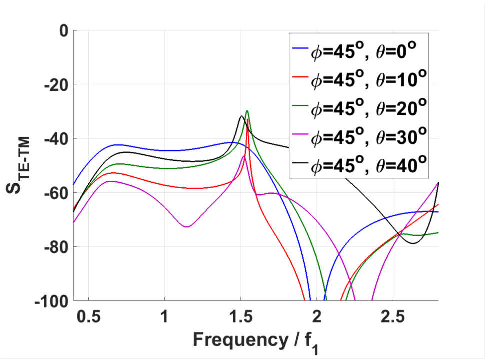

(e) Coupling of modes in f_1 PEC based FSS ($\phi_i = 45^o$).

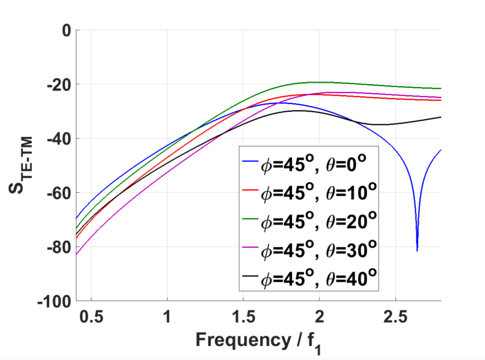

(f) Coupling of modes in f_2 PEC based FSS ($\phi_i = 45^o$).

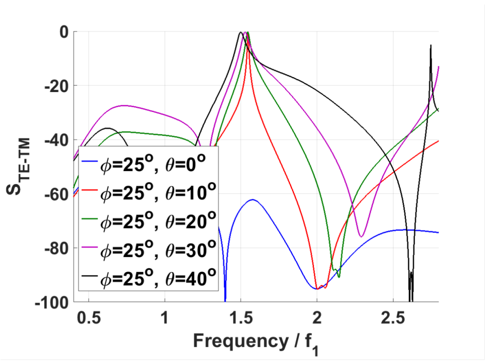

(g) Coupling of modes in f_1 PEC based FSS ($\phi_i = 25^o$).

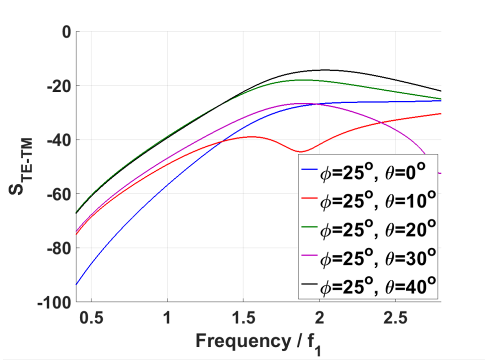

(h) Coupling of modes in f_2 PEC based FSS ($\phi_i = 25^o$).

Figure 3.17: Coupling between TE and TM modes for different scanning angles for both the absorber based FSS and the PEC based.

3.4 Study for Finiteness Effect

The previous sections used the infinite array approximation for the FSS array. However, in reality, the array is finite. In imaging systems based on antennas, finiteness effects can influence the design significantly. On the other hand, since the currents are absorbed and decay over the structure in FSS based absorbers, it is expected that the edge effect is less significant. In this section this effect is investigated.

Absorption Efficiency in the Finite Structure

In general form, using the Poynting theorem [28], one can calculate the amount of incident power generated by a plane wave impinging on a planar structure with amplitude E_0 and propagation vector $\vec{k}_i$ (see Fig. 3.18). The incident power can be expressed as

$$P_{inc} = \frac{1}{2}\frac{|E_0|^2}{\eta_0} A\cos(\theta_i) \tag{3.8}$$

Where η_0 is the impedance of the free space, A is the area of the investigated surface and θ_i is the elevation angle of incidence.

In previous sections, a unit cell boundary condition was applied to calculate the absorption efficiency of an infinite array of FSS based absorber. The absorption efficiency is calculated by assuming that 0.5 watt of power is impinging on the surface of a unit cell for TE or TM mode. Therefore, the incident power is kept constant for different unit cell sizes and angles of incidence. To do so, the amplitude of the incoming plane wave, $|E_0|$, varies in each simulation. In order to investigate a finite array, one must use the open boundary condition in the CST with a plane wave excitation with a certain amplitude and direction of propagation. To compare the performance of the infinite and finite arrays, the same amount of power must impinge on both arrays. This was insured, by simulating the finite array using an amplitude of the incident plane wave expressed as

$$E_0 = \sqrt{\frac{\eta_0}{\cos(\theta_i) A_{abs}}} \tag{3.9}$$

Where A_{abs} is the area of the finite array. Eq. (3.9) was derived using Eq. (3.8) and assuming $P_{inc} = 0.5$ watt.

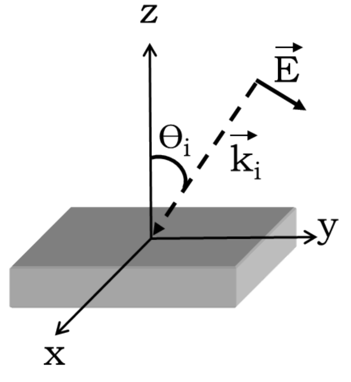

Figure 3.18: A plane wave impinges on a surface with a certain direction of propagation.

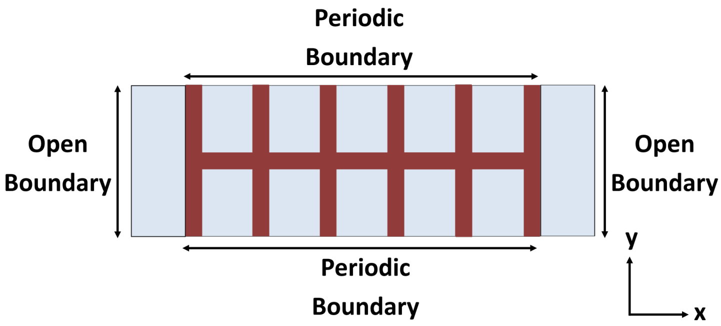

Figure 3.19: 1D array which is finite in x, and it is infinite in y.

Since the finiteness effect is caused by limiting the propagation of induced current on a structure, it is assumed to be similar for the JC array and the broadband absorber. Therefore, the effect is investigated for the continuous strip line with the central frequency of f_1 because of the lower computational time cost. Furthermore, the 2D finite array is approximated by a 1D finite array which is illustrated in Fig. 3.19. This structure is excited by a plane wave. The plane wave is polarized either vertically or horizontally. In a 1D finite array, the number of elements in one dimension is limited. This number is introduced here, as n for the x dimension. In the other dimension, there is an infinite number of elements. In this 1D array, a certain absorber area is considered, which is defined as: $A_{abs} = nd_x \times d_y$.

In the infinite array, CST reports the absorption efficiency as η_{inf}. In order to calculated the absorbed power over a specific area, the expression below is used

$$P_{abs,inf} = \eta_{inf} P_{inc} \tag{3.10}$$

Where $P_{inc} = \frac{1}{2}\frac{|E_0|^2}{\eta_0} A_{abs}\cos(\theta_i)$ and equals 0.5 watt.

In Fig. 3.20, for different values of n, the absorbed power over the introduced 1D finite array is computed, when the incident plane wave is vertically polarized and coming from the broadside. The amplitude of the incident plane wave for the finite case is chosen using Eq. (3.9). The absorbed power for the 1D finite array is compared to the one in the infinite case with the same area. It is visible that, in the 1D finite array, there is a shift of the resonant frequency for $n = 4$. As it is expected, by increasing the number of elements, n, the array behavior approaches the infinite one.

The absorbed power for the horizontally polarized plane wave with different incidence angles are shown in Fig. 3.21. The amount of power absorbed over the finite array is larger than the power absorbed by the infinite array for any incidence angle. This indicates that the finite array has an effective absorbing area, A_{eff}, larger than its physical size.

Effective Area Case Study for a Matched Continues Strip Line

In order to investigate the finiteness effect in the introduced 1D finite array with horizontal polarization, one can define the effective area at a certain frequency as the following: the effective area is an area of an infinite array which absorbs the same amount of power as a finite array with a certain physical area.This definition is shown as

$$P_{abs,fin} = P_{abs,inf} = \eta_{inf} P_{inc,eff} \tag{3.11}$$

Where $P_{inc,eff}$ is

$$P_{inc,eff} = \frac{1}{2\eta_0}|E_0|^2 A_{eff} \tag{3.12}$$

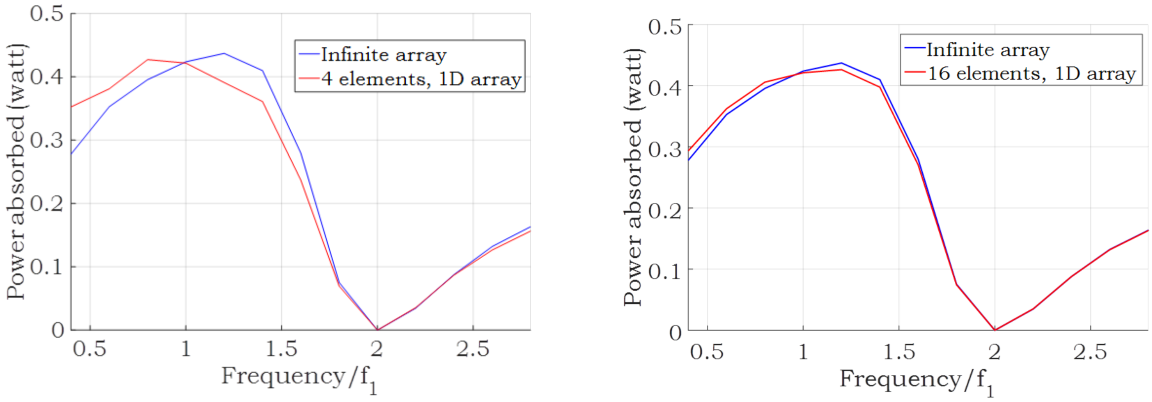

(a) With 4 elements in x direction ($n = 4$). **(b)** With 16 elements in x direction ($n = 16$).

Figure 3.20: Comparison between the absorbed power by the infinite array and a 1D array, finite in x and excited by a vertically polarized plane wave coming from the broadside, for continuous dual polarized strip line array.

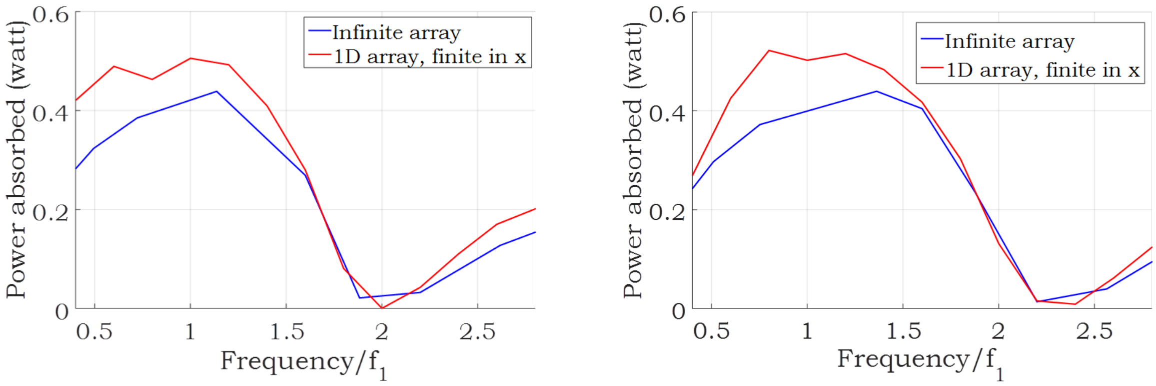

(a) Plane wave is coming from broadside. **(b)** Plane wave is coming from $\theta_i = 30^o$ and $\phi_i = 0^o$.

Figure 3.21: Comparison between the absorbed power by the infinite array and a 1D array, with $n = 4$ and excited by a horizontally polarized plane wave for continuous dual polarized strip line array.

Therefore, using Eq. (3.9), when $\theta_i = 0$ (at broadside incidence), the expression for the effective area is

$$A_{eff} = \frac{P_{abs,fin}}{0.5\eta_{inf}} A_{abs} \tag{3.13}$$

The ratio A_{eff}/A_{abs} is a good indication of the finiteness effect. If A_{eff}/A_{abs} is approximately 1, the finite and infinite arrays are approximately the same in terms of power absorption over the area A_{abs}.

In the following section, a case study is represented to understand how significant is the introduced effect. A single polarized infinite continuous strip line absorber is designed to have high absorption at f_1 frequency. The performance of the infinite structure is then compared to a finite absorber configuration. This case study is provided at three frequency points: $f = 0.8f_1$, f_1 and $1.2f_1$. The actual length in x, L, of the finite line is varied from $0.42\lambda_1$ to $2.5\lambda_1$. In Fig. 3.22, the normalized effective length of the straight line is shown as a function of the actual length. When the array size enlarges the edge effect is less significant and the effective length converges toward the physical length of the line. For small lengths, the oscillation in the ratio is due to variations of the phase of the currents at the edges of the absorber. The oscillation is more visible for the small lengths, because the amplitude of the current is still high at the edges.

The same effect can be seen for a 1D array of f_1 JC FSS with $n = 5$, Fig. 3.23, which

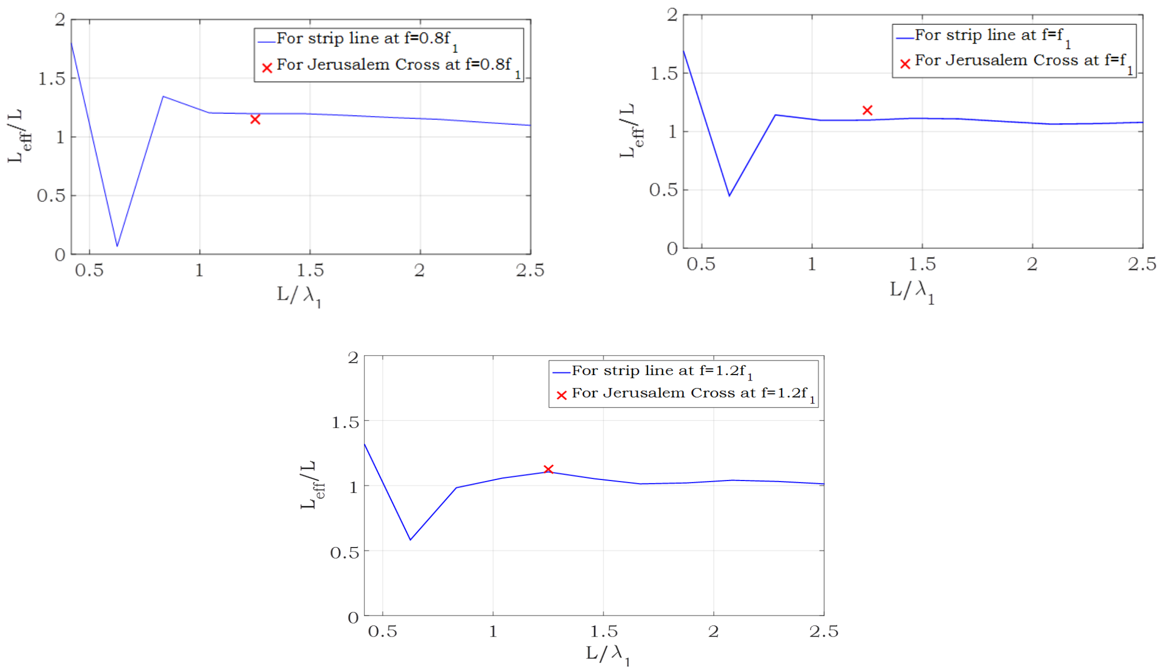

Figure 3.22: Effective length as a function of the physical length at different frequencies.

is excited by a horizontally polarized plane wave. This effect is illustrated in Fig. 3.24. To evaluate the edge effect contributions, the effective area can be introduced as defined before. The effective length of the f_1 Jerusalem cross finite array is indicated in Fig. 3.22 by red crosses. Using the results of this case study, one can assumed that if the length of the detector is larger than λ, the finiteness effect is negligible. Since, as it was mentioned in Section 1.4, both set of absorbers have a larger side length than the wavelength at their central frequencies ($w_{f1} = 1.25\lambda_1$ and $w_{f2} = 1.5\lambda_2$), in the final evaluation of the system performance, the finiteness effect has been neglected.

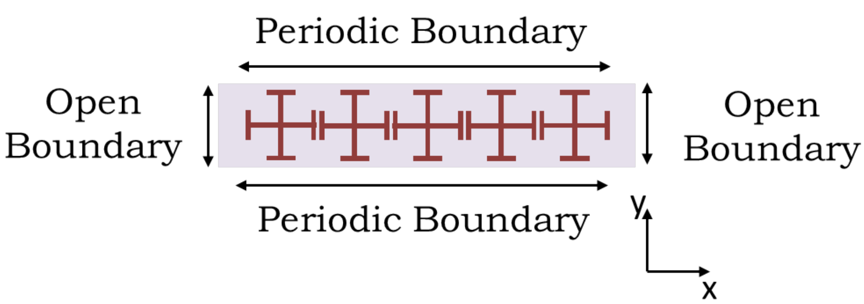

Figure 3.23: 1D array of Jerusalem cross which is finite in x, and it is infinite in y.

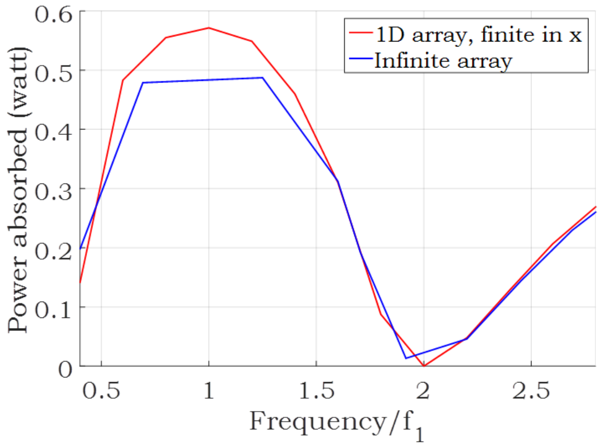

Figure 3.24: Power absorbed over a 1D finite array of JC FSS v.s. the power absorbed over the same physical area in an infinite array of JC FSS.

3.5 Evaluating the Performance of the Design Including the KID Resonators

As it was mentioned in Section 3.1, the FSS absorbers are used to couple the corresponding frequency bands into the KID resonator lines. If the same free standing design of the FSS is used when the dielectric layer and resonator lines are present (see Fig. 3.4), the absorption efficiency of each absorber set changes as shown in Fig. 3.25. Since the resonator lines distort the symmetry of the structure, the results in this section are reported for the horizontal and vertical excitations separately. As it can be seen in the figure, the dielectric layer and the resonator lines change the frequency response of the FSS drastically. Therefore, the initial free standing design can not be used as the final design. The distortion in the absorption efficiency is related to changes in the input impedance of the structure. The sheet resistance of the material used as the superconducting resonator was reported in Fig. 3.5. This sheet resistance has both real and imaginary parts and it is a function of frequency. Therefore, the combined impedance of the FSS, dielectric layer and the resonator lines is a complicated term. This impedance is reported in Fig. 3.26 for both free standing case and the distorted case. In the f_1 absorbers, when the layer and the resonator lines are present, the resonance is shifted and the matching at f_1 frequency is lost, especially for the horizontal polarization. The same issues can be observed for f_2 absorbers. In addition, the new f_1 absorbers also reject less power in their rejection band.

In this section, the FSS designs at both frequencies are adjusted to keep into account the effect of the dielectric layer and the superconducting lines. In order to reach this goal, firstly, the effect of having the layer underneath is studied using simulations in CST. Secondly, the FSS designs are reoptimized based on the first step. Finally, the KID lines are added in such a way to minimized their effect on the frequency response of the FSS and a final design is presented.

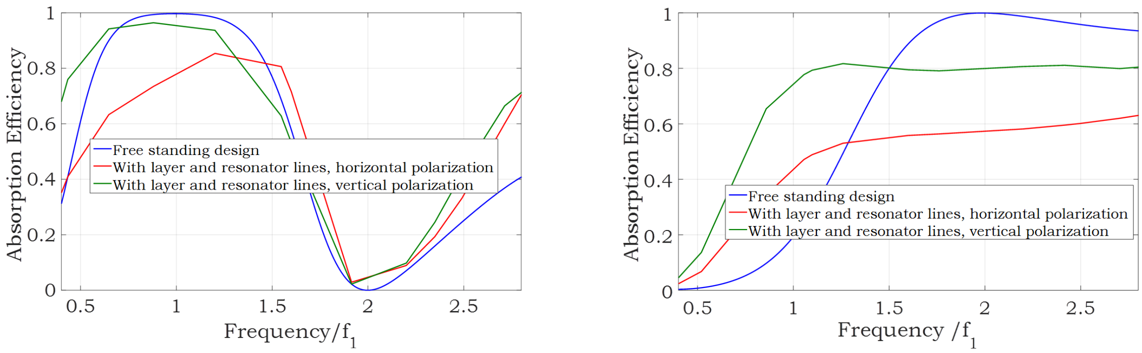

(a) For f_1 absorbers. **(b)** For f_2 absorbers.

Figure 3.25: Absorption efficiency of the free standing FSS design v.s. the same design including the dielectric layer and the resonator lines.

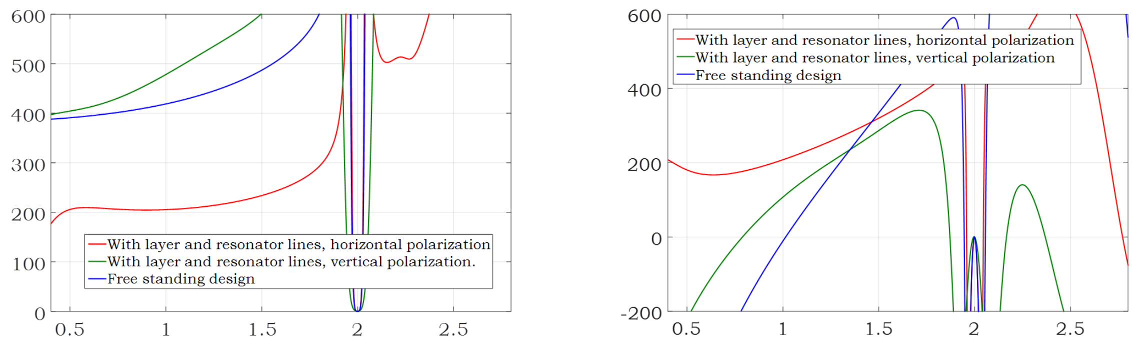

(a) Real part of the impedance for f_1 absorbers. **(b)** Imaginary part of the impedance for f_1 absorbers.

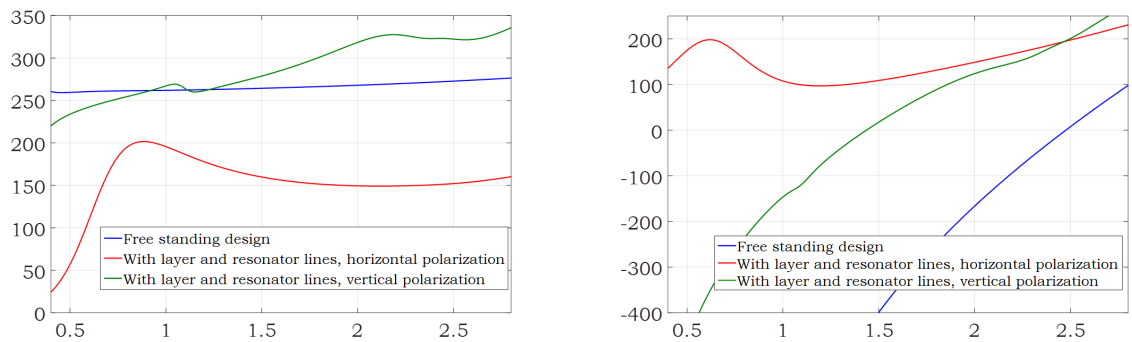

(c) Real part of the impedance for f_2 absorbers. **(d)** Imaginary part of the impedance for f_2 absorbers.

Figure 3.26: Input impedance of the FSS design (Z_{FSS}) for free standing v.s. with layer and resonator lines.

Effect of Thin Dielectric Layer on the FSS Response

By adding a dielectric layer, the equivalent wavelength of the structure is lowered, and the structure resonates at a slightly lower frequency. To compensate this effect, the geometrical parameters of the FSS unit cells must be retuned. The absorption efficiency of the structure designed in Section 3.3.1 and the one including the dielectric layer are illustrated in Fig. 3.27 (black and red curves). The absorption efficiency of the design including the dielectric slab does not reach 100% at the central frequency. This is due to the fact that the needed width to achieve the matching to the free space impedance (w in Eq. (3.6)) is too small for the fabrication procedure used in CONSORTIS. Therefore, the minimum realizable width was used in the design. However, this problem will be solved later when the resonator lines are also included.

The rejection issue observed in Fig. 3.25a is not solved with this new optimization. This issue is due to the resonance of the short arm of the opposite polarization, as discussed in Section 3.3. A possible solution is to further bent the JC FSS, Fig. 3.28, which leads to a smaller length for the short arm. In Fig. 3.27, also the absorption efficiency of the bent JC is illustrated. It is visible from the figure, that the rejection is improved by using the bent geometry. For the f_2 absorber, since the rejection band is at lower frequencies, the discussed issue is not present. However, the geometrical parameters of the FSS still should be retuned. The retuning of the f_2 absorbers is performed in the following section, when the effect of the resonator lines is also present.

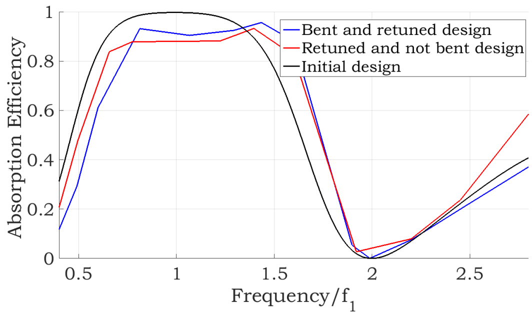

Figure 3.27: An example of comparison between the absorption efficiency of a bent and not bent JC.

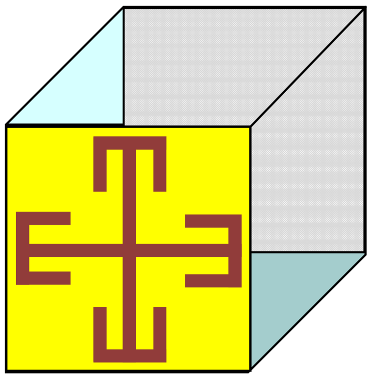

Figure 3.28: Bent JC for the f_1 design.

Effect of Resonator Lines on the FSS Response

In order to minimize the effect of the resonator lines, their position (r_p in Fig. 3.29) is chosen as far as possible from the horizontal main arms. For both absorber types, the design steps described in Section 3.3 are performed again to match the new impedance to the free space one and to adjust the resonance. The new designed parameters of the JC are introduced in Fig. 3.29. The optimized value for these parameters are reported in Table 3.3 and Table 3.4 for f_1 and f_2 absorbers, respectively. The absorption efficiency of the new designs for both the horizontal and vertical polarization are shown in Fig. 3.30.

Table 3.3: Geometrical and material parameters of f_1 FSS absorber unit cells with KID lines.

R_s	w	l	$h1$	$h2$	hb	d	rw	rd	rp
5Ω/sqr	$0.005\lambda_1$	$0.238\lambda_1$	$0.042\lambda_1$	$0.033\lambda_1$	$\lambda_1/4$	$\lambda_1/4$	$0.033\lambda_1$	$0.004\lambda_1$	$0.071\lambda_1$

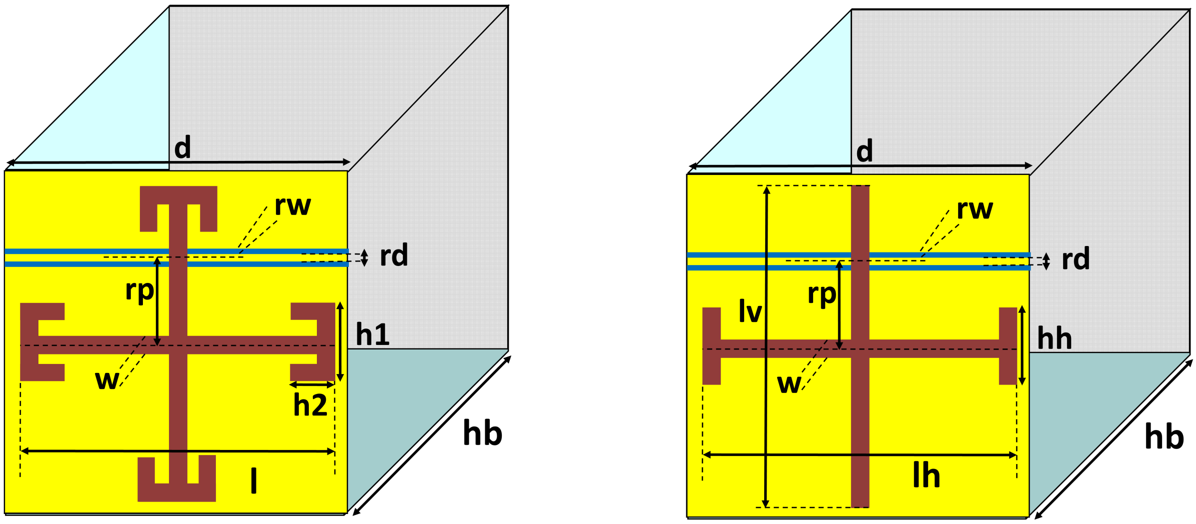

(a) f_1 FSS unit cell. **(b)** f_2 FSS unit cell.

Figure 3.29: Design parameters of the absorbers with resonator lines.

Table 3.4: Geometrical and material parameters of f_2 FSS absorber unit cells with KID lines.

R_s	w	lh	lv	hh	hb	d	rw	rd	rp
5Ω/sqr	$0.008\lambda_2$	$0.237\lambda_2$	$0.243\lambda_2$	$0.043\lambda_2$	$\lambda_2/6$	$\lambda_2/4$	$0.007\lambda_2$	$0.008\lambda_2$	$0.063\lambda_2$

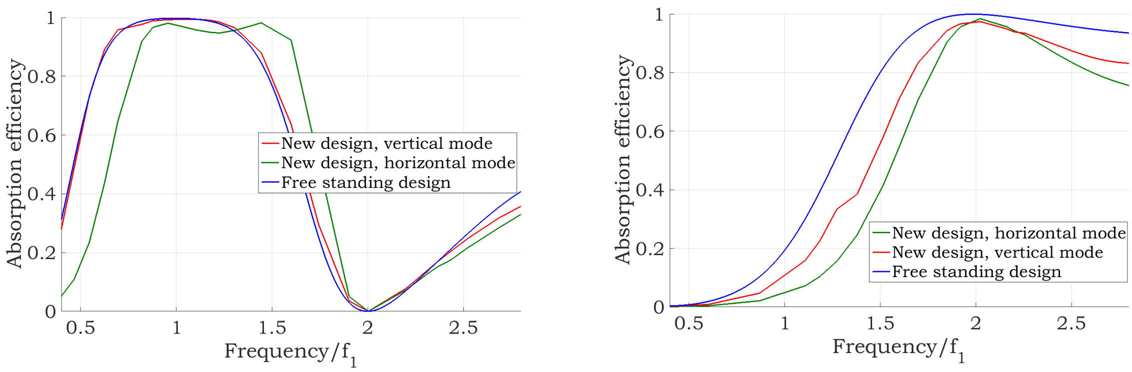

(a) f_1 absorber. **(b)** f_2 absorber.

Figure 3.30: Absorption efficiency for both the horizontal and vertical excitations.

The FSS geometry of the f_2 absorber needed no further bending. However, the reoptimization of its design leads to a very small vertical short arm. This arm was removed and to compensate, the length of the vertical main arm was increased.

The main horizontal arm and the short vertical arms in the FSS unit cells are affected electrically by the presence of the horizontal resonator lines. Therefore, the resonator lines distort the symmetry of the design both electrically and geometrically, which leads to different absorption efficiencies for the horizontal and vertical polarizations. In the f_1 FSS for the horizontal polarization, the absorption response is shifted toward the higher frequencies. As for the f_2 FSS, the rejection is actually improved in comparison to the free standing design, but the absorption bandwidth narrowed. Since the total performance of the imager is related to the average absorbed power over both the rejection and absorption bandwidths, these effects are tolerable. Using the definition of the operation and rejection bands (see Section 3.3.1.), the relative bandwidth of these bands for both the f_1 and f_2 absorbers are reported in Table 3.5 and Table 3.6, respectively.

Table 3.5: Comparison between the operation and rejection bandwidths of the free standing design and the new introduced design for f_1 absorbers.

	Horizontal operation BW	Vertical operation BW	Horizontal rejection BW	Vertical rejection BW
New design	1.1 Octave	1.36 Octave	0.59 Octave	0.6 Octave
Free standing design	1.35 Octave	1.35 Octave	0.6 Octave	0.6 Octave

Table 3.6: Comparison between the operation and rejection bandwidths of the free standing design and the new introduced design for f_2 absorbers.

	Horizontal operation BW	Vertical operation BW	Horizontal rejection BW	Vertical rejection BW
New design	0.56 Octave	starts at $1.67f_1$	ends at $1.42f_1$	ends at $1.24f_1$
Free standing design	starts at $1.5f_1$	starts at $1.5f_1$	ends at $1.1f_1$	ends at $1.1f_1$

3.6 Conclusion

In this chapter, the absorber based FSS was introduced. Moreover, the latter for both required bands of the CONSORTIS project were designed by following few steps. These design steps matched the equivalent impedance of the absorber based FSS to the free space impedance. The performance of the design was also evaluated for oblique incidences. In addition, the effect of two more realistic cases were investigated: the edge effect cased by the finiteness of the array, and the effect of having KID resonators behind the FSS.

In the study for the finite array, in order to investigate the finiteness effect, the concept of the effective area was introduced. The effective area is defined as an area on an infinite array which absorbs the same amount of power as a finite array with a certain physical size. In order to understand the significance of the proposed concept for this project, a case study was provided for the effective length for different absorber sizes at several frequencies. The case study demonstrated that the edge effect in the absorber based FSS is negligible when the array size is larger than a wavelength at the investigated frequency.

The KID resonator lines distort the FSS absorption response. After understanding their effect on the structure, to compensate it for each FSS types a modified design was proposed. The parameters in the new designs were optimized and reported.

Chapter 4

Analysis and Performance Evaluation of the Absorber Coupled Optics

In this chapter, the performance of the imager including both the focusing system and the absorbers is evaluated. To do so, the behavior of the detector is analyzed using a proposed circuit model for a generic incoming plane wave. In Section 2.2.1, the spectral domain representation of the fields at the focal plane of a focusing system was reported. By combining the two representations, one can evaluate the field on the focal plane of the imaging system, including the effect of the detectors and the overall absorption efficiency. The key to reach this goal is the plane wave spectrum representation of the field at the focal plane. A plane wave spectrum (PWS) in the spectral domain is an infinite summation of the uniform plane waves coming from every direction [54]. As a direct result of such representation, the absorption efficiency of the imager including the detectors coupled to the optics can be computed. An approximated method is also introduced by assuming simplifications on the full model.

Each detector in the FPA will receive an amount of power that varies as a function of the observed direction in the FoV. If the normalized absorbed power on the detector is plotted as the function of the angle in the FoV from which it is generated, this figure can be referred to as the angular response of the imager to a point source. A detailed analysis of this response is provided in this chapter. By definition, the resolution of the imager can be obtained directly from the angular response as its half power beam width (HPBW). The resolution of the imager depends on the detector size. In particular, it is shown that by increasing the detector size the effective resolution enlarges. In the final section of this chapter, the introduced methods are used to evaluate the performance of the imager in CONSORTIS project in terms of its angular response to a point source and resolution, considering the actual optical system developed for the project.

The described analysis is shown for the free standing FSS design introduced in chapter 3. The design including the superconducting resonator lines and the dielectric layer is not used to evaluate the performance of the absorber based FSS coupled to the optics. Moreover, the input impedance of the FSS design is obtained using CST by assuming an infinite array approximation. By considering the discussion provided in Section 3.4 and 3.5, these assumptions are approximately valid.

4.1 Circuit Model for the Absorber Based FSS Array

This section focuses on deriving a circuit model that allows the evaluation of the absorbed power on the FSS based absorber for a generic plane wave incidence. This circuit model will be used in the following sections to couple the absorber to the optics. The analysis tool for periodic structures discussed in Section 2.1 can be used if the FSS array is approximated as an infinite periodic structure. If a plane wave with a certain direction of propagation (θ_i and ϕ_i) impinges on the array, Fig. 4.1, the main Floquet mode wave vector is equal to the propagation vector of the incoming plane wave, $k_{x0} = k_x$ and $k_{y0} = k_y$. This generic plane wave is referred to as the direct field, and does not include the effect of the stratification or FSS. The direct field can be

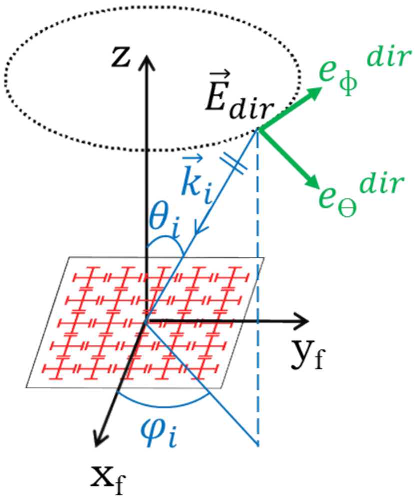

Figure 4.1: The direct field impinging on the FSS array.

expressed as

$$\vec{E}_{dir} = (e_\theta^{dir}\hat{\theta} + e_\phi^{dir}\hat{\phi})e^{-j\vec{k}_i.\vec{r}} \tag{4.1}$$

Where e_θ^{dir} and e_ϕ^{dir} are the amplitudes of the spherical components of the plane wave and $\vec{k}_i = k_x\hat{x} + k_y\hat{y} + k_z\hat{z}$ is its propagation vector, $|\vec{k}_i| = k = 2\pi/\lambda$, Fig. 4.1. The Cartesian components of the propagation vector are expressed as

$$k_x = k\sin(\theta_i)\cos(\phi_i) \tag{4.2}$$

$$k_y = k\sin(\theta_i)\cos(\phi_i) \tag{4.3}$$

$$k_z = k\cos(\theta_i) \tag{4.4}$$

Where θ_i is the elevation angle of incidence and ϕ_i is the azimuth angle, Fig. 4.1.

Using the discussions in Section 3.3, for a plane wave with a certain direction of incidence (k_x and k_y), the behavior of an infinite array of the FSS elements can be represented as an impedance matrix in an equivalent transmission line circuit. Each element of the matrix relates a TE or TM equivalent voltage on the FSS to an equivalent TE or TM current on the FSS plane. These voltages and currents represent the transverse values of the electric and magnetic fields, respectively. The transverse voltages and currents are averaged over the FSS unit cell area, and the transversalization is done with respect to the normal vector of the surface of the structure (which is assumed to be $\hat{z}$, see Fig. 4.1). In [52, 55–57] for strip based absorbers, the Floquet mode impedance matrix is modeled with an analytical equivalent circuit that allows to calculate the real current induced on the line. To do so, the actual impedance of the lines per unit of length is investigated. In [52], the coupling between the TE and TM modes is not negligible. Therefore, the introduced analytical model takes the coupling into account by introducing a transformer, Fig. 4.2b, that combines the fields into actual currents flowing on the strips. However, for more complicated geometries, the derivation of an analytical circuit model is not trivial. In such cases, a periodic based numerical method can be used to compute an impedance matrix that represents the average Floquet field propagating on the FSS surface.

In this work, this impedance matrix is obtained using the CST software. As it was discussed in Section 3.3, the TE and TM modes are decoupled in the designed absorber based on Jerusalem cross elements. Therefore, it is possible to represent the modes with independent circuits, and simplify the impedance matrix to an impedance for each TE and TM mode only, Fig. 4.2c.

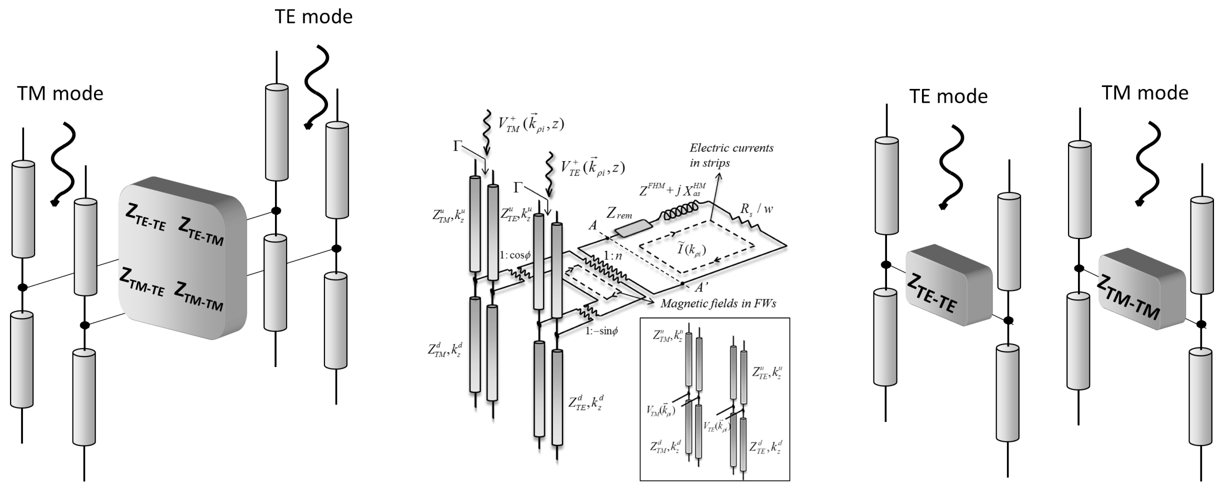

(a) Transmission line circuit model in generic form.

(b) Circuit model considering the coupling [52].

(c) Circuit model without considering any coupling.

Figure 4.2: Equivalent circuit model of the absorber based FSS.

Fig. 4.3 illustrates the discussed equivalent transmission line model for a direct field with a certain direction of propagation, k_x and k_y. In the figure, h_b is the distance of the ground plane from the FSS plane and $Z_0^{TM/TE}(k_x, k_y)$ is the characteristic impedance of the transmission line for each mode, k_x and k_y (the characteristic impedance of a transmission line is discussed in Section 2.1). $Z_{FSS}^{TE/TM}$ represents the uncoupled elements in the mentioned impedance matrix, i.e. Z_{TE-TE} and Z_{TM-TM} in Fig. 4.2c.

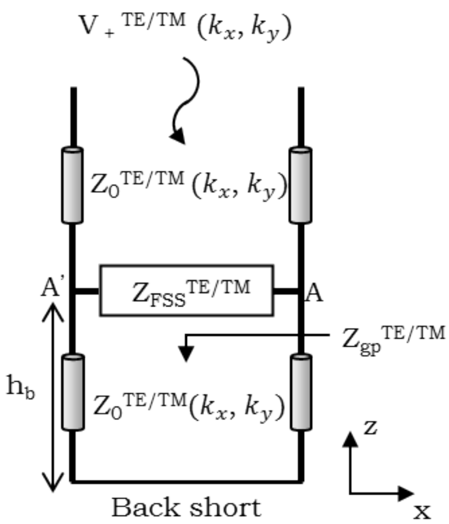

Figure 4.3: Transmission line representation of the absorber based FSS.

TE/TM Decoupled Model

The transverse voltage source in the transmission line model is $\upsilon_{+}^{TE/TM}$. This source can be expressed as the transverse value of the direct field incoming toward the structure, Eq. (4.1). Transverse TE and TM voltage sources in transmission line representation are defined as

$$\upsilon_{+}^{TM} = \int_{-d_y/2}^{d_y/2}\int_{-d_x/2}^{d_x/2} \vec{e}_{dir}\cdot\vec{e}_{TM} d_x d_y \tag{4.5}$$

$$\upsilon_{+}^{TE} = \int_{-d_y/2}^{d_y/2}\int_{-d_x/2}^{d_x/2} \vec{e}_{dir}\cdot\vec{e}_{TE} d_x d_y \tag{4.6}$$

Where d_x and d_y are the periods of the unit cell in x and y direction, respectively. $\vec{e_{TM}}$ and $\vec{e_{TE}}$ are the TM and TE basis functions, which are defined as [52]

$$\vec{e}_{TM} = \frac{1}{\sqrt{d_x d_y}}(\cos(\phi)\,\hat{x} + \sin(\phi)\,\hat{y})e^{j\vec{k}_{pi}\cdot\vec{\rho}} \tag{4.7}$$

$$\vec{e}_{TE} = \frac{1}{\sqrt{d_x d_y}}(-\sin(\phi)\,\hat{x} + \cos(\phi)\,\hat{y})e^{j\vec{k}_{p}\cdot\vec{\rho}} \tag{4.8}$$

As shown in Fig. 4.1, θ_i and ϕ_i are the incidence angles of the incoming direct field. Using Eq. (4.1) and Eq. (4.5) to Eq. (4.8), υ_{TM}^{+} and υ_{TE}^{+} for a specific incoming plane wave can be expressed as

$$\upsilon_{+}^{TM}(k_x,k_y) = \sqrt{d_x d_y}e_{\theta}^{dir}\cos(\theta_i) \tag{4.9}$$

$$\upsilon_{+}^{TE}(k_x,k_y) = \sqrt{d_x d_y}e_{\phi}^{dir} \tag{4.10}$$

The term $\sqrt{d_x d_y}$ is used to normalize the voltage values over a unit cell area.

The equivalent transmission line can be represented by an equivalent Thevenin circuit from the AA' terminal, Fig. 4.4. In this representation, from the definition of a Thevenin source, $V_{oc}^{TE/TM}$ can be calculated as the voltage at the AA' terminal when $Z_{FSS}^{TE/TM}$ is replaced with an open circuit. Therefore this source is expressed as

$$V_{oc}^{TE/TM}(k_x,k_y) = \upsilon_{+}^{TE/TM}(k_x,k_y)(1+\Gamma_{oc}^{TE/TM}(k_x,k_y)) \tag{4.11}$$

Where $\Gamma_{oc}^{TE/TM}$ is the reflection coefficient between $Z_0^{TE/TM}$ and $Z_{gp}^{TE/TM}$

$$\Gamma_{oc}^{TE/TM}(k_x,k_y) = \frac{Z_{gp}^{TE/TM}(k_x,k_y) - Z_0^{TE/TM}(k_x,k_y)}{Z_{gp}^{TE/TM}(k_x,k_y) + Z_0^{TE/TM}(k_x,k_y)} \tag{4.12}$$

Where $Z_{gp}^{TE/TM}(k_x,k_y)$ is the impedance seen from the AA' terminal toward the ground plane, Fig. 4.3, and $Z_0^{TE/TM}(k_x,k_y)$ is the characteristic impedance of the transmission line. This impedance were already discussed in Section 3.3.1. The equivalent Thevenin impedance is $Z_{oc}^{TE/TM}$, and it is defined as the equivalent impedance seen by the AA' terminal. Therefore, $Z_{oc}^{TE/TM}$ can be expressed as

$$Z_{oc}^{TE/TM}(k_x,k_y) = Z_{gp}^{TE/TM}(k_x,k_y)\|Z_0^{TE/TM}(k_x,k_y) \tag{4.13}$$

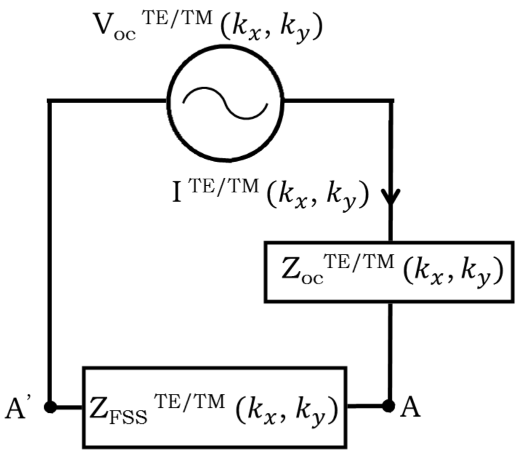

Figure 4.4: Thevenin equivalent circuit from AA' terminal in the transmission line model.

Since all the elements in Fig. 4.4 are defined above, one can calculate the average current flowing on the FSS for each mode as

$$I^{TE/TM}(k_x,k_y) = \frac{V_{oc}^{TE/TM}(k_x,k_y)}{Z_{FSS}^{TE/TM}(k_x,k_y) + Z_{oc}^{TE/TM}(k_x,k_y)} \tag{4.14}$$

The absorbed power on the FSS can be expressed as

$$P_{abs}^{TE/TM}(k_x,k_y) = \frac{1}{2}|I^{TE/TM}(k_x,k_y)|^2 Real(Z_{FSS}^{TE/TM}(k_x,k_y)) \tag{4.15}$$

Using the Poynting theorem, the incident power impinging on a unit cell area is expressed as

$$P_{inc}(k_x,k_y) = \frac{1}{2\eta_0}|\vec{E}_{dir}|^2 d_x d_y \cos(\theta_i) \tag{4.16}$$

To validate the steps above, the discussed design of the JC FSS is simulated in CST for TE and TM modes separately, using the unit cell boundary condition. The impedance matrix of the FSS is calculated using the software. In the unit cell boundary condition, CST calculates the absorption efficiency of the structure for each TE and TM modes separately. In order to compare the circuit model with the results of CST, the same normalization for calculating the efficiency is required. The incident power of TE and TM modes can be expressed as

$$P_{inc}^{TE/TM}(k_x,k_y) = \frac{1}{2}\frac{|\upsilon_+^{TE/TM}(k_x,k_y)|^2}{Z_0^{TE/TM}(k_x,k_y)} \tag{4.17}$$

Since in CST the incident power is 0.5 watt, the voltages, $\upsilon_+^{TE/TM}(k_x,k_y)$, can be calculated from Eq. (4.17). The absorption efficiency for each mode can be introduced as

$$\eta_{abs}^{TE/TM}(k_x,k_y) = \frac{P_{abs}^{TE/TM}(k_x,k_y)}{P_{inc}^{TE/TM}(k_x,k_y)} \tag{4.18}$$

A MATLAB tool including all the described steps (Eq. (4.9) to Eq. (4.18)) which uses the described FSS impedance matrix was developed. Fig. 4.5 illustrates a case for a certain angle of incidence as an examples to compare the efficiency calculated using Eq. (4.18) and the efficiency reported directly by CST. It is visible that the results computed using the MATLAB tool and CST simulation agree well.

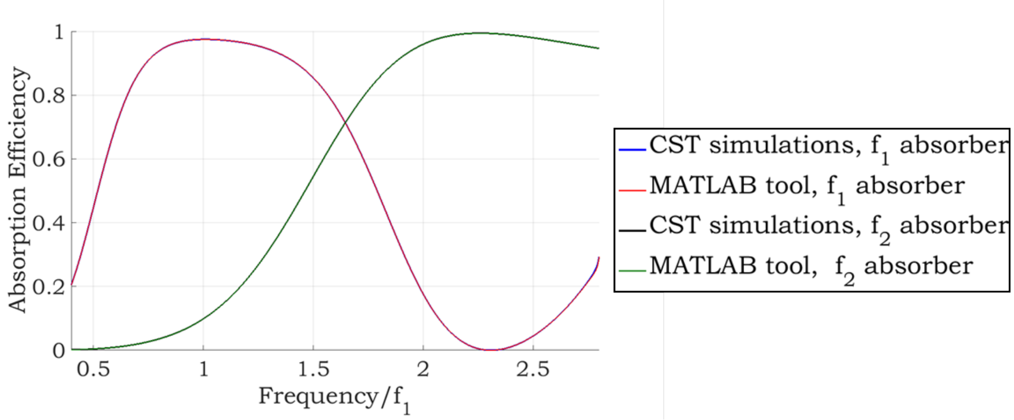

(a) Absorbers excited with only TM mode.

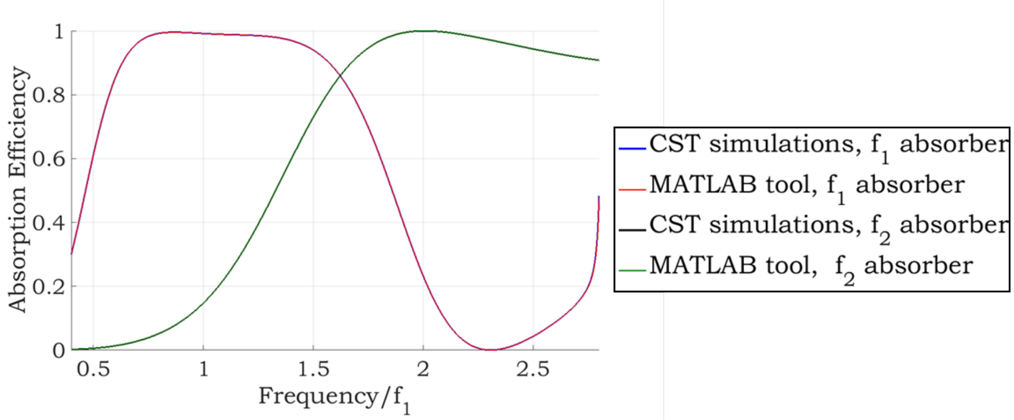

(b) Absorbers excited with only TE mode.

Figure 4.5: Comparing absorption efficiency of MATLAB code and CST simulation for both f_1 and f_2 absorbers with scanning angle of $\theta = 30^o$ and $\phi = 25^o$

Validation of the Circuit Model

The main goal of the introduced circuit model is to evaluate the absorbed power when several coherent plane waves arrive with both TE and TM modes on the FSS. In general, the electric field in a plane wave is the combination of both TE and TM fields, and can be expressed as

$$\vec{E} = E_{TM}\hat{\theta} + E_{TE}\hat{\phi} \tag{4.19}$$

As it was discussed in Section 3.3, the possibility of breaking the coupled circuit (see Fig. 4.2a) to two separate circuits (see Fig. 4.2c) is only applicable for this specific absorbing geometry. By exploiting the low coupling between the modes, one can assume that the amount of power absorbed from an incoming generic plane wave can be calculated as the summation of the absorbed powers associated to the TE and TM modes, as

$$P_{abs}^{PW} \simeq P_{abs}^{TE} + P_{abs}^{TM}. \tag{4.20}$$

In this section, the introduced MATLAB tool is used to validate the possibility of calculating P_{abs}^{PW} using Eq. (4.20) and Eq. (4.15). To achieve this goal, the calculated absorbed power is compared to one simulated by CST. The unit cell simulation can only excite the TE and TM modes separately. Therefore, the plane wave excitation and the periodic boundary condition is the alternative choice to validate the approximation. However, the periodic boundary condition does not support plane wave excitations with oblique incidence angles. Therefore, another method must be introduced to calculated the absorbed power of a generic plane wave using unit cell simulation.

In general, the absorbed power over a certain volume of a material can be calculated as [28]

$$P_{abs} = \frac{1}{2}\iiint_{Volume} \sigma |E|^2 dv \tag{4.21}$$

Where σ is the conductivity of the material. In the case of absorbers, the thickness of the material, τ (see Fig. 4.6a), is chosen very thin in comparison to the skin depth ($\tau << \delta$). Therefore, one can assume that the electric field inside the absorber is constant and equal to the one on its surface. As it was mentioned in Section 3.3, an important parameter of the structure is the sheet resistance of the absorbing material. This parameter is defined as [52]

$$R_s \simeq \frac{1}{\sigma\tau} \tag{4.22}$$

By using the definition of the sheet resistance and assuming that the electrical field is constant in the thickness of the material, the absorbed power can be calculated as a surface integral expressed as

$$P_{abs} = \frac{1}{2R_s}\iint_{A_{FSS}} |\vec{E}|^2 ds \tag{4.23}$$

Where A_{FSS} is the surface of the FSS where the electric field can be absorbed. This surface is indicated by the color orange in Fig. 4.6b. As it can be seen, A_{FSS} is smaller than the unit cell area.

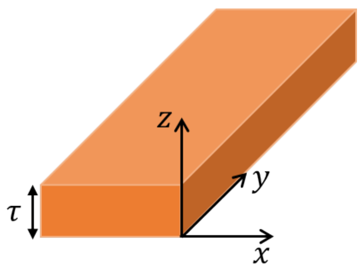

(a) An absorbing material with thickness τ.

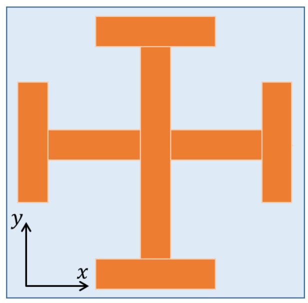

(b) The area in a unit cell that absorbs power (orange color).

Figure 4.6: Geometry of an absorber with focus on the absorbing part (orange color).

In unit cell simulation by CST, it is possible to obtain the amplitude of the TE and TM electrical fields separately over the area of the cell. Using these amplitudes and Eq. (4.19), one can express Eq. (4.23) as

$$P_{abs}^{pw} = \frac{1}{2R_s}\iint_{A_{FSS}} |E_{TM}\hat{\theta} + E_{TE}\hat{\phi}|^2 ds \tag{4.24}$$

Using the above equation, one can compare the evaluated P_{abs}^{pw} using the circuit model with the one calculated by a simulation software. As it was discussed in Section 3.4, CST uses specific amplitudes for the TE and TM electrical fields in the unit cell simulation. These amplitudes are calculated using Eq. (3.9) and were used in the MATLAB tool (see Eq. (4.9) and Eq. (4.10)). The comparison between the results from the MATLAB tool and CST using Eq. (4.24) is shown in Fig. 4.7. As it can be seen, the curves agree well. The small disagreement between the results is due to the accuracy of the amplitude of the electrical fields calculated by CST. By increasing

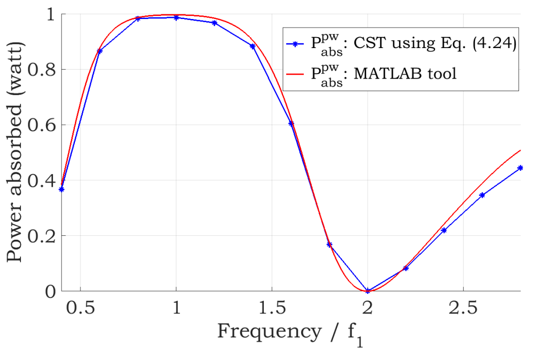

(a) Total absorbed power for f_1 FSS at broadside

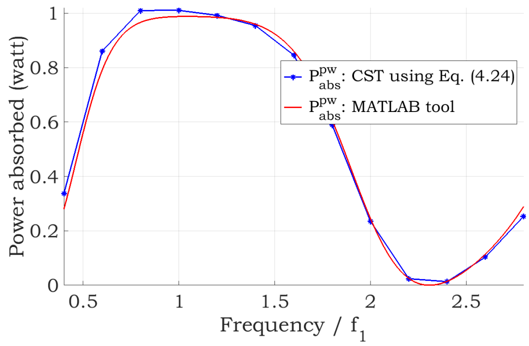

(b) Total absorbed power for f_1 FSS at $\theta = 30^o$ and $\phi = 45^o$

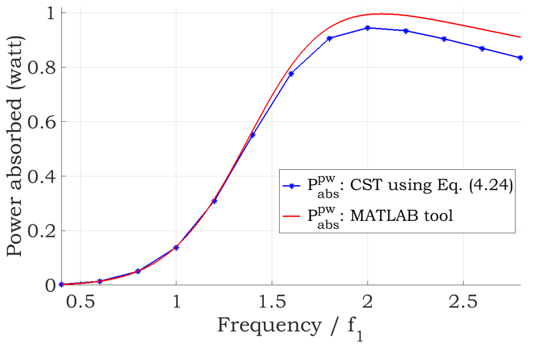

(c) Total absorbed power for f_2 FSS at broadside

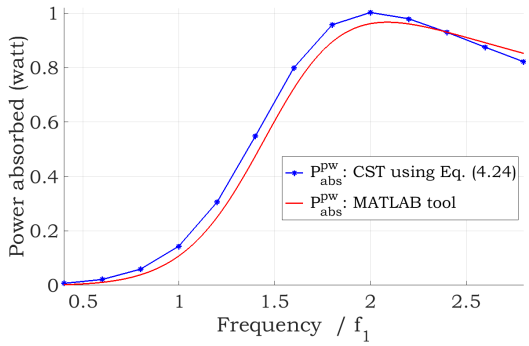

(d) Total absorbed power for f_2 FSS at $\theta = 30^o$ and $\phi = 45^o$

Figure 4.7: Comparing total absorbed power of the structure, considering coupling (blue) or not (red)

the mesh density, the results eventually converge to each other. Therefore, when a plane wave impinges on the structure, it is possible to calculated P_{abs}^{pw} as the summation of the absorbed powers by TE and TM modes (see Eq. (4.20)).

As the result of the circuit model discussion, the total absorption efficiency of the FSS for a certain plane wave can be expressed as

$$\eta_{abs}(k_x, k_y) = \frac{P_{abs}^{pw}}{P_{inc}} \simeq \frac{P_{abs}^{TM}(k_x, k_y) + P_{abs}^{TE}(k_x, k_y)}{P_{inc}(k_x, k_y)} \tag{4.25}$$

The discussed circuit model can be used for every direction of incidence of the incoming plane wave. Therefore, η_{abs} is a function of k_x and k_y.

4.2 Analysis of the Focusing System

As it was mentioned in Section 2.2.1, the focusing system is approximated as a canonical symmetric parabolic reflector. The reflector is illuminated by a plane wave and it focuses this incoming field in its focal plane Fig. 4.8. For this study, the parameters of the parabolic reflector are chosen as: $D = 20\lambda_1$ and $f_\# = 2$, which leads to a maximum rim angle, θ_0, of approximately 15^o (see Section 1.3.1).

The detector shape is a square with side length w, Fig. 4.9. The detector is a finite array of the designed FSS elements. If the element periods for each type are d_{f1} and d_{f2}, and the detector sizes for each type are w_{f1} and w_{f2}, the number of unit cells in a row of the finite array is

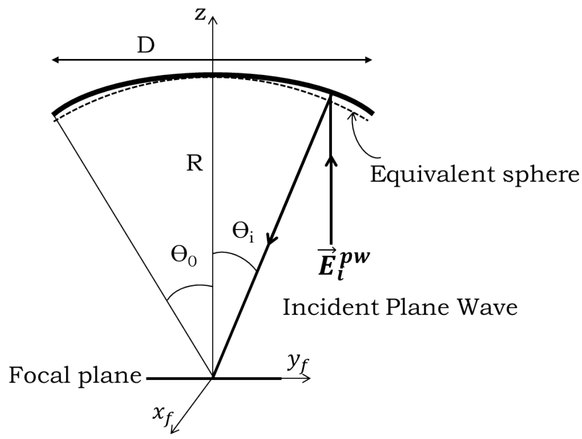

Figure 4.8: Geometry of a parabolic reflector and its focal plane.

$$n_{f1/f2} = \frac{w_{f1/f2}}{d_{f1/f2}} \tag{4.26}$$

In this project, since $w_{f1} = 1.25\lambda_1$ and $w_{f2} = 1.5\lambda_2$, for a detector working at the f_1 band 5×5 FSS unit cells are used and for a detector working at the f_2 band 6×6 FSS unit cells are used, Fig. 4.9.

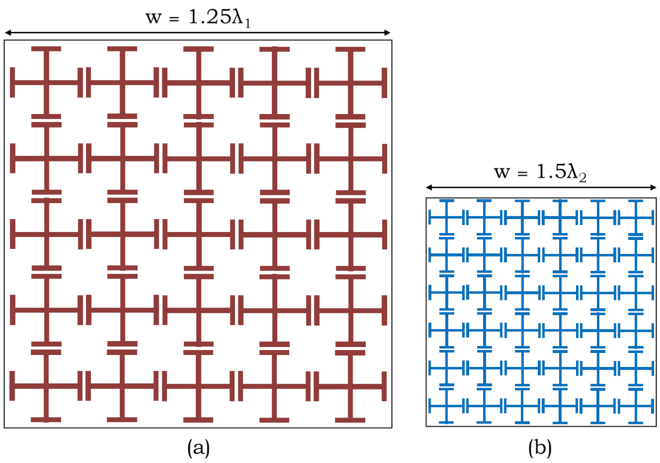

Figure 4.9: Finite array of designed FSS as the detectors in the FPA, (a) f_1 type, (b) f_2 type.

A plane wave polarized along x which impinges on a parabolic reflector from broadside, Fig. 4.8, can be expressed as

$$\vec{E}_i = E_0^{PW} e^{-jkz}\hat{x} \tag{4.27}$$

Where E_0^{PW} is the amplitude of the field. This incident plane wave generates a field on the focal plane of the reflector. The generated field is referred to as the direct field. As it was mentioned in Section 2.2.1, the direct field can be calculated using Fourier optics as the spectral Fourier transform of the field on the aperture of the reflector. Using the discussion in Section 2.2.1 and Eq. (2.53), the spectral distribution of the direct field can be expressed as

$$\vec{E}^{dir}(k_x,k_y) = E_0^{dir}\left(\frac{k_x}{k_\rho}\hat{\theta} - \frac{k_y}{k_\rho}\hat{\phi}\right) = E_\theta^{dir}\hat{\theta} + E_\phi^{dir}\hat{\phi} \tag{4.28}$$

Where $k_\rho = \sqrt{k_x^2 + k_y^2}$. The direct field was called in $\vec{E}_f$ in Section 2.2.1. The amplitude, E_0^{dir}, in Eq. (4.28) can be expressed as

$$E_0^{dir} = -\frac{4\pi kRE_0^{PW} e^{-jkR}}{k_z} \frac{1}{k+k_z} circ(k_\rho, k_{\rho 0}) \tag{4.29}$$

Where the function $circ(a,b)$ equals 1 when $|a| \leq b$, and 0 otherwise. The *circ* function is used to introduce the maximum rim angle of the reflector, θ_0, Fig. 4.8. Therefore, the spectral domain is limited by $k_{\rho 0} = k \sin(\theta_0)$. R is the distance of the apex of the reflector from its focus and k_z is the z component of the wave vector.

Using the spectral Fourier transform, the spatial distribution of the direct field is expressed as

$$\vec{e}^{dir}(x_f, y_f) = \frac{1}{4\pi^2} \int_{-\infty}^{\infty} \int_{-\infty}^{\infty} \vec{E}^{dir}(k_x, k_y) e^{jk_x x_f} e^{jk_y y_f} dk_x dk_y \tag{4.30}$$

Where x_f and y_f are the Cartesian coordinates in the focal plane (see Fig. 4.8). By comparing this expression to the one of plane waves with certain directions of propagation, $\vec{k}_i$ (i.e.Eq. (4.1)), it is visible that $\vec{e}^{dir}(x_f, y_f)$ can be modeled as a summation of all the incoming plane waves on the focal plane, Fig. 4.10. This approach is referred to as the plane wave spectrum (PWS) representation.

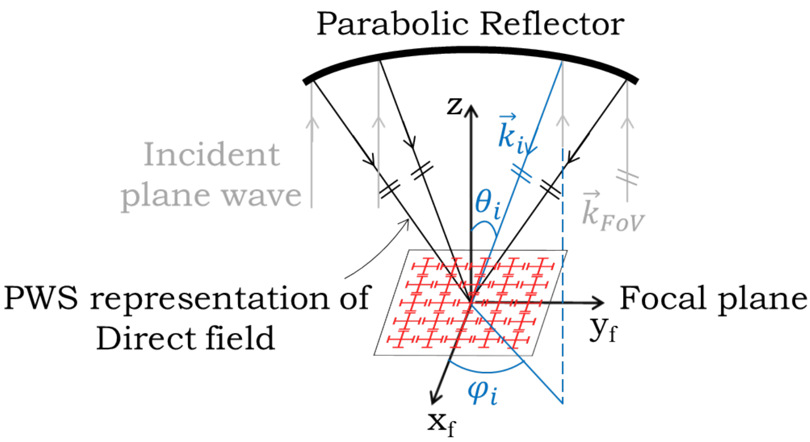

Figure 4.10: Incident plane wave coming from broadside and direct field represented as a PWS.

The field on the focal plane when the contribution of the FSS is included is referred to as the total field. The electrical field in the incident plane wave illuminating the reflector was assumed to be polarized along the x direction. Since the electric and magnetic fields in a plane wave are orthogonal to each other, the magnetic field of the plane wave is polarized along the y direction. The reflector does not introduce cross polarization term (the electric field polarized along y) at the center of its focal plane [29]. As the result, the E_y and H_x components are not present in the direct field. Moreover, as the Poynting theorem indicates, the loss is represented only by the transverse components. Therefore, the fields polarized along z are not relevant to this discussion. In conclusion, only the E_x and H_y components of the fields on the focal plane are of interest.

Using the Thevenin circuit introduced in Section 4.1 (see Fig. 4.4), the current flowing in the AA' terminal, $I^{TM/TE}(k_x, k_y)$, was obtained for each incoming $\vec{E}^{dir}(k_x, k_y)$ (see Eq. (4.14)). The voltage on the AA' terminal can be expressed as

$$V_{FSS}^{TE/TM}(k_x, k_y) = I^{TE/TM}(k_x, k_y) Z_{FSS}^{TE/TM}(k_x, k_y) \tag{4.31}$$

Using the definition of the equivalent transmission line model, these voltages and currents represent the transverse values of the total electrical and magnetic fields at the focal plane, respectively. Using the above discussions, the x-component of the total field in the spectral domain can be expressed as

$$E_x^{tot}(k_x,k_y) = E_\theta^{dir} F^{TM}(k_x,k_y)\frac{k_z}{k}\frac{k_x}{k_\rho} - E_\phi^{dir} F^{TE}(k_x,k_y)\frac{k_y}{k_\rho} \tag{4.32}$$

$$H_y^{tot}(k_x,k_y) = E_\theta^{dir}\frac{F^{TM}(k_x,k_y)}{Z_{FSS}^{TM}(k_x,k_y)}\frac{k_z}{k}\frac{k_x}{k_\rho} - E_\phi^{dir}\frac{F^{TE}(k_x,k_y)}{Z_{FSS}^{TE}(k_x,k_y)}\frac{k_y}{k_\rho} \tag{4.33}$$

Where $\frac{k_z}{k}\frac{k_x}{k_\rho}$ and $-\frac{k_y}{k_\rho}$ terms project the θ and ϕ components of the field to x-component, respectively, and $F^{TE/TM}(k_x,k_y)$ is the FSS response defined as

$$F^{TE/TM}(k_x,k_y) = \sqrt{d_x d_y}\,\frac{\left[1+\Gamma_{oc}^{TE/TM}(k_x,k_y)\right]Z_{FSS}^{TE/TM}(k_x,k_y)}{Z_{oc}^{TE/TM}(k_x,k_y)+Z_{FSS}^{TE/TM}(k_x,k_y)} \tag{4.34}$$

As an example, the response of the designed JC FSS operating at f_1 is illustrated in Fig. 4.11. The spectral domain is limited by the maximum rim angle of the reflector. For this specific reflector $\theta_0 \simeq 15$. Since θ_0 is small, the spectral domain is limited and $F^{TE/TM}(k_x,k_y)$ does not vary significantly from the response of the FSS to a broadside incoming plane wave ($F^{TE/TM}(k_x=0,k_y=0)$). Moreover, at broadside, the FSS response for TE and TM fields is the same.

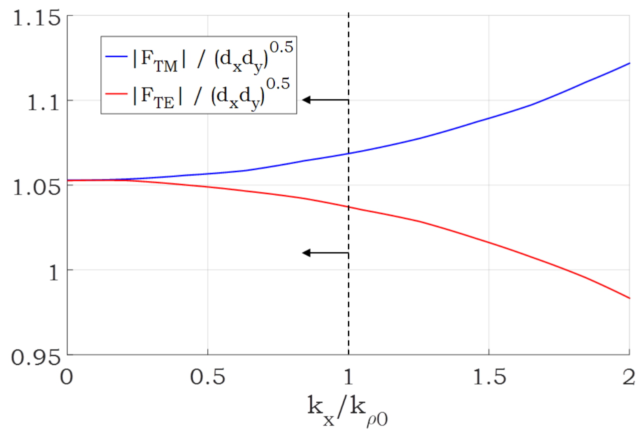

Figure 4.11: FSS response as a function of k_x when $k_y = 0$ for both TE and TM modes for f_1 absorber at the center of its operation frequency band. The marked region is the limitation on the spectral domain.

Using the spectral Fourier transform, one can calculate the spatial distribution of the total electric, $e_x^{tot}(x_f,y_f)$, and magnetic, $h_y^{tot}(x_f,y_f)$, fields. Since the domain of $\vec{E}^{dir}(k_x,k_y)$ is limited to $k_{\rho 0}$, $E_x^{tot}(k_x,k_y)$ and $H_y^{tot}(k_x,k_y)$ are also limited in the spectral domain. Therefore, the integral range of the spectral Fourier transform is limited.

The spatial distribution of $e_x^{tot}(x_f,y_f)$ is illustrate in Fig. 4.12, for $y_f = 0$, and for the detector that operates at f_1 frequency band with the mentioned reflector parameters. The figure compares the direct field and the total field to the Airy pattern approximation which was introduced in Section 1.3.1. As it was already discussed in Section 2.2.1, for a focusing system with a large $f_\#$, the direct field and the Airy pattern are approximately the same. Moreover, the direct and total fields also have approximately the same shape. This is due to the fact that the FSS response does not vary significantly for different k_x and k_y values (see Fig. 4.11).

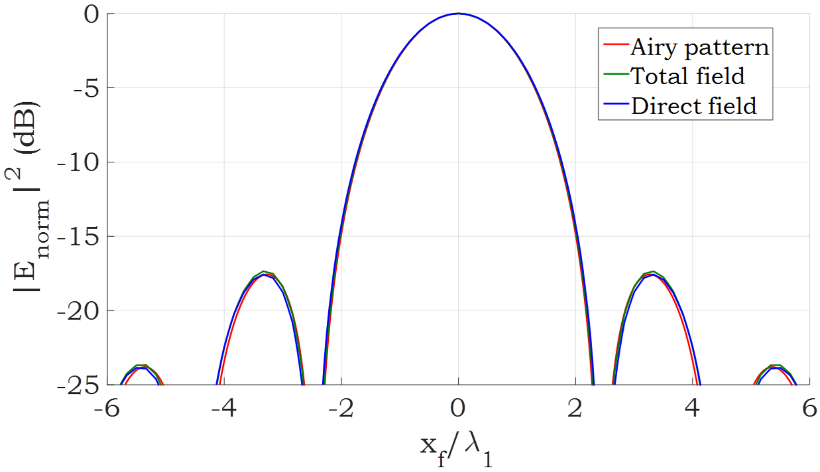

Figure 4.12: Normalized amplitude of the total electrical field in x direction compared to the direct field and the Airy pattern, at the focal plane of the imager, at f_1 frequency for the f_1 detector

The period of a unit cell element, $d = \lambda/4$ (see Fig. 4.13), is very small in comparison to the main lobe of the total field at the focal plane (see Fig. 4.12). Therefore, the total field over a unit cell can be approximated as the field at its center. It is worth to remind that the total field is calculated by assuming an infinite array of FSS elements. However, the absorbed power should be computed over the area of a detector. The Poynting theorem can be used to calculated the absorbed power over this area. The equivalent transmission line represents the average fields over the unit cell area. The term $\sqrt{d_x d_y}$ represents this averaging. Since the field is already averaged over the unit cell area, a valid approximation to evaluate this power is to calculate the power at the center of each unit cell and sum all these contributions. If n is the number of elements in the finite array, the central position of each unit cell is $x_c = m_x d$ and $y_c = m_y d$, where $m_{x/y} = -\dfrac{n-1}{2} : \dfrac{n-1}{2}$ if n is odd, and $m_{x/y} = -\dfrac{n}{2} : \dfrac{n}{2}$ if n is even.

Using the introduced approximation, the absorbed power over the area of the detector can be expressed as

$$P_{abs} \simeq \frac{1}{2} \sum_{m_x} \sum_{m_y} Re\{e_x^{tot}(m_x d, m_y d) h_y^{tot*}(m_x d, m_y d)\} \tag{4.35}$$

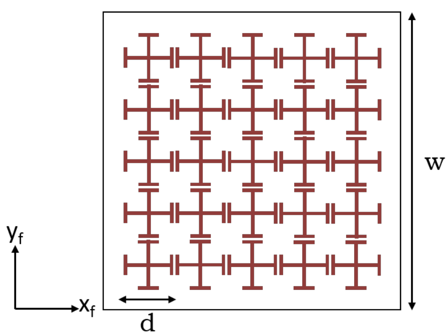

Figure 4.13: Finite array of FSS unit cells as a detector on the FPA

The broadside illumination of the reflector leads to the specific mentioned distribution of the direct field (see Fig. 4.12). Therefore, P_{abs} is the absorbed power by the detector at the center of the FPA. The total incident power on the focusing system can be approximated as the power delivered to the surface of the reflector, A_{ref}, by the incident plane wave incoming from broadside. This power can be expressed as

$$P_{inc} = \frac{1}{2\eta_0} A_{ref} |E_0^{PW}|^2 \tag{4.36}$$

Where η_0 is the impedance of the free space. Using the above discussion, one can evaluate the absorption efficiency of the imager for the detector at the center of the focal plane as

$$\eta_o = \frac{P_{abs}}{P_{inc}} \tag{4.37}$$

This efficiency is referred to as the optical efficiency when no additional loss is present in the system. The discussed steps to calculated η_o (Eq. (4.35) to (4.37)), is referred to as the full method in the remaining parts of this chapter.

The calculation for the absorption efficiency is valid for every frequency. As it was mentioned in Section 1.3.2 (see Eq. (1.22)), the averaged optical efficiency over a bandwidth can be expressed as

$$\eta_o^{avg} = \frac{1}{BW} \int_{f_L}^{f_H} \eta_o(f) df \tag{4.38}$$

Where BW is the absolute considered bandwidth, f_L is the lower limit of the bandwidth and f_H is the higher limit.

4.2.1 Approximated Analysis Method

Using the discussion on the FSS response (see Fig. 4.11), one can assume that this response is approximately equal to the broadside case for small values of k_x and k_y, i.e

$$F^{TE/TM}(k_x, k_y) \simeq F^{TE/TM}(0,0) \triangleq F(0,0) \tag{4.39}$$

The FSS impedance, $Z_{FSS}^{TE/TM}(k_x, k_y)$, also does not vary significantly for small values of k_x and k_y. Therefore, this impedance can also be approximated as

$$Z_{FSS}^{TE/TM}(k_x, k_y) \simeq Z_{FSS}^{TE/TM}(0,0) \triangleq Z_{FSS}(0,0) \tag{4.40}$$

Using Eq. (4.39) and Eq. (4.40), as a first order of approximation the total fields can be expressed as

$$E_x^{tot}(k_x, k_y) \simeq F(0,0) E_x^{dir}(k_x, k_y) \tag{4.41}$$

$$H_y^{tot}(k_x, k_y) \simeq \frac{F(0,0)}{Z_{FSS}(0,0)} E_x^{dir}(k_x, k_y) \tag{4.42}$$

Where $E_x^{dir}(k_x, k_y)$ is

$$E_x^{dir}(k_x, k_y) = E_\theta^{dir} \frac{k_z}{k} \frac{k_x}{k_\rho} - E_\phi^{dir} \frac{k_y}{k_\rho} \tag{4.43}$$

Using Eq. (4.41) and Eq. (4.42), the spatial distribution of the total fields can be approximated as

$$e_x^{tot}(x_f, y_f) \simeq F(0,0) \frac{1}{4\pi^2} \int_{-\infty}^{\infty} \int_{-\infty}^{\infty} E_x^{dir}(k_x, k_y) e^{jk_x x_f} e^{jk_y y_f} dk_x dk_y = F(0,0) e_x^{dir}(x_f, y_f) \tag{4.44}$$

$$h_y^{tot}(x_f, y_f) \simeq \frac{F(0,0)}{Z_{FSS}(0,0)} \frac{1}{4\pi^2} \int_{-\infty}^{\infty} \int_{-\infty}^{\infty} E_x^{dir}(k_x, k_y) e^{jk_x x_f} e^{jk_y y_f} dk_x dk_y = \frac{F(0,0)}{Z_{FSS}(0,0)} e_x^{dir}(x_f, y_f) \tag{4.45}$$

This result is visible in Fig. 4.12. Therefore, it is possible to compute the total field approximately by multiplying the direct field by a constant.

One can relate $e_x^{tot}(x_f, y_f)$ and $h_y^{tot}(x_f, y_f)$ by an impedance as

$$Z^{tot}(x_f, y_f) = \frac{e_x^{tot}(x_f, y_f)}{h_y^{tot}(x_f, y_f)} \tag{4.46}$$

By using Eq. (4.44) and Eq. (4.45), the above equation can be approximated as

$$Z^{tot}(x_f, y_f) \simeq \frac{F(0,0)e_x^{dir}(x_f, y_f)}{\frac{F(0,0)}{Z_{FSS}(0,0)} e_x^{dir}(x_f, y_f)} = Z_{FSS}(0,0) \tag{4.47}$$

Using Eq. (4.46), the accurate value of $Z^{tot}(x_f, y_f)$ for the f_1 absorber is calculated and compared to the approximated expression of Eq. (4.47) in Fig. 4.14. Since the two curves are close, the figure indicates that the approximation is valid. Moreover, $Z^{tot}(x_f, y_f)$ is constant over the focal plane. Therefore, the notation: Z^{tot} is used in the following discussions. By using the Z_{tot}

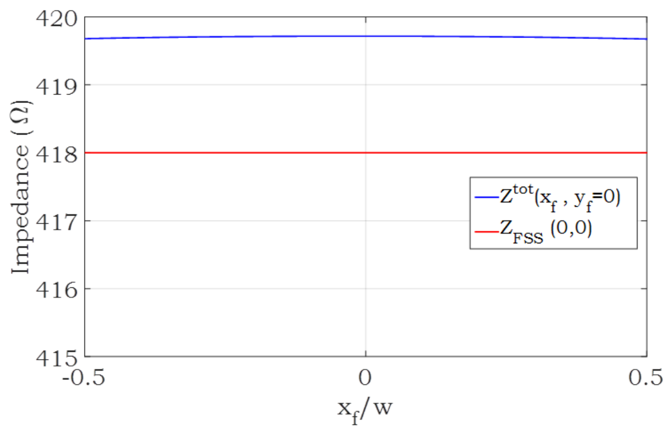

Figure 4.14: Z_{tot} as a function of x_f when $y_f = 0$ compared to the $Z_{FSS}(0,0)$ for f_1 absorber at f_1 frequency.

concept, Eq. (4.35) can be simplified as

$$P_{abs} = \frac{1}{2Re\{Z^{tot}\}} \sum_{m_x} \sum_{m_y} |e_x^{tot}(m_x d, m_y d)|^2 \tag{4.48}$$

By considering the above approximations, the total absorbed power can be expressed as

$$P_{abs} = \frac{|F(0,0)|^2}{d_x d_y} \frac{1}{2Re\{Z^{tot}\}} \sum_{m_x} \sum_{m_y} |e_x^{dir}(m_x d, m_y d)|^2 d_x d_y \tag{4.49}$$

If the reflection of the fields from the surface of the focusing system is considered lossless, one can assume that the incident power is equal to the power available over the entire focal plane. Therefore

$$P_{inc} = \frac{1}{2\eta_0} A_{ref} |E_0^{PW}|^2 \simeq \frac{1}{2\eta_0} \iint_{-\infty}^{\infty} |e_x^{dir}(x_f, y_f)|^2 ds \tag{4.50}$$

Using Eq. (4.50) and Eq. (4.49), the absorption efficiency of the imager can be expressed as

$$\eta_o = \frac{1}{\frac{1}{2\eta_0} \iint_{-\infty}^{\infty} |e_x^{dir}(x_f, y_f)|^2 ds} \frac{|F(0,0)|^2}{d_x d_y} \frac{1}{2Re\{Z^{tot}\}} \sum_{m_x} \sum_{m_y} |e_x^{dir}(m_x d, m_y d)|^2 d_x d_y \tag{4.51}$$

Using the definition of the spillover efficiency (see Section 1.3.2), the above expression can be simplified as

$$\eta_o = \frac{|F(0,0)|^2}{d_x d_y} \frac{\eta_0}{Re\{Z^{tot}\}} \eta_{SO} \tag{4.52}$$

Where the spillover efficiency, η_{SO}, is expressed as

$$\eta_{SO} = \frac{\sum_{m_x} \sum_{m_y} |e_x^{dir}(m_x d, m_y d)|^2 d_x d_y}{\iint_{-\infty}^{\infty} |e_x^{dir}(x_f, y_f)|^2 ds} \tag{4.53}$$

The term $A = \frac{|F(0,0)|^2}{d_x d_y} \frac{\eta_0}{Re\{Z^{tot}\}}$ can be related to the absorption efficiency of the FSS at broadside (see Eq. (4.25)) by following the steps below. Using Eq. (4.34), $|F(0,0)|^2$ can be expressed as

$$|F(0,0)|^2 = d_x d_y \frac{[1+\Gamma_{oc}(0,0)]^2 Z_{FSS}(0,0)^2}{[Z_{oc}(0,0)+Z_{FSS}(0,0)]^2} \tag{4.54}$$

Where $Z_{oc}(0,0) = Z_{oc}^{TE/TM}(0,0)$, and $\Gamma_{oc}(0,0) = \Gamma_{oc}^{TE/TM}(0,0)$. Therefore, A can be simplified to

$$A = \frac{[1+\Gamma_{oc}(0,0)]^2 \eta_0 Z_{FSS}(0,0)^2}{Re\{Z_{tot}\}[Z_{oc}(0,0)+Z_{FSS}(0,0)]^2} \tag{4.55}$$

The absorption efficiency at broadside using Eq. (4.25) is calculated as

$$\eta_{abs}(k_x=0,k_y=0) = \frac{\frac{1}{2}\frac{|V_{oc}^{TM}(0,0)|^2}{[Z_{oc}^{TM}(0,0)+Z_{FSS}^{TM}(0,0)]^2} Z_{FSS}^{TM}(0,0) + \frac{1}{2}\frac{|V_{oc}^{TE}(0,0)|^2}{[Z_{oc}^{TE}(0,0)+Z_{FSS}^{TE}(0,0)]^2} Z_{FSS}^{TE}(0,0)}{\frac{1}{2\eta_0}|\vec{E}_{dir}|^2 d_x d_y} \tag{4.56}$$

By using Eq. (4.9) to (4.11), the expressions for $V_{oc}^{TM/TE}$ at broadside can be substitute with

$$V_{oc}^{TM}(0,0) = \sqrt{d_x d_y} e_\theta^{dir}(1+\Gamma_{oc}(0,0)) \tag{4.57}$$

$$V_{oc}^{TE}(0,0) = \sqrt{d_x d_y} e_\phi^{dir}(1+\Gamma_{oc}(0,0)) \tag{4.58}$$

Moreover, using the results of the discussion in Section 4.1, $|\vec{E}_{dir}|^2$ can be approximated as

$$|\vec{E}_{dir}|^2 \simeq |e_\theta^{dir}|^2 + |e_\phi^{dir}|^2 \tag{4.59}$$

By using Eq. (4.57) to (4.59), one can simplify Eq. (4.56) as

$$\eta_{abs}(k_x=0,k_y=0) = \frac{[1+\Gamma_{oc}(0,0)]^2 Z_{FSS}(0,0)\eta_0}{[Z_{oc}(0,0)+Z_{FSS}(0,0)]^2} \tag{4.60}$$

Eq. (4.60) and Eq. (4.55) are equal if the approximation: $Z_{FSS}(0,0) \simeq Re\{Z^{tot}\}$ is valid. This approximation was already validated in Eq. (4.47) (see Fig. 4.14). Therefore, Eq. (4.52) can be simplified as

$$\eta_o \simeq \eta_{abs}(k_x=0,k_y=0)\eta_{SO} \tag{4.61}$$

The above steps which leads to the expression of η_o as Eq. (4.61) is referred to as the approximated method in the remaining parts of this chapter.

When deriving an analytical expression for the spectral representation of the direct field at the focal plane is difficult, the discussed approximated model is extremely useful. Using computational software such as GRASP, one can obtain the spatial distribution of the direct field generated by a specific optical system. Furthermore, using Eq. (4.61), one can calculated the optical efficiency, η_o, using the spillover efficiency (see Eq. (4.55)) and the absorption efficiency of the absorber based FSS at broadside.

(a) (b)

Figure 4.15: Representation of the fields focused by the quasi-optical system on the FSS array: (a) $\theta_{FoV} = 0$, (b) $\theta_{FoV} \neq 0$.

4.2.2 Angular Response of Absorber Based Imaging System

Every point in the FoV radiates a field that is focused at a different spot on the focal plane of the imaging system. Part of the power associated to this field is received by each absorbers in the FPA. For each point in the FoV, the amount of power received by an absorber can be related to the corresponding absorption efficiency. The angular response of the imager to a point source is defined as the absorption efficiency of the imager as a function of the angle of incidence of the plane waves coming from the FoV, θ_{FoV}, see Fig. 4.15. As it was discussed in Section 2.2.1, the FO calculates the field at the focal plane of a focusing system using the spectral aperture field. For small incidence angles, the spectrum of the aperture field can be assumed to be the same as the one for broadside except for a linear phase shift associated to θ_{FoV} [58]. Therefore, we can assume to have the same spatial field in the focal plane but with a translation related to this linear phase shift. This approximation is only valid for the points close to the focus of the reflector. Therefore, in this discussion only the angular response when the detector is at the center of the FPA is investigated. For a specific direction of the incidence, $\vec{k}_{FoV}$, the field will be shifted in the focal plane as (see Fig. 4.15)

$$\vec{\rho}_s = \frac{R}{k_0}\vec{k}_{\rho FoV} \tag{4.62}$$

Where $k_{\rho FoV} = k_0 \sin(\theta_{FoV})$.

In order to calculate the angular response of the imager, Eq. (4.48) can be rearranged as

$$P_{abs}(\vec{k}_{FoV}) = \frac{1}{2Re\{Z^{tot}\}d_x d_y} \iint_{-\infty}^{+\infty} |e_x^{tot}(\vec{\rho}_f - \vec{\rho}_s)|^2 \Pi(\vec{\rho}_f, w)\, dx_f\, dy_f \tag{4.63}$$

Where $\Pi(\vec{\rho}_f, w)$ represents the area of the squared detector of side length w. Using the above discussions, the angular response of the imager can be approximated as

$$\eta_{img}(\vec{k}_{FoV}) = \frac{1}{P_{inc}} \frac{1}{2Re\{Z^{tot}\}d_x d_y} \iint_{-\infty}^{+\infty} |e_x^{tot}(\vec{\rho}_f - \vec{\rho}_s)|^2 \Pi(\vec{\rho}_f, w)\, dx_f\, dy_f \tag{4.64}$$

This equation can be expressed as an efficiency for broadside multiplied by an normalized angular pattern, i.e. $\eta_{img}(\vec{k}_{FoV}) = \eta_o F_a(\vec{k}_{FoV})$. Indeed, as shown in section 4.2.1, $\eta_o \simeq \eta_{abs}(k_x = 0, k_y = 0)\eta_{SO}$. This expression represents a convolution integral between the absolute value of

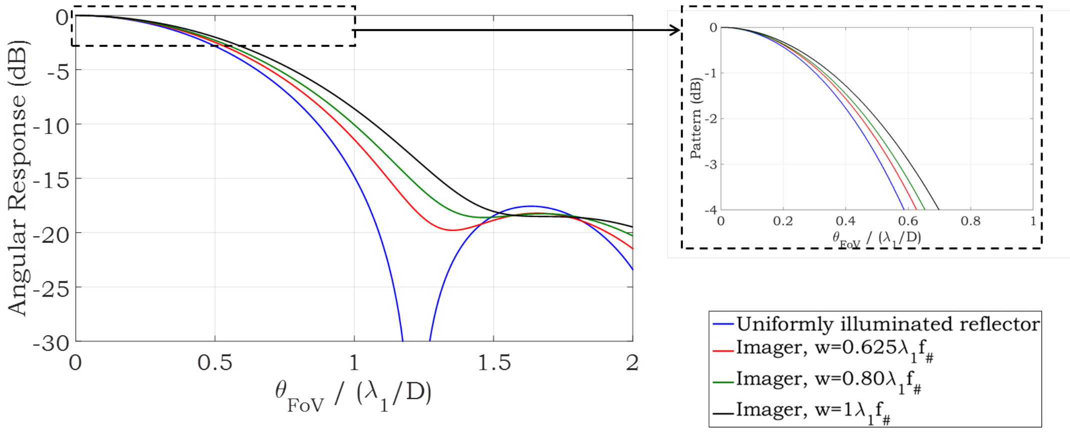

Figure 4.16: Angular response of the imager in comparison to the response of a uniformly illuminated reflector, for f_1 detector with different sizes at f_1 frequency.

the electric field at the focal plane and the rectangular function representing the area of the detector. In a convolution integral the domain of the result is equal to the summation of the domains of each convoluted function. Therefore, if the domain of one function enlarges the result of the integral also will have a larger domain. This property indicates that by enlarging the area of the detector its angular response widens. The normalized angular response of the imager for different detector sizes is calculated using the approximated method in Fig. 4.16. The discussed response can be compared to the one obtained by considering a uniformly illuminated reflector that radiates in far-field. The latter with the same reflector parameters is also reported in the figure. The figure indicates that the main lobe of the angular response of an absorber coupled to optics is always wider than the one of a uniformly illuminated reflector with the same parameters. Moreover, the side lobe level in the response of the imager is comparable to the one of the uniformly illuminated case. The angular response of the uniformly illuminated reflector is defined similar to the one of the imager when the detector is just a point in the FPA. Therefore, by substituting $\Pi(\vec{\rho}_f, w)$ with $\delta(\vec{\rho}_f)$ in Eq. (4.64), both responses should be equal.

The resolution of an imager is defined as the half power beam width (HPBW) of its normalized angular response. The resolution indicates the angular distance between two points in the FoV that the detector can resolve by $-3dB$ difference in the absorption efficiency. The resolution of the discussed imager for the f_1 absorber is illustrated in Fig. 4.17 for different detector sizes. This resolution is normalized to the HPBW of the angular response of the uniformly illuminated reflector. The latter can be calculated analytically using the Airy pattern approximation similar to the discussion in Section 1.3.2. As it can be seen in the figure the resolution enlarges as the detector area increases. Similar results were presented in [59]. Moreover, using the above comparison between the responses, it is expected that for a very small detector size, the normalized resolution is equal to 1.

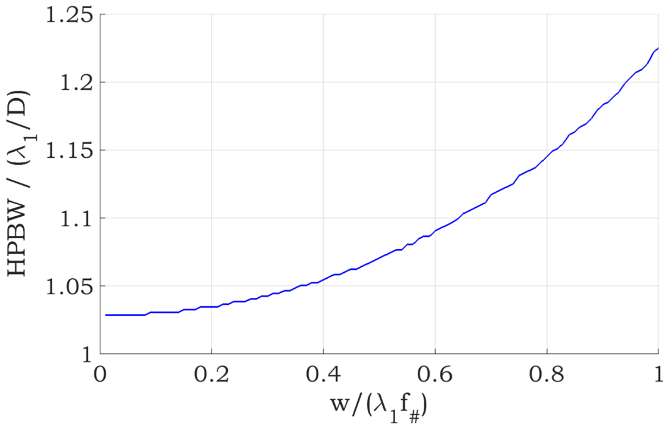

Figure 4.17: Normalized value of the resolution for different detector sizes, at f_1 frequency.

4.3 Evaluation of System Performance

4.3.1 System Performance: Parabolic Reflector

In this section the discussed methods are used to evaluate the performance of an imager in terms of its absorption efficiency when the focusing system is a parabolic reflector with the discussed geometrical parameters (see Section 4.2). In Fig. 4.18, the spillover efficiency, the absorption efficiency of the FSS and the absorption efficiency of the imager calculated using both the full and approximated methods are illustrated for broadside incidence. For focusing systems with large f-number, the direct field can be approximated by the Airy pattern (see Section 2.2.1). This approximation is used in calculating the spillover efficiency. The Airy pattern becomes more focused as the frequency increases. Therefore, the spillover efficiency increases with frequency. The absorption efficiency of the imager is fundamentally limited by spillover efficiency. However, this absorption efficiency is also related to the frequency response of the absorber based FSS.

The focusing system filters the frequencies higher than $2.6f_1$. Moreover, the absorption efficiency of the imager is approximately 0 for frequencies lower than $0.4f_1$. Therefore, the frequency range of the imager is approximately $0.4f_1$ to $2.6f_1$. The detectors absorb all the power in this frequency range. In this section, two bandwidths are chosen for each absorber type. The bandwidth of operation, BW_{op}, and the rejection band, BW_{rej}. This bands are illustrated in Fig. 4.18. For f_1 absorber these bandwidths are chosen as: $BW_{op}^{f1} = 0.4f_1 : 1.75f_1$, $BW_{rej}^{f1} = 1.75f_1 : 2.6f_1$. The bands for the f_2 absorber are the opposite of the one of f_1, $BW_{op}^{f2} = 1.75f_1 : 2.6f_1$, $BW_{rej}^{f2} = 0.4f_1 : 1.75f_1$. The power absorbed in the out band is considered as noise. The absorption efficiency of the imager over the bandwidth, η_{BW} (see Eq. (4.38)), for both the designed f_1 and f_2 absorber types (see Table 3.1 and Table 3.2) is calculated using the defined bandwidths and reported in Table 4.1.

Table 4.1: The absorption efficiency of the imager over the bandwidth for the f_1 and f_2 absorbers.

Relative Band width	Operation band	Rejection band
η_o^{avg}, for f_1 absorber Full / Approximated method	24.74% / 23.96%	9.62% / 8.92%
η_o^{avg}, for f_2 absorber Full / Approximated method	40.07% / 39.26%	7.13% / 7.50%

Since the f_2 absorber has a larger area in terms of wavelength, it has a better spillover effi-

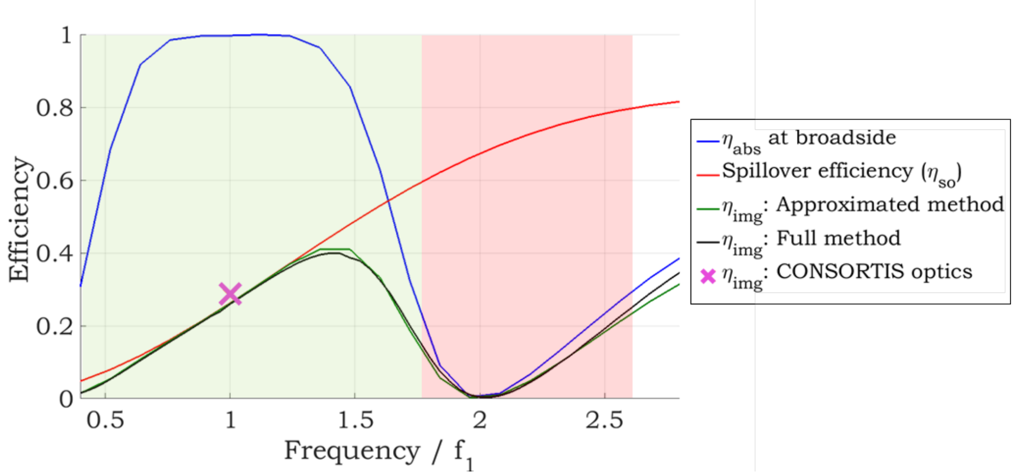

(a) For the detector working at f_1 band.

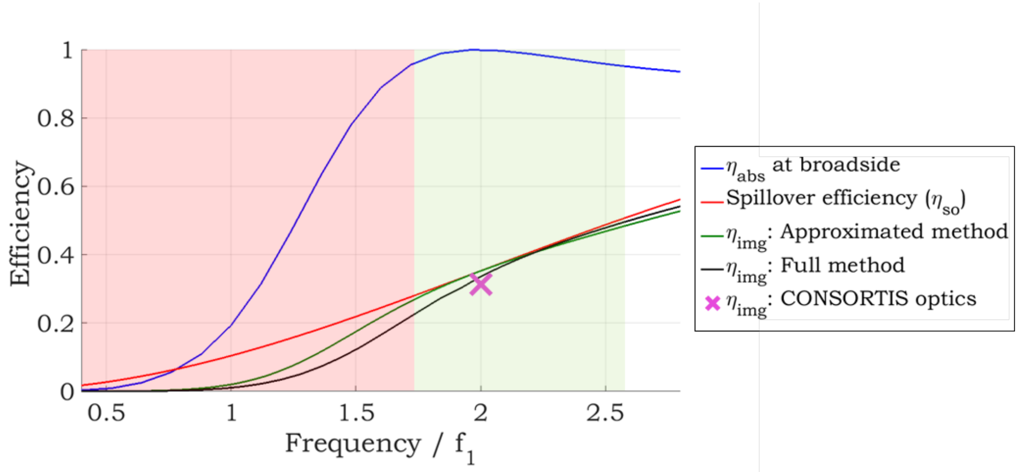

(b) For the detector working at f_2 band.

Figure 4.18: Discussed efficiencies for the detectors using the free standing FSS design. The green and red areas correspond to the operational and rejection bands, respectively.

ciency in the operation band. As for the rejection band, since f_2 absorber uses a ground plane very close to the FSS, the absorption is low over the entire rejection band. Therefore, f_2 absorbers have a better rejection performance. In the table and the figure, small differences are visible between the absorption efficiency of the imager calculated using the full and the approximated methods. This is due to the fact that the full method considers the FSS response in both the broadside and oblique incidences. This difference is more visible in the f_2 absorber specifically around the operation band.

Since the full and approximated methods are approximately the same at the central frequency of the operation band of both the f_1 and f_2 absorbers, only the approximated method is used to calculated the angular response of the imager. This response is illustrated in Fig. 4.19. As it was mentioned before, the side lob levels of these responses are comparable to the one of the uniformly illuminated reflector. The resolution of both absorber types are compared to the one of the uniformly illuminated reflector in Fig. 4.19. As it was expected, the imager has larger resolutions than the uniformly illuminated reflector. Moreover, since the f_2 absorber has a larger electrical size, the imager coupled to a f_2 detector has a larger resolution in terms of wavelength.

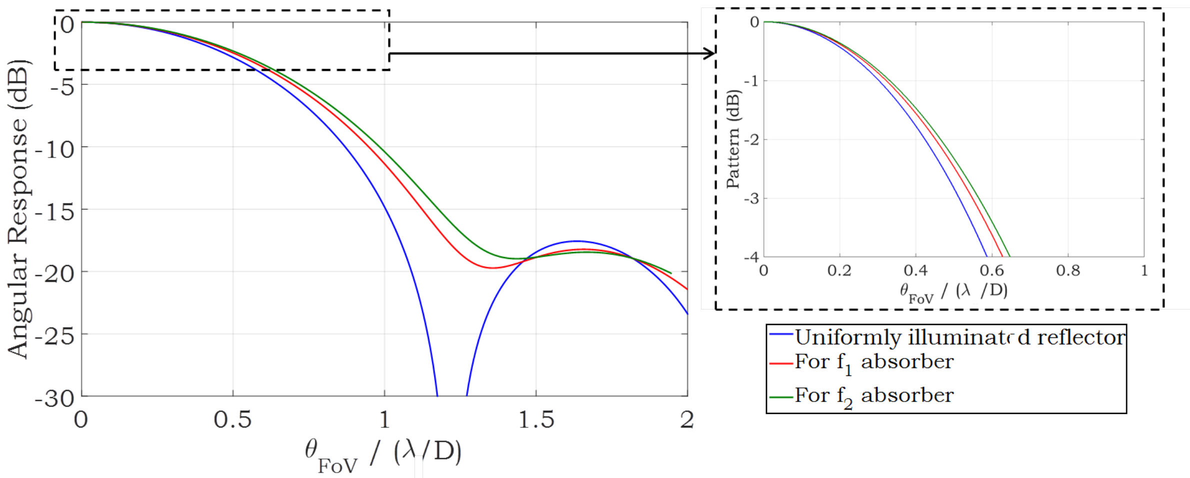

Figure 4.19: Angular response of the imager calculated as a function of positions in the FoV, compared to the one of a uniformly illuminated reflector.

Table 4.2: Resolution of the detector coupled imager compared to the one of the uniformly illuminated reflector.

	f_1 absorber	f_2 absorber
$\Delta\theta_{FoV}$, detector coupled to reflector	$1.1\lambda_1 D$	$1.13\lambda_2 D$
$\Delta\theta_{FoV}$, the uniformly illuminated reflector	$1.02\lambda_1 D$	$1.02\lambda_2 D$

FSS Based Absorber Including the KID resonator lines

The free standing design of the absorber based FSS was modified in Section 3.5 to compensate the effects that the KID resonator lines and the dielectric layer impose on the performance of the structure. The approximated method can also be used to evaluate the absorption efficiency of the imager when this modified design is used. The spillover efficiency is determined by the size of the detector and the direct field generated by the parabolic reflector, both of which do not change in this new case. Therefore, only the η_o and $\eta_{abs}(0,0)$ are reported in Fig. 4.20 for both the horizontal and vertical excitations. The η_o^{avg} for the same cases as the free standing design is reported in Table 4.3. By comparing results of the latter tables with the ones in Table 4.1, it is visible that the optical efficiency of the imager in both cases are comparable despite the slight differences between the FSS response of each design. This is due to the fact that the efficiency is averaged over the bandwidth.

As it was discussed in Section 1.3.2, the NETD can be calculated for an imager by using Eq. (1.28). For a lossless optical system η_o^{avg} can be expressed as Eq. (4.38). Using the values provided in Table 4.1, NETD for each case is calculated in Table 4.4. As it can be seen, the NETD is lower than 1 Kelvin for all the cases, which was the requirement of this imaging system.

Table 4.3: The absorption efficiency over bandwidth for detectors designed by including the KID resonator lines.

Relative Band width	Operation band	Rejection band
η_o^{avg} for f_1 absorber Horizontal / Vertical mode	25.99% / 24.49%	9.72% / 9.29%
η_o^{avg} for f_2 absorber Horizontal / Vertical mode	36.15% / 36.97%	3.95% / 5.47%

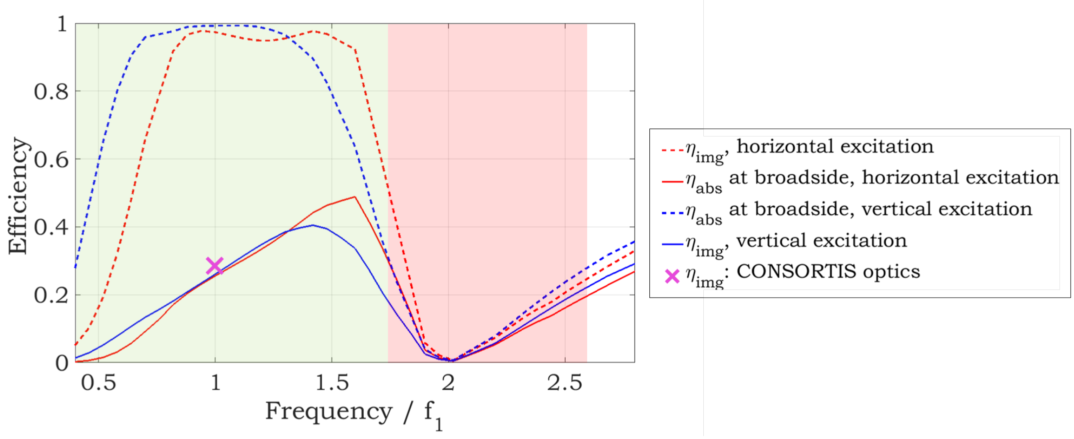

(a) For the detector working at f_1 band.

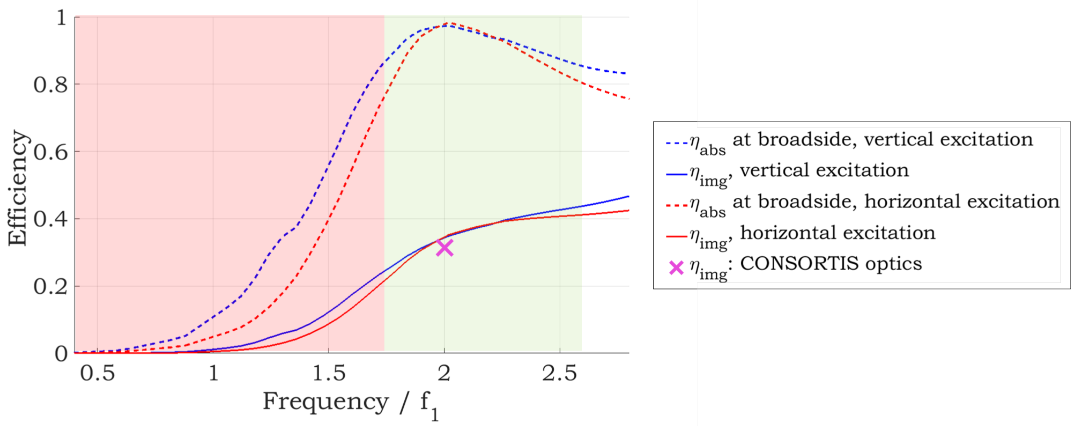

(b) For the detector working at f_2 band.

Figure 4.20: Discussed efficiencies for the design introduced in Section 3.5. The green and red areas correspond to the operational and rejection bands, respectively.

Table 4.4: NETD of the imager coupled to the design of the detector which included the KID resonator lines.

	NETD
f_1 detector Horizontal / Vertical mode	0.102 K / 0.108 K
f_2 detector Horizontal / Vertical mode	0.140 K / 0.137 K

4.3.2 System Performance: CONSORTIS Optics

As it was mentioned in Section 1.4, in CONSORTIS project a more complicated optical system is used. This focusing system has a f-number equal to 2 and a magnification factor equal to 8.33 (see Section 1.3.1). In this section, the performance of the imager is evaluated for this specific focusing system for both the detector at the center of the FPA and the edge. To achieve this goal, the spatial distribution of the direct field on the focal plane of this focusing system is obtained using GRASP simulation software. This distribution is then used to calculated the absorption efficiency of the imager using the approximated method. The plane waves incoming on the detector at the edge of the FPA have the incidence angles $8.8^o < \theta_i < 28.1^o$ and $-90^o < \phi_i < 90^o$, see Fig. 4.21. This is related to the geometry of CONSORTIS optics. Therefore, instead of using the absorption efficiency of the FSS at broadside, for the edge detector case the FSS behavior should be approximated by its absorption efficiency at the incidence angle in the middle of the beam: $\theta_i^{edge} = 17.4^o$ and $\phi_i^{edge} = 0^o$.

The angular response of the imager for both the f_1 and f_2 absorber types at their corresponding central frequencies are illustrated in Fig. 4.22. These responses are compared to the shape of their corresponding magnified direct fields. The main lobe of the former is wider than the latter as expected, and the side lobe level of the former is comparable to the latter. Since the direct field generated at the edge of the FPA is not symmetric, as an example, the angular response for the edge detector is shown at two cuts. In the figures, the angular response of the edge detector is normalized by the term θ_P. This term represents the angular position in the FoV that generates the focal field at the center of the edge detector (see Fig. 4.21). Moreover, the resolution for an asymmetric angular response is introduced as the HPBW of the response averaged over the ϕ cuts. The resolution of CONSORTIS imager for this cases are reported in Table 4.5. The absorption efficiency of the imager, η_o, is calculated by using the approximated method. In other words, this efficiency is calculated by multiplying the corresponding spillover efficiency, η_{so}, and the absorption efficiency of the FSS based absorber at the middle of its incidence beam, $\eta_{abs}(\theta_i, \phi_i)$ ($\eta_{abs}(0,0)$ for the detector at the center and $\eta_{abs}(\theta_i^{edge}, \phi_i^{edge})$ for the detector at the edge). These efficiencies are calculated for both f_1 and f_2 detectors at the center of their operation bands and reported also in the table. The results in the table indicated that the enlargement of the resolution in comparison to the reference (magnified direct field) must be consider in the design of the imager. In order to have a more accurate result, one should obtain the spectral distribution of the direct field and use the full method to evaluate the performance of the detector at the edge of the FPA.

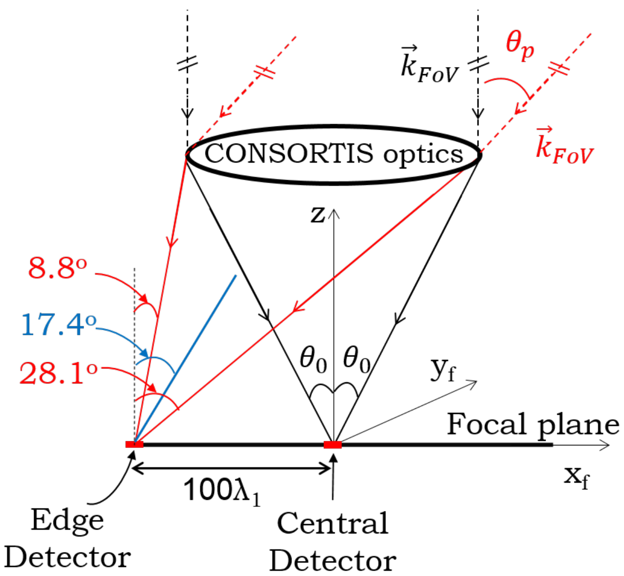

Figure 4.21: Comparison between the possible incidence angles of plane waves coming to the edge and central detector at the FPA of CONSORTIS optics.

In CONSORTIS, a lens based quasi-optical system is used. Therefore, reflection at the air-lens interfaces and absorption loss inside the lenses occur and can be significant depending on the material chosen to design the system (the approximation in Eq. (4.50) is not valid anymore). These additional losses have to be included in the efficiency calculation. For this reason, the averaged optical efficiency has to be modified as

$$\eta_o^{avg} = \frac{1}{BW} \int_{f_L}^{f_H} \eta_o(f)\eta_{diel}(f)df \tag{4.65}$$

where $\eta_{diel}(f)$ is the additional loss due to the use of lenses. The material used to design the

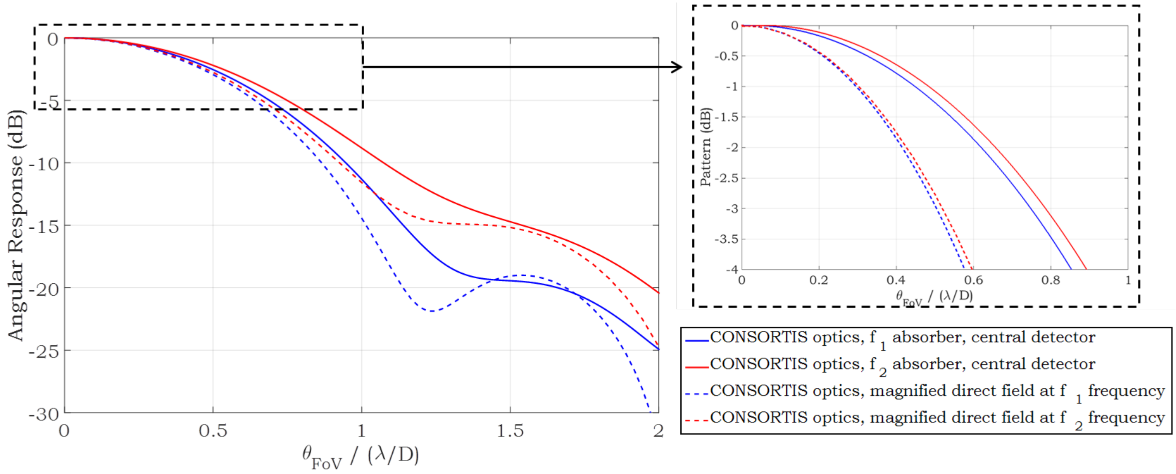

(a) Detector at the center of FPA, for $\phi_{FoV} = 0^o$ cut.

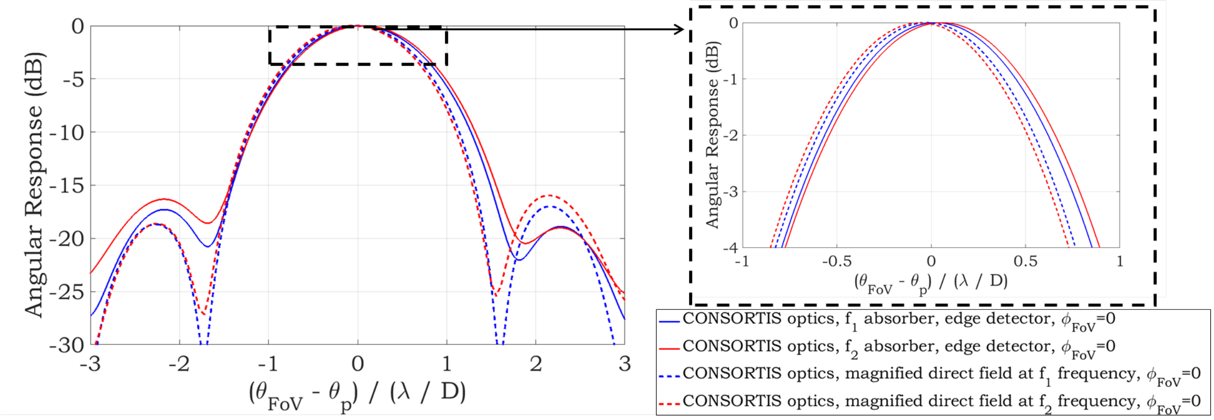

(b) Detector at the edge of FPA, for $\phi_{FoV} = 0^o$ cut.

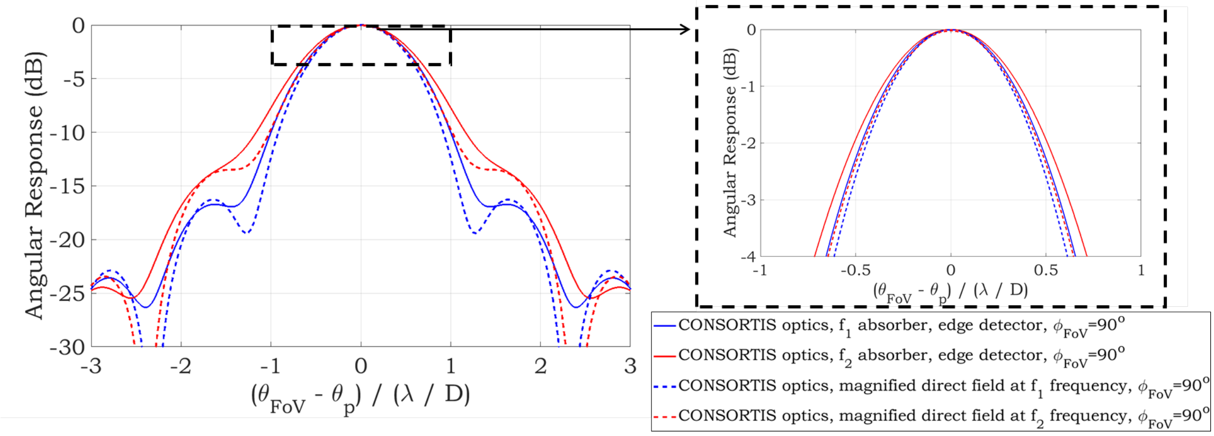

(c) Detector at the edge of FPA, for $\phi_{FoV} = 90^o$ cut.

Figure 4.22: Angular response of CONSORTIS imager for the detector, compared to the magnified version of the direct field

lens system of CONSORTIS has a low dielectric permittivity and high absorption loss. The low value of the dielectric constant allows to have low reflection loss at the air-material interface. The latter can be further reduced by using matching layers over the surfaces of the lenses. Therefore, the reflection loss can be neglected in the calculation of the total efficiency. On the other hand, the absorption loss in the lens material is significant and depends on the frequency. The absorption loss of a Gaussian beam propagating inside a slab of a material with thickness

Table 4.5: Resolution and the absorption efficiency of the detector coupled CONSORTIS optics.

	f_1 absorber, center detector	f_1 absorber, edge detector	f_2 absorber, center detector	f_2 absorber, edge detector
Averaged resolution	$1.05\lambda_1 D$	$1.31\lambda_1 D$	$1.16\lambda_2 D$	$1.37\lambda_2 D$
η_{so}	28.5%	20.57%	31.49%	25.19%
$\eta_{abs}(\theta_i,\phi_i)$	99.7%	99.5%	100%	99.9%
η_o (without additional losses)	28.41%	20.47%	31.49%	25.16%

τ_o, can be expressed as [60]

$$\eta_{diel} = e^{-\alpha\tau_o} \tag{4.66}$$

Where α is the attenuation constant of the material and is expressed as

$$\alpha = \frac{2\pi n \tan(\delta)}{\lambda} \tag{4.67}$$

Where n and $\tan(\delta)$ are the refraction index and the tangent loss of the material, respectively.

The imager efficiencies, η_o, considering the optics of CONSORTIS are reported as crosses in Fig.s 4.18 and 4.20 for both f_1 and f_2. Based on these comparisons, one can assume that the performance of the CONSORTIS optics is comparable to the one of the parabolic reflector. Therefore, the frequency variation of the efficiency of the parabolic reflector is used in Eq. (4.65) to evaluate the performance of the actual optics configuration. The optical efficiency including the dielectric loss is reported in Table 4.6. By comparing these results with Table 4.3, it is visible that the efficiency is lower because of the dielectric loss. Since the dielectric loss as defined in Eq. (4.66) becomes larger as the frequency increases, its effect is more significant for f_2 absorbers. The NETD values of the imager including the new calculation of the efficiency are summarized in Table 4.7. The NETD is increased with respect to the case with no dielectric loss (see Table 4.4). However, the achieved NETD for the central detector is less than 0.3 K, much lower than the requirement of the project, NETD = 1 K. For the edge detector, the dielectric loss and the absorption efficiency of the FFS are approximately the same as the central detector. The main variation in the efficiency (and therefore, the NETD) is due to an increase of the spillover loss. As reported in Table 4.5, the spillover efficiency is decreased approximately by a factor 30% and 20% for the f_1 and f_2 absorbers, respectively. Since the NETD is inversely proportional to the efficiency, it can be assumed that, at the edge of the FPA, the NETD is lower than 0.2 K and 0.3 K for the f_1 and f_2 absorbers, respectively. Therefore, we can conclude that the requirements of the project on the NETD are largely met.

Table 4.6: The optical efficiency of the CONSORTIS optics, including dielectric loss.

Relative Band width	Operation band	Rejection band
η_o^{avg} for f_1 absorber Horizontal / Vertical mode	21% / 20.10%	6.18% / 5.78%
η_o^{avg} for f_2 absorber Horizontal / Vertical mode	23.22% / 23.73%	2.98% / 4.18%

Table 4.7: NETD of the CONSORTIS optics, including dielectric loss.

	NETD for the ceneter detector	NETD for the edge detector
f_1 detector Horizontal / Vertical mode	0.126 K / 0.131 K	0.180 K / 0.187 K
f_2 detector Horizontal / Vertical mode	0.218 K / 0.214 K	0.272 K / 0.268 K

4.4 Conclusion

Linking the analysis of both the detector and the focusing system in the spectral domain is possible, which leads to evaluating the performance of the total imaging system. In this chapter a circuit model was purposed for the FSS structure to evaluate its absorption efficiency for a generic incident plane wave. Using the circuit model one could calculate the FSS response to incoming plane waves in the spectral domain. The field at the focal plane of a parabolic reflector was already introduced in Section 2.2.1. The possibility of representing this field as a plane wave spectrum was discussed in this chapter. By linking the spectral domain representation of the field at the focal plane and the behavior of the FSS in the spectral domain, it was possible to characterize the behavior of the imager. The total field at the focal plane of the imager was computed. As a result, the absorbed power on the detector at the center of the FPA was computed when all the possible incoming plane waves were considered. Furthermore, by normalizing this absorbed power over the total power which illuminates the focusing system, the absorption efficiency of the imaging system was obtained. An approximated model was also introduced to represented this absorption efficiency.

In a step further, the above discussion is used to compute the angular response of the imager to a point source. This response indicates how much power a certain detector absorbs from each point in the FoV. The HPBW of the angular response is defined as the resolution of the imager. This response and the resolution are compared to the one of a uniformly illuminated reflector. It is observed that the former response is wider than the latter, and its resolution is larger. This effect is explained using an introduced convolution integral concept. This convolution integral is between a windowing factor introduced by the absorber size and the total field at the focal plane. Therefore, as the detector size increases, the result of the integral widens and the resolution enlarges.

In the last section of this chapter, the introduced methods were used to evaluate the system performance of the imager when a parabolic reflector is assumed as the focusing system and the detector is at the center of the FPA. Moreover, this evaluation is performed for the real optics used in CONSORTIS project. The latter was also performed for the detector at the edge of the FPA. The NETD of CONSORTIS optics was approximated by the one calculated for the parabolic reflector coupled to the detector. As it was discussed, the NETD is within the requirements of the project.

Chapter 5

Conclusion

The imaging systems at the sub-millimeter waves for security applications are subjects of interest in the research in the recent years. A sub-millimeter based system can operate at longer distances from the target in comparison to a mm wave based system, and still maintain sufficient spatial resolution. In the mm-wave systems, the image is acquired digitally by using phased arrays. However, having a large number of transceivers in the array with accurate phase control is not technologically available in the sub-mm regime. Therefore, the solution of acquiring the image using a quasi-optical system is widely used. Such imagers behave as cameras, which use focusing systems such as lenses or reflectors to generate the image. In this approach the quality of the image is determined by the optics.

The CONSORTIS project is an imager designed for security applications. The project is consist of both an active and a passive imager. In this thesis, its passive imager was investigated. The latter should absorb power from two different frequency bands simultaneously, i.e. a dual band imager is required. Since the thermal behavior of an object is a function of the frequency, absorbing different frequency bands provide more thermal information than a single-band system. Therefore, a dual band imager improves the probability of detection. The performance of an imager based on thermometers can be estimated using the noise equivalent temperature difference (NETD) concept. The NETD is the minimum temperature that the imager can detect. For the CONSORTIS project a certain NETD is required. To achieve such NETD value, one must have a high optical efficiency over a large bandwidth. In order to achieve this goal, two set of detectors were designed, each should absorb power in one band and reject it at the other. The frequency selectivity for the detectors is introduced by an absorber based FSS. This FSS is a periodic array of absorbing elements which is coupled to the bolometer based KIDs. Both the absorber based detector and the focusing system contribute to the total performance of the imager. Therefore, the possibility of evaluating the performance of the imager by combining both responses was of interest.

In chapter 2, the most well-known backgrounds needed to analyze both the detectors and the optical system in the spectral domain were discussed. The spectral analysis for the periodic structures were provide using the Floquet mode theorem. In this analysis, the response of a periodic structure to plane waves incoming from different angles of incidence is provided. Moreover, the Fourier optics was introduced to calculated the field at the focal plane of the focusing system. This field is presented as the spectral Fourier transform of the field at the aperture of an equivalent sphere. The sphere represents the surface of the focusing object. Both spectral analysis tools were introduced to provide the possibility of linking the response of the detectors on the FPA to the focusing system.

Chapter 3 focuses on designing the detectors used at the FPA. As it was mentioned, the detectors at the FPA are consist of FSS based absorbers coupled to the bolometer based KIDs. The FSS array is a periodic structure and its unit cell element was chosen as the Jerusalem cross. The Jerusalem cross has a sharp roll off behavior after its resonance. This behavior is useful in designing a dual band system. An absorber based FSS uses absorbing materials with a finite conductivity. As a result, the current which is flowing on the FSS decays and absorbed on the lossy metal. Therefore, the amplitude of the incident signal is received in terms of heat. A backing reflector is placed at a certain distance from the FSS to insure the possibility of absorbing all of the incident power. The FSS is designed as a free standing structure without considering the effects of having the bolometer based KIDs underneath the array. For the dual band imager, two absorber based FSS are designed, each operating at one frequency band and reject the power on the other band. By obtaining the equivalent impedance of the FSS, using CST simulation software, the geometrical parameters of the unit cell element were designed to insure high absorption rate in the operation band, and high rejection of power at the rejection band. These absorbers are referred to as the f_1 and f_2 absorbers, which operate at a frequency band centered around f_1 and f_2, respectively ($f_2 = 2f_1$).

Moreover, in the third chapter, two more realistic versions of the structure were discussed. Firstly, the effects of having a finite FSS array was investigated. The finiteness effect was modeled as an effective area. The latter is an area on the designed infinite FSS array which absorbs the same amount of power as a finite array with a certain physical area. In a study, the effective area was computed for different finite array sizes and was compared to the physical area. As the result of this study, it was visible that the finiteness effect is negligible for a squared shaped detector with a side length larger than the wavelength. Since the designed f_1 and f_2 detectors have larger lengths than λ_1 and λ_2, respectively, the finiteness effect is neglected in this work. Secondly, the resonator lines of the bolometer based KIDs, and the dielectric layer between the FSS and the lines were added to the structure. As the result, the behavior of the free standing design was significantly distorted. Therefore, the design was readjusted to compensate for the added effects. Since the added resonator lines are not symmetric, the symmetry of the design was lost and the response of the structure for the horizontal and vertical polarizations differs.

In chapter 4, the performance of the imager including both the detectors at the FPA, and the focusing system is evaluated. To achieve this goal, a circuit model for the absorber based FSS is introduced, which evaluates the amount of power absorbed when a generic plane wave impinges on the structure. The results from the circuit model discussion indicate that for this specific absorbing geometry, it is possible to separate the TE and TM components of a plane wave and investigate each component independently. Therefore, the power absorbed from an incoming plane wave is approximated as the summation of the absorbed power from the TE and TM components. Moreover, the calculated field at the focal plane of the parabolic reflector (direct field) is represented as a summation of incoming plane waves by using the discussed Fourier optics method. The direct field does not take into account the effects of the stratification or the absorber based FSS at the focal plane. The total field includes those effects. By using the circuit model for each possible incoming plane wave, one can calculate a spectral component of the total field. The spatial distribution of the total field can be calculated using the spectral Fourier transform. The amount of power absorbed by the imager is then computed using the Poynting theorem. This calculations is referred to as the full method in the chapter. An approximated method was also introduced to obtain the absorption efficiency of the imager. In this approximation, the efficiency is approximated as the spillover efficiency multiplied by the efficiency of the absorber at broadside.

The angular response of the imager to a point source is defined as the amount of power a detector on the FPA receives from different angular positions in the FoV. The half power beam width (HPBW) of the normalized angular response is defined as the resolution of the imager. The angular response can be obtained by calculating the absorption efficiency of the imager. This response for an imager coupled to absorbers has a wider main lobe than the angular response of a uniformly illuminated reflector with the same geometrical parameters. Moreover, the main lobe of the response of the imager widens as the detector size increases. Therefore, the resolution of the imager also enlarges when a larger detector is present. The side lobes of both responses are comparable.

In the last section of chapter 4, the discussed analysis methods were used to evaluate the performance of an imager coupled to absorbers. Firstly, the performance of reflector based imager was evaluated for two cases: when it was coupled to the free standing absorber based FSS, and also when it was coupled to the design which included the resonator lines. Secondly, the performance of the CONSORTIS optics were evaluated for both a detector at the center of the FPA and the one at the edge. The performance of these imagers were reported in terms of the optical efficiency, normalized angular response, resolution and the NETD of the imager while scanning a large FoV. The CONSORTIS optics is a lens based optics. Therefore, the dielectric losses of the lens is also included in the calculation of the optical efficiency and the NETD. The required NETD for the CONSORTIS optics was largely met for both the detectors at the center and at the edge of the FPA.

The FSS based absorbers achieved the absorption efficiency of approximately 100% at the center of their operation band. Moreover, the absorption rate at the center of the rejection band of the f_1 and f_2 absorbers are 0% and 1% at broadside, respectively. The sensitivity of the CONSORTIS optics coupled to a detector at the edge of the FPA is provided in terms of the NETD. The latter is calculated including the absorption loss inside the lens system, and is lower than 0.2 K and 0.3 K for the f_1 and f_2 absorbers, respectively.

5.1 Future Research

In this thesis, using the Fourier optics, the field at the focal plane of a parabolic reflector was reported, for the case that the reflector is illuminated from broadside. Therefore, the analysis for the parabolic reflector based imager was provided only for the detector located at the center of the FPA. In order to extend the analysis method to detectors at the edge of the FPA, one must calculated the spectral representation of the direct field generated by an oblique illuminations of the parabolic reflector, analytically. The introduced Fourier optics should be used to achieve this goal. Moreover, in this thesis, the performance of the CONSORTIS optics was evaluated by only using the approximated method. This goal was achieved by using the GRASP computational software to simulate the spatial distribution of the field at the focal plane of the CONSORTIS optics for both the broadside and oblique illuminations. The spectral analysis (full method) should be performed for both the detector at the edge and the center of the FPA to check whether the accuracy of the approximated method is tolerable.

Bibliography

[1] B. Blazquez, *Quasioptical Imaging Systems at THz Frequencies*, PhD. dissertation, Technical University of Delft, 2015.

[2] A. V. Timofeev, V. Vesterinen, P. HelistÃű, L. GrÃűnberg, J. Hassel, and A. Luukanen, "Submillimeter-wave kinetic inductance bolometers on free-standing nanomembranes," *Superconductor Science and Technology*, vol. 27, no. 2, p. 025002, 2014. [Online]. Available: http://stacks.iop.org/0953-2048/27/i=2/a=025002

[3] R. Appleby and H. Wallace, "Standoff detection of weapons and contraband in the 100 ghz to 1 thz region," *IEEE Trans. Antennas and Propag.*, vol. 55, no. 11, pp. 2944–2956, Nov 2007.

[4] K. Cooper, R. Dengler, N. Llombart, B. Thomas, G. Chattopadhyay, and P. Siegel, "Thz imaging radar for standoff personnel screening," *Terahertz Science and Technology, IEEE Transactions on*, vol. 1, no. 1, pp. 169–182, Sept 2011.

[5] G. Zentai and L. Partain, "Development of a high resolution, portable x-ray imager for security applications," in *Imaging Systems and Techniques, 2007. IST '07. IEEE International Workshop on*, May 2007, pp. 1–5.

[6] S. S. Ahmed, A. Schiessl, and L.-P. Schmidt, "A novel active real-time digital-beamforming imager for personnel screening," in *Synthetic Aperture Radar, 2012. EUSAR. 9th European Conference on*, April 2012, pp. 178–181.

[7] S. Ahmed, A. Schiessl, and L. Schmidt, "A novel fully electronic active real-time imager based on a planar multistatic sparse array," *Microwave Theory and Techniques, IEEE Transactions on*, vol. 59, no. 12, pp. 3567–3576, Dec 2011.

[8] J. F. Federici, B. Schulkin, F. Huang, D. Gary, R. Barat, F. Oliveira, and D. Zimdars, "Thz imaging and sensing for security applicationsâĂŤexplosives, weapons and drugs," *Semiconductor Science and Technology*, vol. 20, no. 7, p. S266, 2005. [Online]. Available: http://stacks.iop.org/0268-1242/20/i=7/a=018

[9] J. Lovberg, C. Martin, and V. Kolinko, "Video-rate passive millimeter-wave imaging using phased arrays," in *Microwave Symposium, 2007. IEEE/MTT-S International*, June 2007, pp. 1689–1692.

[10] N. Llombart, K. Cooper, R. Dengler, T. Bryllert, and P. Siegel, "Confocal ellipsoidal reflector system for a mechanically scanned active terahertz imager," *Antennas and Propagation, IEEE Transactions on*, vol. 58, no. 6, pp. 1834–1841, June 2010.

[11] E. Gandini and N. Llombart, "Toward a real time stand-off submillimeter-wave imaging system with large field of view: quasi-optical system design considerations," *Proc. SPIE*, 2015.

[12] E. Grossman, C. Dietlein, J. Ala-Laurinaho, M. Leivo, L. Gronberg, M. Gronholm, P. Lappalainen, A. Rautiainen, A. Tamminen, and A. Luukanen, "Passive terahertz camera for standoff security screening," *Appl. Opt.*, vol. 49, pp. E106–E120, Jul 2010.

[13] G. Chattopadhyay, "Submillimeter-wave coherent and incoherent sensors for space applications," in *Sensors*, ser. Lecture Notes Electrical Engineering, S. Mukhopadhyay and R. Huang, Eds. Springer Berlin Heidelberg, 2008, vol. 21, pp. 387–414. [Online].

Available: http://dx.doi.org/10.1007/978-3-540-69033-7_19

[14] J. Zmuidzinas, J. W. Kooi, J. Kawamura, G. Chattopadhyay, B. Bumble, H. G. LeDuc, and J. A. Stern, *Development of SIS mixers for 1 THz*, 1998, vol. 3357. [Online]. Available: http://dx.doi.org/10.1117/12.317386

[15] A. Karpov, D. Miller, J. Stern, B. Bumble, H. LeDuc, I. Mehdi, R. Lin, and J. Zmuidzinas, "Low noise 1 thz sis mixer for stratospheric observatory: Design and characterization," *Applied Superconductivity, IEEE Transactions on*, vol. 21, no. 3, pp. 616–619, June 2011.

[16] J. Gao, M. Hajenius, Z. Yang, J. Hovenier, J. Baselmans, A. Baryshev, P. Khosropanah, and T. Klapwijk, "Thz superconducting hot electron bolometer heterodyne receivers," in *Infrared Millimeter Waves and 14th International Conference on Teraherz Electronics, 2006. IRMMW-THz 2006. Joint 31st International Conference on*, Sept 2006, pp. 545–545.

[17] T. Crowe, R. Mattauch, H. Roser, W. Bishop, W. Peatman, and X. Liu, "Gaas schottky diodes for thz mixing applications," *Proceedings of the IEEE*, vol. 80, no. 11, pp. 1827–1841, Nov 1992.

[18] M. Gaidis, H. Pickett, C. Smith, S. Martin, R. Smith, and P. Siegel, "A 2.5-thz receiver front end for spaceborne applications," *Microwave Theory and Techniques, IEEE Transactions on*, vol. 48, no. 4, pp. 733–739, Apr 2000.

[19] E. Ojefors, U. Pfeiffer, A. Lisauskas, and H. Roskos, "A 0.65 thz focal-plane array in a quarter-micron cmos process technology," *Solid-State Circuits, IEEE Journal of*, vol. 44, no. 7, pp. 1968–1976, July 2009.

[20] B. Cabrera, R. Clarke, P. Colling, A. Miller, S. Nam, and R. Romani, "Detection of single infrared, optical, and ultraviolet photons using superconducting transition edge sensors," *Applied Physics Letters*, vol. 73, no. 6, pp. 735–737, 1998.

[21] B. Karasik, A. Sergeev, and D. Prober, "Nanobolometers for thz photon detection," *Terahertz Science and Technology, IEEE Transactions on*, vol. 1, no. 1, pp. 97–111, Sept 2011.

[22] P. K. Day, H. G. LeDuc, B. A. Mazin, A. Vayonakis, and J. Zmuidzinas, "A broadband superconducting detector suitable for use in large arrays," *Nature*, vol. 425, no. 6960, pp. 817–821, 2003.

[23] E. Burstein, D. N. Langenberg, and B. N. Taylor, "Superconductors as quantum detectors for microwave and sub-millimeter-wave radiation," *Phys. Rev. Lett.*, vol. 6, pp. 92–94, Feb 1961. [Online]. Available: http://link.aps.org/doi/10.1103/PhysRevLett.6.92

[24] J. Glenn, P. A. Ade, M. Amarie, J. J. Bock, S. F. Edgington, A. Goldin, S. Golwala, D. Haig, A. E. Lange, G. Laurent *et al.*, "Current status of bolocam: a large-format millimeter-wave bolometer camera," in *Astronomical Telescopes and Instrumentation*. International Society for Optics and Photonics, 2003, pp. 30–40.

[25] E. Kreysa, H. Gemund, A. Raccanelli, L. Reichertz, and G. Siringo, "Bolometer arrays for mm/submm astronomy," *AIP Conference Proceedings*, pp. 262–269, 2002.

[26] A. Baryshev, J. Baselmans, S. Yates, L. Ferrari, R. Bisigello, R. Janssen, A. Endo, K. T.M, B. Klein, S. Heyminck, and R. Gusten, "Large format antenna coupled microwave kinetic inductance detector arrays for radio astronomy," *39th Conference on Infrared, Millimeter and THz Waves*, 2014.

[27] B. Mazin, *Microwave kinetic inductance detectors*, PhD. dissertation, California Institue of Technology, United States, California, 2004.

[28] C. A. Balanis, *Antenna Theory: Analysis and Design*. Wiley-Interscience, 2005.

[29] S. Rao, L. Shafai, and S. Sharma, Eds., *Handbook of Reflector Antennas and Feed Systems Volume III, Applications of Reflectors*. Artech House, 2013.

[30] J. C. Mather, "Bolometer noise: nonequilibrium theory," *Appl. Opt.*, vol. 21, no. 6, pp. 1125–1129, Mar 1982. [Online]. Available: http://ao.osa.org/abstract.cfm?URI=

ao-21-6-1125
[31] J. Hassel, *Internal report in CONSORTIS project*, Oct 2014.
[32] *www.consortis.eu*.
[33] N. Llombart, *Internal report in CONSORTIS project*, Feb 2015.
[34] C. A. Balanis, *Advanced engineering electromagnetics*. John Wiley & Sons, 2012.
[35] L. B. Felsen and N. Marcuvitz, *Radiation and scattering of waves*. John Wiley & Sons, 1994, vol. 31.
[36] D. Cavallo, *Connected Array Antennas: Analysis and Design*, PhD. dissertation, University of Eindhoven, 2011.
[37] A. Neto and S. Maci, "Green's function for an infinite slot printed between two homogeneous dielectrics. i. magnetic currents," *Antennas and Propagation, IEEE Transactions on*, vol. 51, no. 7, pp. 1572–1581, July 2003.
[38] S. Maci and A. Neto, "Green's function of an infinite slot printed between two homogeneous dielectrics-part ii: uniform asymptotic solution," *Antennas and Propagation, IEEE Transactions on*, vol. 52, no. 3, pp. 666–676, March 2004.
[39] R. Collin, *Field Theory of Guided Waves*. New York: McGraw-Hill, 1960.
[40] G. Mur, "A finite dilyerence method for the solution of electromagnetic waveguide discontinuity problems," *Microwave Theory and Techniques, IEEE Transactions on*, vol. 22, no. 1, pp. 54–57, Jan 1974.
[41] A. Taflove and S. Hagness, *Computational Electrodynamics: The Finite-difference Time-domain Method*. Artech House, 2005.
[42] D. Lynch and K. Paulsen, "Time-domain integration of the maxwell equations on finite elements," *Antennas and Propagation, IEEE Transactions on*, vol. 38, no. 12, pp. 1933–1942, Dec 1990.
[43] P. Silvester and R. Ferrari, *Finite Elements for Electrical Engineers*. Cambridge University Press, 1996. [Online]. Available: https://books.google.nl/books?id=QXWFEIesd14C
[44] F. Teixeira, "Time-domain finite-difference and finite-element methods for maxwell equations in complex media," *Antennas and Propagation, IEEE Transactions on*, vol. 56, no. 8, pp. 2150–2166, Aug 2008.
[45] R. Harrington, *Field Computation by Moment Methods*. Wiley-IEEE Press, 1993.
[46] M. Bass, C. DeCusatis, J. Enoch, V. Lakshminarayanan, G. Li, C. Macdonald, V. Mahajan, and E. Van Stryland, "Handbook of optics, volume i: Geometrical and physical optics," *Polarized Light, Components and Instruments (set)*, 2010.
[47] P. Goldsmith, *Quasioptical Systems: Gaussian Beam Quasioptical Propogation and Applications*. Wiley-IEEE Press, 1998.
[48] E. Wolf, "Electromagnetic diffraction in optical systems. i. an integral representation of the image field," in *Proceedings of the Royal Society of London A: Mathematical, Physical and Engineering Sciences*, vol. 253, no. 1274. The Royal Society, 1959, pp. 349–357.
[49] N. Llombart, B. Blazquez, A. Freni, and A. Neto, "Fourier optics for the analysis of distributed absorbers under thz focusing systems," *Terahertz Science and Technology, IEEE Transactions on*, vol. 5, no. 4, pp. 573–583, July 2015.
[50] B. Munk, *Frequency Selective Surfaces Theory and Design*. Wiley-Interscience, 2000.
[51] S. Monni, *Frequency Selective Surfaces Integrated with Phased Array Antennas, Analysis and Design using Multimode Equivalant Networks*, PhD. dissertation, University of Eindhoven, 2005.
[52] B. Blazquez, N. Llombart, D. Cavallo, A. Freni, and A. Neto, "A rigorous equivalent network for linearly polarized thz absorbers," *Antennas and Propagation, IEEE Transactions on*, vol. 62, no. 10, pp. 5077–5088, Oct 2014.
[53] D. M. Pozar, *Microwave Engineering*. John Wiley & Sons, 2012.
[54] S. Maci, Z. Sipus, A. Freni, A. Mazzinghi, and S. Skokic, *Advanced Mathematics for An-*

tenna Analysis, Class notes for European School of Antennas Course, Dubrovnik, Croatiam May 14-19, 2012.

[55] D. Cavallo, A. Neto, and G. Gerini, "Green's function based equivalent circuits for connected arrays in transmission and in reception," *Antennas and Propagation, IEEE Transactions on*, vol. 59, no. 5, pp. 1535–1545, May 2011.

[56] A. Neto, D. Cavallo, G. Gerini, and G. Toso, "Scanning performances of wideband connected arrays in the presence of a backing reflector," *Antennas and Propagation, IEEE Transactions on*, vol. 57, no. 10, pp. 3092–3102, Oct 2009.

[57] A. Neto and J. Lee, "Ultrawide-band properties of long slot arrays," *Antennas and Propagation, IEEE Transactions on*, vol. 54, no. 2, pp. 534–543, Feb 2006.

[58] N. Llombart, E. Gandini, B. Blazquez, A. Freni, and A. Neto, "Coherent fourier optics representation of focal plane fields," *European Conference on Antennas and Propagation*, 2015.

[59] M. J. Griffin, J. J. Bock, and W. K. Gear, "Relative performance of filled and feedhorn-coupled focal-plane architectures," *Appl. Opt.*, vol. 41, no. 31, pp. 6543–6554, Nov 2002.

[60] P. F. Goldsmith, *Quasioptical Systems: Gaussian Beam Quasioptical Propogation and Applications*. Wiley-IEEE Press, 1997.

Appendix A

List of abbreviations

List of abbreviations	
1D	One dimensional
2D	Two dimensional
3D	Three dimensional
BW	Band width
CST	Computer Simulation Technology
et al.	et alii (*lat.* and others)
etc.	et cetera (*lat.* and so forth)
EFIE	Electric Field Integral Equation
e.g.	exempli gratia (*lat.* for example; example given)
EM	Electromagnetic
FO	Fourier Optics
FoV	Field of View
FPA	Focal Plane Array
FSS	Frequency Selective Surface
FT	Fourier Transform
GF	Green's Function
GO	Geometric Optics
HPBW	Half Power Beam Width
JC	Jerusalem Cross
IE	Integral Equation(s)
i.e.	id est (*lat.* that is; in other words; that is to say)
KID	Kinetic Inductance Detector
NEP	Noise Equivalent Power
NETD	Noise Equivalent Temperature Difference
PEC	Perfect Electric Conductor(s)
PO	Physical Optics
SNR	Signal to Noise Ratio
TE	Transverse Electric
TM	Transverse Magnetic